

Usman Tahir Virk

Characterization of Vehicle Penetration Loss at Wireless Communication Frequencies

School of Electrical Engineering

Thesis submitted in partial fulfillment of the requirements
for the degree of Master of Science in Technology at Aalto
University, Espoo, Finland.

9.11.2012

Thesis supervisor:



Prof. Dr. Antti Räisänen

Thesis instructor:



Dr. Katsuyuki Haneda

Dedicated to my parents, my grand parents and Prof. Pertti Vainikainen

Author: Usman Tahir Virk

Title: Characterization of Vehicle Penetration Loss at Wireless
Communication Frequencies

Date: 9.11.2012

Language: English

Number of pages:0+164

Department of Radio Science and Engineering

Professorship: Radio Engineering

Code: S-26

Supervisor: Prof. Dr. Antti Räsänen

Instructor: Dr. Katsuyuki Haneda

Automotive window films are widely used for heat rejection, protection from ultra-violet radiations and glare control purposes. For an increased performance, these films are usually metallized since metals effectively reflect the impinging electromagnetic radiations. The expend of metallization in these films may affect the communication of radio signals into vehicles. In this perspective, the provision of reliable in-vehicle coverage is a major goal of both wireless network providers and automotive industry. In order to quantify the effects of automotive window films on communication signals inside a vehicle, this research study was undertaken with industrial cooperation.

The thesis presents the characterization of Vehicle Penetration Loss (VPL) at major wireless communication frequencies based on empirical and numerical evaluation and by exploiting different window coatings including a commercially available automotive window film and Aluminium metal foil. The research involves ultra-wideband (UWB) car measurement campaign for the frequency range of 0.6-6.0 GHz in an indoor industrial environment at an isolated storage facility in Helsinki utilizing a regular sized hatchback car. Several realistic measurement scenarios were considered to obtain large measurement sets. The measurement data was post-processed using fine algorithms to exploit various channel characteristics to gain sufficient understanding of associated propagation phenomenon. Window films were also exclusively measured in a specialized environment to accurately asses the associated penetration loss. Apart from measurements, numerical analysis based on Finite-difference time-domain (FDTD) method for the assessment of VPL was carried out at discrete frequencies, 900 MHz and 1.2 GHz. The numerical approach can serve as a future alternate to measurements provided that adequate computational resources are available. The results infer that the use of metallized automotive films can severely affect the communication of radio signals into vehicles.

Keywords: Automotive window films, Vehicle Penetration Loss (VPL), ultra-wideband (UWB), Finite-difference time-domain (FDTD)

Preface

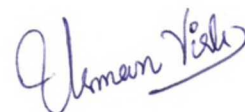
A research cooperation with industry extends the perspectives of researchers, provide valuable resource support and lead to discoveries that are significant in terms of broad public interest. This masters thesis is the outcome of the research project VEPRO undertaken by Radio Science and Engineering Department, Aalto University and sponsored by Renesas Mobile. The research work under the scope of this thesis is fully consonant with the obligations of both Aalto University and Renesas Mobile.

Writing a research thesis is a challenging task. However, this opportunity enabled me to explore many avenues in research, equipped me with dynamic skills and motivated me for pursuing a research career. Above all, my first and utmost praises go to Allah Almighty the Creator and Lord of mankind and everything that exists. I thank Allah Almighty for granting me this opportunity and providing me the capacity to accomplish it successfully.

It would not have been possible to complete this thesis without the help and support of kind and professional people around me. I thank all of them and to some of whom a particular mention is given here. I am greatly indebted to my initial supervisor Prof. Pertti Vainikainen and would like to pay my respect and gratitude for all his support and trust during my study period at Aalto University. I wish he cherishes a healthy and happy life. I would like to express my earnest thanks to my supervisor, Prof. Antti Räisänen for trusting my capabilities and accepting me in the middle of this research study despite his extremely busy schedule. I thank him for giving me time and worthy suggestions to correct the thesis. I owe a sincere and deepest gratitude to my instructor Dr. Katsuyuki Haneda whose unsurpassed knowledge, professional experience and commitment have always inspired me. I thank him for the insightful discussions, critical suggestions and encouragement in all times of research, especially for his patience and invaluable guidance during the writing process and proofreading of this thesis. I am also highly grateful to Dr. Veli-Matti Kolmonen who has a nonpareil input to my research career and always had time for my queries. I thank him for always encouraging and guiding me in research, no matter how hard is the problem. I wish him a happy life and a prosperous future. I would like to thank Dr. Yrjo Kaipainen from Renesas Mobile for his cooperation and keen interest in the research. I am thankful to all laboratory and departmental staff who helped and contributed in this research. I thank all my colleagues in the propagation group for their support and friendly environment.

Finally, I would like to warmly thank my parents, brother and sisters who have given me their unequivocal support and encouragement throughout my life and a simple expression of thanks does not suffice their role in my life.

Otaniemi, Espoo: 9.11.2012



Usman Tahir Virk

Contents

Abstract	2
Preface	3
Contents	4
List of tables	8
List of figures	11
Symbols and abbreviations	12
1 Introduction	15
1.1 Background and motivation	16
1.2 Objectives	18
1.3 Scope of work	18
1.4 Organization of thesis	19
2 Ultra-wideband antennas and propagation	20
2.1 Introduction	20
2.2 Ultra-Wideband propagation channels	21
2.2.1 Wireless channel representation	22
2.2.2 Frequency selectivity of propagation channels	24
2.2.3 UWB channel characteristics	26
2.2.3.1 Path loss	26
2.2.3.2 Large-scale fading	28
2.2.3.3 Small-scale fading	30
2.2.3.4 Path loss, shadowing and small-scale fading: one picture	32
2.2.4 Reflection, transmission and scattering from materials	33
2.2.4.1 Reflection and transmission	33
2.2.4.2 Surface scattering	36
2.2.5 Delay domain channel expressions	37
2.2.5.1 Power delay profile (PDP)	37
2.2.5.2 RMS delay spread	38
2.2.6 Delay domain channel models	39
2.2.6.1 Saleh-Valenzuela model	39
2.2.6.2 The Δ -K model	40
2.2.6.3 The two-cluster model	41
2.2.6.4 The single Poisson model	42
2.2.7 UWB channel measurement techniques	43

2.2.7.1	Time domain (TD)	43
2.2.7.2	Frequency domain (FD)	44
2.3	UWB antennas	47
2.3.1	Antenna design considerations	47
2.4	Summary	49
3	Shielding theory and literature review for Vehicle Penetration Loss	50
3.1	Introduction	50
3.2	Electromagnetic shielding	50
3.2.1	Shielding effectiveness	52
3.2.2	Shielding apertures	54
3.3	Previous investigations for VPL	56
3.3.1	Hill and Kneisel (1991)	56
3.3.2	Vogel, Torrence and Kleiner (1996)	57
3.3.3	Kostanic, Hall and McCarthy (1998)	59
3.3.4	Harrysson (2003)	60
3.3.5	Berens, et al. (2007)	61
3.3.6	Tanghe, Joseph, Verloock, Martens(2008)	63
3.3.7	Harrysson, et al. (2011)	65
3.4	Contribution of this thesis	66
3.5	Summary	66
4	Ultra-wideband measurements	67
4.1	Introduction	67
4.2	UWB car measurements	68
4.2.1	Measurement location and environment	68
4.2.2	Measurement environment layout	69
4.2.3	Car interior layout	70
4.2.4	Measurement equipment	71
4.2.5	Measurement system and setup	74
4.2.6	Measurement scenarios	76
4.2.6.1	Inside-outside measurements	76
4.2.6.2	Intra-car measurements	79
4.2.6.3	Outside measurement	80
4.2.6.4	Reference measurement	82
4.2.7	Measurements summary	84
4.3	UWB window film measurements	85
4.3.1	Measurement location and environment	85
4.3.2	Measurement layout description	86
4.3.3	Measurement equipment	87
4.3.4	Measurement system and setup	88
4.3.5	Measurement scenarios	89
4.3.6	Measurements summary	91
4.4	Summary	91

5	Data post-processing and analysis	93
5.1	Introduction	93
5.2	UWB car measurements	94
5.2.1	Post-processing flow diagram	94
5.2.2	Post-processing steps	95
5.2.2.1	Data calibration	95
5.2.2.2	Windowing	97
5.2.2.3	Fourier transformation (FT)	98
5.2.3	Channel characteristics	99
5.2.3.1	Channel transfer function (CTF)	100
5.2.3.2	Vehicle penetration loss (VPL)	101
5.2.3.3	Power delay profiles (PDPs)	105
5.2.3.4	RMS delay spread (DS)	120
5.2.3.5	Directional estimation: Beamforming	122
5.2.3.6	Discrete power angle delay profile (DPADP)	124
5.2.3.7	Geometry based path identification	129
5.3	UWB window film measurements	132
5.3.1	Post-processing flow diagram	132
5.3.2	Channel characteristics	133
5.3.2.1	Window film penetration loss (WFPL)	133
5.3.2.2	Channel impulse response (CIR)	134
5.4	Summary	136
6	Numerical analysis	137
6.1	Introduction	137
6.2	Finite-difference time-domain (FDTD) method	138
6.2.1	Formulation of FDTD algorithm	138
6.2.2	Computational load	140
6.2.3	Numerical dispersion	141
6.2.4	Numerical stability criteria	142
6.2.5	Strengths and weaknesses	142
6.2.6	Challenges for radio channel modelling	143
6.3	Boundary conditions	144
6.3.1	Absorbing boundary conditions (ABC)	144
6.3.1.1	Perfectly matched layers (PML):	144
6.3.1.2	Analytical absorbing boundary conditions (A-ABC)	144
6.3.2	Perfectly conductive boundary conditions	145
6.3.3	Perfectly magnetic boundary conditions	145
6.3.4	Periodic boundary conditions	145
6.4	Simulations	145
6.4.1	Simulation tools	146
6.4.1.1	FDTD electromagnetic solver	146
6.4.1.2	Computing hardware	146
6.4.2	Simulation model	146
6.4.3	Simulation setup	150

6.4.3.1	Material properties	150
6.4.3.2	Primary simulation settings	151
6.4.3.3	Multi-simulation setup	152
6.4.3.4	Convergence criteria	152
6.4.4	Simulation results	152
6.4.4.1	Plane wave illumination	152
6.4.4.2	VPL	154
6.4.4.3	Simulations versus measurements	156
6.5	Summary	156
7	Conclusions and future thoughts	157
	References	159

List of Tables

3.1	Mean VPL results from [1]	57
3.2	Mean VPL results from [2]	59
3.3	Mean VPL results from [3]	60
3.4	Mean VPL results from [4]	61
3.5	Mean VPL results from [5]	62
3.6	Mean VPL results from [6]	65
3.7	Mean VPL results from [7]	66
4.1	UWB car measurement setup	76
4.2	Measurements summary	84
4.3	Window film measurement setup	89
4.4	Measurements summary	91
5.1	Mean VPL in dBs	104
5.2	Total leakage level for rooftop-to-car channels.	115
5.3	DPADPs parameters for the reference case	125
5.4	DPADPs parameters for the reference case	126
5.5	DPADPs parameters for the no coating case	127
5.6	DPADPs parameters for the no coating case	128
5.7	DPADPs parameters for Aluminium foil case	128
5.8	Path identification for the reference case	130
5.9	Path identification for the no coating case	131
6.1	Material properties	151
6.2	Grid size for simulations	152
6.3	Mean simulated VPL	156
6.4	VPL comparison between simulations and measurements	156

List of Figures

1.1	Solar energy interaction with a normal glass pane	16
2.1	FCC spectral masks for indoor and outdoor UWB transmissions . . .	21
2.2	Typical multipath propagation environment	22
2.3	Bandwidth effect of propagation channels	24
2.4	Shadowing effect due to building obstacle	29
2.5	Underlying dynamics of received signal [8]	32
2.6	Radio wave incident on a surface	33
2.7	Scattering from rough surfaces	36
2.8	Saleh-Velenzuela model	40
2.9	The Δ -K model	41
2.10	The two-cluster model	41
2.11	The single Poisson model	42
2.12	Time domain channel measurement set-up	44
2.13	Frequency domain channel measurement set-up	46
2.14	Typical examples of UWB antennas	47
2.15	TX-RX antenna system	48
3.1	Shielding enclosure	51
3.2	Plane wave incident on a shield	52
3.3	Effect of shielding aperture slots on induced currents	55
3.4	Slot antennas	55
3.5	Plane wave incident on a shield with a slot aperture	56
4.1	Measurement location maps (a) topographic (b) satellite	68
4.2	Measurement environment: (a) measurement area, (b) rear portion. .	69
4.3	Measurement environment layout	70
4.4	Car interior layout for measurements	71
4.5	UWB car measurement equipment; (a) Toyota Prius car, (b) Bi-conical TX-RX antennas, (c) VNA, (d) Tripod stand with L-shape antenna fixture.	72
4.6	Measured and simulated return loss of TX-RX bi-conical antennas .	73
4.7	Measurement setup for UWB car measurements	75
4.8	Inside-outside measurement scenario	77
4.9	Inside-outside measurements depicting (a) RX around car (b) TX on 2D scanner inside car	78

4.10	Inside-outside (a) window coating measurements (b) car rooftop to inside measurements	78
4.11	Intra-car measurement scenario	79
4.12	Intra-car measurements	80
4.13	Outside measurement scenario	81
4.14	Outside measurements (a) TX antenna on car rooftop close-up (b) RX antenna around car	81
4.15	Reference measurement scenario	82
4.16	Reference measurements	83
4.17	Measurement environment	85
4.18	Measurement layout	86
4.19	Measurement equipment; (a) VNA, (b) antennas, (c) tripod stand.	87
4.20	Measurement setup for window film measurements	88
4.21	PX-Slate measurement	90
4.22	Century-Nova measurement	90
4.23	Reference measurement	91
5.1	Post-processing flow diagram for UWB car measurements	94
5.2	General measurement setup	95
5.3	Back-to-back calibration setup	96
5.4	Gaussian window	98
5.5	Passband Hermitian reconstruction (PHR)	99
5.6	Channel transfer function for complete frequency band	100
5.7	VPL for sub-bands I & II	102
5.8	VPL for sub-bands III & IV	103
5.9	VPL for sub-bands V & VI	104
5.10	Power delay profile for complete frequency band at RX 90°	106
5.11	PDPs in I & II frequency sub-bands	107
5.12	PDPs in III & IV frequency sub-bands	108
5.13	PDPs in V & VI frequency sub-bands	108
5.14	PDPs for 0.6-6.0 GHz frequency band with RX around the car	109
5.15	Variation of LOS delay w.r.t RX angle around the car	110
5.16	PDPs for 0.6-6.0 GHz frequency band with RX at front, rear and lateral sides of the car	111
5.17	PDPs for open and close car windows at RX angle 90°	111
5.18	PDPs for RX angle 90° with human presence inside car	112
5.19	PDPs for RX angle 0° with different RX heights	113
5.20	PDPs for 0.6-6.0 GHz frequency band with different Aluminium foil coating configurations at front and rear of the car	114
5.21	PDPs for 0.6-6.0 GHz frequency band with different Aluminium foil coating configurations at lateral sides of the car	114
5.22	PDPs of radio channels from car roof-top to car interior with Aluminium foil covering on windows	115
5.23	PDPs for 0.6-6.0 GHz frequency band at RX angle 0° with co-polar and cross-polar channel	116

5.24	PDPs for 0.6-6.0 GHz frequency band for cross-polar channel	117
5.25	PDPs for 0.6-6.0 GHz frequency band for cross-polar channel	117
5.26	PDPs for 0.6-6.0 GHz frequency band Intra-car measurements for five RX positions	118
5.27	PDPs for 0.6-6.0 GHz frequency band Intra-car measurements with and without Aluminium foil	119
5.28	CIRs for Outside measurements	119
5.29	RMS delay spread in frequency sub-bands I & II	120
5.30	RMS delay spread in frequency sub-bands III & IV	121
5.31	RMS delay spread in frequency sub-bands V & VI	122
5.32	Two-dimensional planar array signal model	123
5.33	DPADPs at the lowest frequency sub-band for the reference case . . .	125
5.34	DPADPs at the highest frequency sub-band for the reference case . .	126
5.35	DPADPs at the lowest frequency sub-band for the no coating case . .	127
5.36	DPADPs at the highest frequency sub-band for the no coating case .	128
5.37	DPADPs at lowest frequency sub-band for Aluminium foil case . . .	129
5.38	Path identification for the reference case at RX angle 90°	130
5.39	Path identification for the no coating case at RX angle 90°	131
5.40	Post-processing flow diagram for UWB window film measurements .	132
5.41	WFPL for PerformX-Slate-50	133
5.42	WFPL for Century-Nova-50	134
5.43	CIR for Perform-XSlate-50	135
5.44	CIR for Century-Nova-50	135
6.1	3D Yee grid with E and H-field components	138
6.2	Auto-cad Toyota Prius car model (a) polygon representation (b) full model	147
6.3	SEMCAD-X Toyota Prius car model (a) side view (b) side view with interior illustrated (c) front view (d) rear view	147
6.4	Antenna simulation model (a) TX antenna (b) RX antenna	148
6.5	Simulation scenario with Rx outside and TX inside the car	149
6.6	Reference simulation scenario	149
6.7	TX antenna modelling inside car	150
6.8	Plane wave excitation of car (a) E-field slice in x-y plane (b) total field region encapsulating car	153
6.9	E-Field cartography for Total-Field Scattered Field simulation	154
6.10	Return loss for TX-RX antennas at 900 MHz	155
6.11	Return loss for TX-RX antennas at 1.2 GHz	155

Symbols and abbreviations

Symbols

A	Amplitude
B_c	Coherence bandwidth
B_f	Fractional bandwidth
$B_w/B/BW$	Bandwidth
c	Speed of light $\approx 3 \times 10^8$ [m/s]
d	Distance
dB	Decibels
E	Electric field
f	Frequency
f_c	Center frequency
f_H	Maximum frequency
f_L	Minimum frequency
G_t	Transmit antenna gain
G_r	Receive antenna gain
H	Magnetic field
$H(f)$	Transfer function
k	Wave number
L_{dB}	Loss in dB
P_t	Transmitted power
P_r	Received power
$p(x)$	Probability density function
T	Transmission coefficient
T_b	Bit duration
T_s	Symbol time
T_m	Measurement time
X	Random variable
α	Electrical length
β	Multipath amplitude
Γ	Fresnel reflection coefficient
γ	Decay exponent
δ	Skin depth
ϵ	Permittivity
ϵ_r	Relative permittivity
ϵ_o	Permittivity of free space
θ	Elevation angle
λ	Wavelength
λ_o	Wavelength in free space
μ	Permeability
μ_r	Relative Permeability
μ_r	Permeability of free space
ϕ	Azimuth angle
σ	Conductivity
τ	Delay
τ_r	Delay resolution
ω	Angular frequency

Abbreviations

ASRHAE	American Research Society of Heating and Air-Conditioning
ABC	Absorbing boundary conditions
BER	Bit error rate
B2B	Back-to-back
CW	Continuous wave
CIR	Channel Impulse Response
CTF	Channel transfer function
DOA	Direction of arrival
DOD	Direction of departure
DPADP	Discrete power angle delay profile
DS	Delay spread
DSHT	Direct solar heat transfer
DS-UWB	Direct sequence ultra-wideband
DVB	Digital Video Broadcasting
EIRP	Effective isotropic radiated power
EMRL	European Microwave Research Laboratory
FCC	Federal Communication Commission
FD	Frequency domain
FDTD	Finite-difference time-domain
FFT	Fast Fourier Transform
FHSS	Frequency hopping spread spectrum
FM	Frequency modulation
GPS	Global Positioning System
GSM	Global System for Mobile Communication
IF	Intermediate frequency
IFFT	Inverse Fast Fourier Transform
IR	Infra-red
ISI	Inter symbol interference
LOS	Line-of-sight
LTE	Long Term Evolution
LTE-A	Long Term Evolution-Advance
MPC	Multipath component
NB	Narrow-band
NLOS	Non Line-of-sight
OFDM	Orthogonal frequency division multiplexing
PAN	Personal area network
PCS	Personal Communication System
PDP	Power delay profile
PEC	Perfect electric conductor
PHR	Passband Hermitian Reconstruction
PMC	Perfect magnetic Conductor
QoS	Quality of service

RHCP	Right hand circularly polarized
RMS	Root mean square
RX	Receiver
SIMO	Single Input Multiple Output
SISO	Single Input Single Output
SNR	Signal-to-noise ratio
SOLT	Short Open Load test
TD	Time domain
TE	Transverse electric
TEM	Transverse electromagnetic
TM	Transverse magnetic
TM-UWB	Time modulated ultra-wideband
TRP	Total radiated power
TX	Transmitter
UV	Ultra-violet
UWB-ABS	Ultra-wideband absolute
UWB-REL	Ultra-wideband relative
UWB	Ultra-wideband
VL	Visible light
VNA	Vector Network Analyser
VPL	Vehicle Penetration Loss
V2I	Vehicle-to-Infrastructure
V2V	Vehicle-to-Vehicle
WB	Wideband
WFPL	Window Film Penetration Loss
WLAN	Wireless Local Area Network
WSSUS	Wide Sense Stationary Uncorrelated Scattering
3G	Third generation

Chapter 1

Introduction

In recent years, research in the field of wireless communication has progressed rapidly. Understanding the phenomenon associated with radio wave propagation, in essence, provides a way to accurately characterize environments which assists in the development and optimization of wireless communication systems. With the evolution of Global System for Mobile Communication (GSM) and Personal Communication Systems (PCS), the initial research was consistently focused on the coverage in outdoor and indoor environments. Recently, the provision of reliable in-vehicle coverage has become a major objective of both wireless service providers as well as automotive industry. The demand of this in-vehicle coverage encompasses wide range of communication systems in practice including Digital Video Broadcasting, Terrestrial/Hand-held (DVB T/H, 600 MHz), GSM (900 MHz), Digital cellular system (DCS-1800, 1800 MHz), Global Positioning System GPS (1500 MHz), Personal Communication System (PCS 1900 MHz), Wireless Local Area Network (WLAN) (2.4 GHz, 3.6 GHz, and 5 GHz), Long Term Evolution (LTE and LTE-A) (450 MHz to 5 GHz) etc. The high speed data volume required by these services compels the correct assessment of associated propagation channel for system design implications.

Apart from the traditional scenario, another intriguing research consideration is to develop a networking technology that enables two way data communication from vehicles to outside systems. Applications such as satellite navigation, electronic traffic control and road safety support that comes under the category of vehicle-to-vehicle (V2V) and vehicle-to-infrastructure (V2I) communications are the main requisitioner for this kind of networking technology. The concept of vehicle communication gateway for integrating in-vehicle wireless communication technologies into an IP network is also appealing car-makers and wireless service providers. In a nutshell, automotive and cellular industry is constantly looking forward for an optimum wireless communication technology to meet present and future challenges. Moreover the innovation and advance features in modern vehicles call for a reduction in physical wired connections occupying more space and approaching a limit hence it is an attractive way to shift towards wireless mode removing wire harness. For instance, peripheral monitoring, navigations, security camera etc. are the key focus in this regard. The very fact urges on a prior and veracious knowledge of propagation channels in vehicular environment.

1.1 Background and motivation

Nowadays, the increased use of glass in vehicles allow more solar energy to directly penetrate into vehicles. The direct exposure of solar energy causes a rapid rise in temperature inside vehicle along with an increase concentration of ultraviolet radiation. Solar energy spectrum constitutes three main components: Ultraviolet (UV) radiation, Infra-red (IR) radiation and Visible light (VL). IR radiation makes up to 53 percent of the spectrum, VL 44 percent, and UV radiation 3 percent. These effects directly influence the human presence inside the vehicle and its interior. Prolonged human exposure to UV radiation may result in acute and chronic health effects on the skin, eye and immune system. According to ASRHAE research of solar heat transfer through glass fenestrations [9], when solar energy is incident on a typical glass pane under average meteorological conditions, 6 percent of the solar radiation is reflected, 5 percent is absorbed while rest of 89 percent is transmitted as direct solar heat transfer (DSHT). This heat transfer mechanism from outside to inside vehicle is depicted in Figure 1.1.

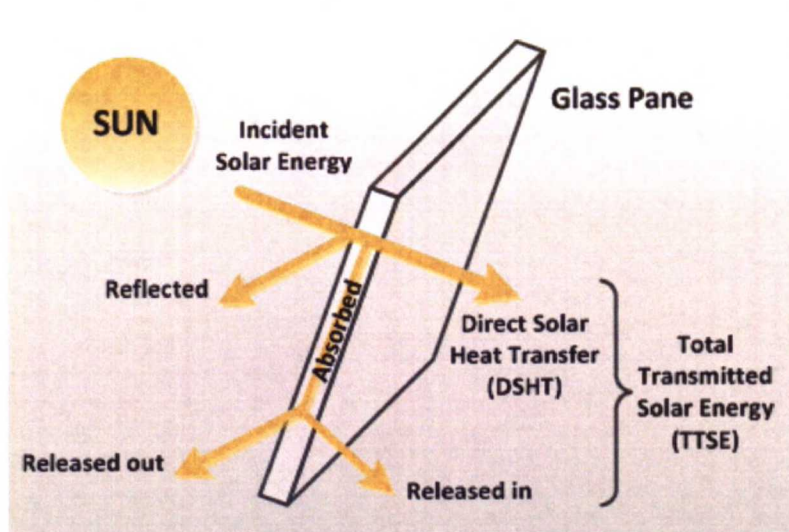


Figure 1.1 Solar energy interaction with a normal glass pane

The energy transfer through this kind of mechanism depends on various factors including characteristics of surface and its orientation, weather and solar radiation conditions. Solar Heat Gain Factor (SHGF) and U-value are the two terms commonly used to quantify this solar energy transfer mechanism. SHGF refers to the total amount of heat flux transmitted through a glazing surface as a heat gain. This includes the amount of energy absorbed by the glass and re-radiated inside. While U-value measures the heat transfer by the method of re-radiation, conduction and convection.

In case of vehicles, when solar energy enters the space inside and combines with the ambient heat already present due to vehicle itself, the vehicle acts as a chamber for the energy trapped due to multiple reflections inside, resulting in an increase in overall temperature. The excess heat is a source of discomfort for people inside

vehicle. For example, when outside temperature is 80 °F, vehicle interior can heat up to 125 °F within few minutes. According to another research by Division of Energy Medicine Stanford University, a vehicle ambient temperature can rise from 72–96 °F to 112–136 °C within initial 30–60 minutes period [10–12]. The most familiar method to combat this heat load is air-conditioning. Whereas, from environmental point of view, air-conditioning is an unfriendly approach as it leads to higher fuel consumption and CO_2 emissions.

An easy way to reduce the solar heat gain inside a vehicle and improve its energy efficiency is to utilize window coating. The use of window coating dates back to 1950s and have been in use ever since with many improvements due to technological advancement. The window film is typically applied to the inner side of a window where it reflects and absorbs heat. Most commercially available automotive window films contain a metallic layer or sometimes are doped with metallic particles of aluminium, steel, silver or combination of these that reflect and absorb the inward radiation. Most of the absorbed radiation is again radiated outwards. In this way, a significant amount of energy is saved from fuel exhausting cooling systems. The window coating also rejects a major portion of harmful ultraviolet radiation. In order to avoid glare and maintain optimum visibility for driving, window coatings comes in tinted form. Hence the use of window coating provides three major benefits for passengers safeguard including heat rejection, protection from UV radiation and glare control.

However, with all benefits that comes with window coating, a radio engineer's perspective would be to consider this coating as a filter for communication signals. It may even cause an additional attenuation of communication signals to several dBs, affecting the in-vehicle coverage adversely for external wireless communication systems. This very reason necessitates the scientific evaluation of the effects of automotive window coating on electromagnetic wave propagation and associated signal attenuation. In scientific standings this attenuation is usually termed as *Vehicle Penetration Loss* or "VPL"¹. The study can broadly influence the design considerations not only for wireless service providers but also for vehicle manufacturers. Based on this sort of analysis, automotive industry can consider manufacturing of window glass in a way to provide both effective communication and protection from solar radiations. Likewise, the placement of communication terminals inside vehicles for high speed data services is crucial, therefore, the analysis can also stipulate intuitive ideas in this respect. Enhanced and better radio coverage is one of the major aims for wireless network providers to sustain Quality of Service (QoS) and hence this study may provide an insight for better radio coverage predictions.

¹To maintain consistency, the term "VPL" is employed throughout this literature.

1.2 Objectives

The goals of this research have been designed to account for the increased interest in wireless communication system performance for in-vehicle coverage by outdoor wireless networks. The prime objectives of this study are thus enumerated as below.

- Characterization of VPL at frequencies that cover all major wireless communication systems with an additional consideration of automotive window coating. The methodical assessment of VPL may evolve in setting a benchmark for defining the coverage and capacity of wireless communication systems to account for communication from external wireless networks to vehicles.
- A thorough radio wave propagation analysis to evaluate the impact of vehicle and human presence on received signal level inside a vehicle, which may provide an insight to underlying propagation phenomena.
- To establish a possibility of full wave numerical analysis for evaluating VPL and its subsequent validation with measurement results.

1.3 Scope of work

The prime focus of this research study will be encircling two main areas that are highlighted below.

(a) Measurement-based analysis

Comprehensive measurements will be performed in an indoor environment considering different measurement scenarios and with different automotive window coatings. The measurement data obtained will be processed by utilizing fine algorithms and will be analysed intensively for VPL and associated propagation phenomena. Additional window film measurements will also be conducted in a shielded environment to characterize penetration loss for two different types of film materials.

(b) Full wave numerical analysis

For reckoning VPL, full wave numerical analysis based on Finite Difference Time Domain (FDTD) method will be considered. For this purpose, commercially available FDTD tool, SEMCAD-X will be used. The theme behind exercising this kind of analysis is to support propagation predictions that are more accurate and computationally efficient in comparison to traditional empirical techniques such as ray-tracing etc.

In order to corroborate a connection between the two areas discussed above, it is essential to consider the practical challenges involved. A great deal of hardship is enfolded in performing measurements since numerous factors are influential which

include appropriate financial resources, hardware implementation and manpower required to accomplish measurement tasks. Furthermore, these factors are subject to variation depending upon the accuracy requirements and environment under consideration. Numerical analysis is yet an alternate way that may provide reasonable and efficient propagation predictions with efforts that are relatively less than measurements. However, the factor that limits the scope of numerical analysis is the availability of computational resources that can hold up the numerical domain.

1.4 Organization of thesis

The thesis is organised in total seven chapters. Chapter 2 to Chapter 6 contain the main body of thesis, each of these begins with a brief introduction and ends with a short summary.

Chapter 1 presents the background and formulates the problem statement. It also defines the objectives and scope of work to accomplish these objectives.

Chapter 2 covers the background theory beginning with ultra-wide band propagation channels and its characteristics and briefly presents ultra-wide band antennas.

Chapter 3 introduces electromagnetic shielding with its mechanisms in order to accentuate the foreground for VPL and eventually the previous VPL investigations have been critically reviewed followed by the contribution of this thesis for filling in the gaps that were left in previous studies.

Chapter 4 describes the measurements performed and methodology employed for conducting these measurements. First, all measurements related to the characterization of VPL are discussed and then additional supporting measurements for window films are presented.

Chapter 5 addresses post-processing of measurement data and in-depth analysis of the results for all measurements that are discussed in Chapter 3.

Chapter 6 is based on numerical analysis of VPL using FDTD electromagnetic full wave solver. In the beginning of the chapter some useful concepts related to FDTD method have been discussed to provide a background before plunging into numerical modelling and simulations. It also gives a brief comparative discourse between measured results described in Chapter 5 and simulated results described in Chapter 6.

Chapter 7 finally concludes the thesis and allows some brisk thoughts for related future work.

Chapter 2

Ultra-wideband antennas and propagation

2.1 Introduction

Wireless communication has revolutionized the field of communication for last two decades and is progressing remarkably with a huge impact on human life and market size. It has enabled people to get closely interconnected with each other through portable and handy wireless devices with reliable voice and data services whereas the business community is always in need of perpetual communication services without disruption to intercommunicate with employees and deal with clients and customers.

As communication technologies evolved, the requirement of bandwidth occupied by communication systems has also increased to satisfy the throughput requirements of modern applications. This trend is dictated by two main factors. First, the data rate, which ranges from a few bits/s to many Gbit/s based on application in question. For instance, sensor networks and basic speech communication requires few kbit/s but on the other hand modern applications such as high speed data services including Wireless Local Area Networks (WLANs), 3G cellular systems and Personal Area Networks (PAN) are data rate starved applications and require hundreds of Mbit/s. Secondly, the multiple access techniques demand resistance to interference rendering high Quality of Service (QoS). In a broader canvas, more bandwidth means more capacity, processing gain and number of users.

With this perspective, ultra-wide band (UWB) having huge available bandwidths has a tremendous attraction for wide range of communication systems. UWB technology has gained substantial interest of research and industry over recent years. Hence Federal Communication Commission (FCC) recognized the importance of UWB technology and authorized its usage. As per FCC definition, “a signal is UWB if it occupies bandwidth larger than 500 MHz or has a fractional bandwidth larger than 20% of the central frequency”¹. The 2002 FCC ruling for UWB sets the radiation limit for UWB indoor and outdoor communication applications and the

¹Fractional bandwidth is based on frequency limits of the bandwidth

$B_{f(-10dB)} = 2 \frac{(f_H - f_L)}{(f_H + f_L)}$ where $f_H = \text{maximum frequency}$, $f_L = \text{minimum frequency}$

spectral mask is shown in Figure 2.1 defining maximum Effective Isotropic Radiated Power (EIRP) for specified frequency range. Due to large bandwidth of UWB systems, they pertain several advantages such as low interference to and from other systems, low sensitivity to fading, accurate ranging and position location etc [13]. UWB systems can be implemented in baseband which eliminates the requirement of an intermediate frequency (IF) stage and hence mixers are not needed. However, there are several other ways of generating UWB signals that includes frequency hopping spread spectrum (FHSS), orthogonal frequency division multiplexing (OFDM), time modulated (TM-UWB) and direct sequence (DS-UWB) techniques.

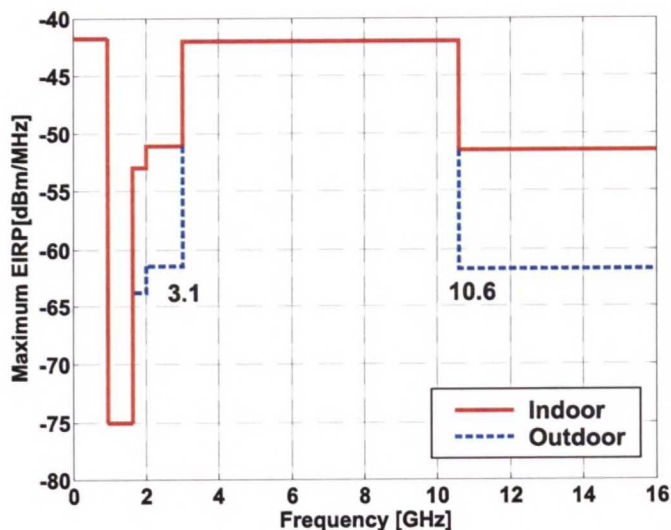


Figure 2.1 FCC spectral masks for indoor and outdoor UWB transmissions

2.2 Ultra-Wideband propagation channels

In contrast with traditional wired communication where a physical medium is used for communication, radio propagation channel is the medium that connects wireless transmit and receive ends. It sets a basic limit on the performance of any wireless communication system. The design, testing and improvement of a wireless communication system critically depends on the implicit understanding of affiliated propagation channel.

Radio waves propagate through free space between a transmitter (TX) and receiver (RX) along direct and indirect paths. The indirect paths arise from the interaction of radio waves with environmental objects. Antenna transmits electromagnetic energy according to its radiation pattern in elevation and azimuth planes. The electromagnetic energy emitted from the TX antenna spreads in space and is a sum of components in different directions. The individual components while propagating through free space undergo various mechanisms, such as reflection, diffraction or scattering, as they interact with different objects in the environment. These mechanisms can change the direction of propagation and even fragment the individual

component into multiple new components. The components adapt different paths and ultimately reach the RX antenna. In this view, the components are called multipath components (MPCs) and the process is termed as multipath propagation. Each MPC can be attributed to particular attenuation, direction of arrival(DOA) at the receiver and delay τ equal to the distance d covered by MPC, $d = \tau c$, where c is the speed of light 3×10^8 m/s. The time domain convolution relation between received signal $y(t)$ and transmitted signal $x(t)$ is given by (2.1).

$$y(t) = h(t) * x(t) + n(t) \quad (2.1)$$

where $h(t)$ is channel impulse response and $n(t)$ corresponds to receiver noise. Propagation environments can be broadly categorized into two types.

- Outdoor environments: These are characterized by large objects such as mountains, buildings, houses, trees etc.
- Indoor environments: These are characterized by relatively small objects such as walls, furniture etc.

A typical outdoor and indoor multipath environments are depicted in Figure 2.2 where an access point is communicating with a client.

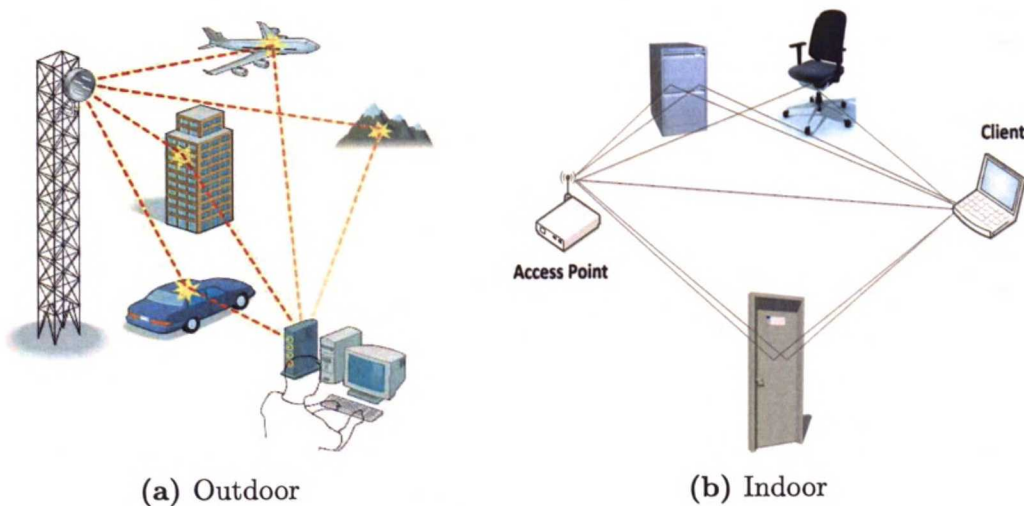


Figure 2.2 Typical multipath propagation environment

2.2.1 Wireless channel representation

The random and time varying wireless propagation channel can be mathematically modelled as a linear time-varied filter with following impulse response [14]:

$$h(t, \tau) = \sum_{k=1}^N a_k(t) \delta(\tau - \tau_k(t)) e^{j\theta(t)} \quad (2.2)$$

where $h(t, \tau)$ is the impulse response at time instant t with delay τ and δ is a Dirac delta function transmitted at $t = 0$. The parameters in (2.2) such as amplitude (a_k), arrival time (τ_k), phase (θ) and number of multipath (N) are attributed to k^{th} path. The model can be generalized to obtain the output of any transmitted signal $x(t)$ at the receiver by convolving it with $h(t)$ and including noise as represented by (2.1).

In general, channels can be differentiated on the basis of their bandwidth into three main types, that are, narrow-band (NB), wide-band (WB) and ultra-wideband (UWB) channels. Following the mathematical model described in (2.2), the individual formulation and representation for each of these channels can be inferred.

A signal centred around a frequency with a small bandwidth is used to stimulate a narrow-band channel. The signal is propagated through multipath environment and reaches RX which experiences an unsteady continuous wave (CW) amplitude envelope due to the vector addition of MPCs. Thus the channel can be represented as:

$$Ae^{j\phi} = \sum_{k=1}^N a_k e^{j\theta_k}. \quad (2.3)$$

A and ϕ corresponds to the amplitude and phase of the received signal. Relation (2.3) implies that one can only draw amplitude and phase information of MPCs which are considered flat over frequency.

For wide-band channels, the frequency response of the channel varies significantly and hence cannot be assumed to be flat over frequency. This frequency response can be transformed into a delay dispersive channel impulse response which is in baseband form as a reduced version of (2.2) can be represented as:

$$h(\tau) = \sum_{k=1}^N a_k \delta(\tau - \tau_k) \quad (2.4)$$

where a_k is the complex amplitude of the k^{th} resolvable path and τ_k is the associated delay.

Ultra-wide band channels having very large bandwidths are distinct and pertain unique characteristics. The physical interpretation of (2.4) suggests a finite number of MPC where each is reflected from a far off object, therefore, the right hand side expression of (2.4) serves an approximate description and do not account for contributions from scattering and diffraction of the waves [15–17]. Also the propagation mechanisms as reflection, diffraction and scattering depends on frequency and cannot be taken as constant for ultra-wide band. The fact makes the ultra-wide band channels highly frequency selective. In this view, the impulse response of a MPC cannot be simply modelled with δ alone instead a distorted pulse $\chi_k(\tau)$ is used to describe distortion that relies on the interaction of MPC with the environment during its journey from TX to RX. The impulse response of an ultra-wide band channel is represented below in which $*$ denotes the convolution [18].

$$h(\tau) = \sum_{k=1}^N a_k \chi_k(\tau) * \delta(\tau - \tau_k). \quad (2.5)$$

The frequency domain variant of (2.5) is given as:

$$H(f) = \sum_{k=1}^N A_k \chi_k(f - k\Delta f) \delta(f - k\Delta f) \quad \Delta f < B_c \quad (2.6)$$

A_k is the complex amplitude at K^{th} frequency bin, N refers to the number of available frequency bins, Δf represents the frequency resolution and B_c is the coherence bandwidth of the channel. The frequency f satisfies $f_L < f < f_H$ where f_L and f_H are the lowest and highest frequencies of ultra-wide band spectrum.

2.2.2 Frequency selectivity of propagation channels

The frequency selectivity of a channel is characterized by the presence of MPCs that are observable by channel impulse response. The parameter that provides the ability to distinguish MPCs is known as delay resolution τ_r which is essentially the inverse of channel bandwidth B i.e. $\tau_r = 1/B$. An intuitive description to understand the nature of MPC can be speculated if we consider the delay range into resolvable delay bins of size equivalent to delay resolution. The Figure 2.3 illustrate a wireless channel for different bandwidth in both frequency and delay domain and provides an intuitive understanding to discriminate between channels on the basis of bandwidth property. The dotted curve represents the true channel behaviour over a segment of large bandwidth. The vertical red arrows and horizontal blue arrows represent the amplitude and delay variation respectively that can be caused due to TX/RX small-scale movements.

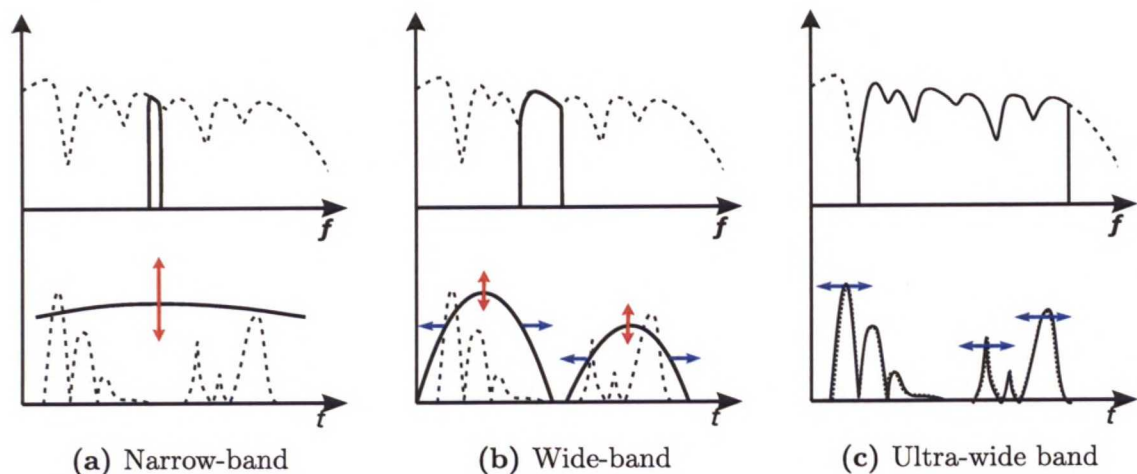


Figure 2.3 Frequency and time domain representation of a channel with different bandwidths

For a narrow-band channel, since the bandwidth is small the delay resolution is extremely low, hence individual MPCs cannot be resolved and all MPCs fall in a single resolvable delay bin as depicted in Figure 2.3a.

For wide-band channels the frequency spectrum varies considerably and therefore, it cannot be considered as flat rather it is frequency selective. The delay resolution for wide-band channels is large in such a way that several delay bins contain MPCs. Due to relatively high delay resolution, small-scale TX/RX variations are translated to channel impulse response. However, individual MPCs are still considered to be frequency flat. Figure 2.3b presents wide-band channel case, where the continuous black curves correspond to the resolvable delay bins in contrast with the true channel scenario depicted with dotted line curve.

UWB channels having large bandwidths render fine delay resolutions. Although, frequency variation exists for complete channel, individual MPCs are also frequency selective. The MPCs falling into delay bins are not resolvable and the overall contribution to delay bins is due to the constructive and destructive interaction of components with different phases. This refers to small scale fading which is described comprehensively in section 2.2.3.3. If the MPCs falling in a same delay bin have almost equal amplitude, the central limit theorem is applied and the amplitude distribution becomes complex Gaussian. The UWB channel is depicted in Figure 2.3c.

The FCC approved definition of an UWB signal stated in Section 2.1 gives a two dimensional picture for the bandwidth of UWB channels. According to the definition, UWB signals are required to satisfy one of the properties: bandwidth larger than 500 MHz which corresponds to “*large absolute bandwidth*” (UWB-ABS) or bandwidth 0.2 times larger than the centre frequency which corresponds to “*large relative bandwidth*” (UWB-REL). An UWB system can be uniquely identified by either one or both of these properties. Consider an UWB signal with lowest and highest boundaries of the spectrum as $f_c - B/2$ and $f_c + B/2$ where f_c is the centre frequency, $|B|$ is the absolute bandwidth and B/f_c is the relative bandwidth.

In case of UWB-ABS, fading cannot be modelled with Rayleigh distribution since less number of MPCs fall in the resolvable delay bins decreases and on the other hand, each resolvable delay bin not necessarily contain MPCs. In this way, delay bins with MPCs and without MPCs are distributed among each other at intervals. More concisely, not every resolvable delay bin contain discrete MPCs and these bin may become overwhelmed with MPCs diffused into each other. For UWB-REL, the distorted pulse $\chi_k(t)$ duration can become larger than the delay resolution. The account for this distortion is thus unavoidable in the channel description. In the UWB spectrum, different frequency components see the environment from their own eye depending upon corresponding wavelengths. The frequency dependence causes dissolution of wide sense stationary uncorrelated scattering (WSSUS) assumption. This premise explains that statistical properties do not change with time and contribution with different delays are uncorrelated.

2.2.3 UWB channel characteristics

The immense bandwidth scope of UWB channels make them unusual and unique thus they behave in a different manner as compared to narrow-band and wide-band channels. It has already been described in the opening remarks of this section that how signal is transmitted from TX, propagates into environment and reaches RX. The environment induces multiplicative processes in the propagating signal due to which received signal show extreme variations in power level. These variations happen on a spatial scale because of two major types of propagation effects that include (a) large-scale effects (b) small-scale effects. Both of these can be filtered from the received signal by necessary signal processing and are quite significant to be examined carefully for effective channel characterization. The small scale effects are described by means of delay characteristics which are the key parameters in system design. The succeeding sub-sections emphasize on different characteristics of UWB channels.

2.2.3.1 Path loss

Signal to noise ratio (SNR) is evaluated through link budget calculations for which correct estimation of the power level is required at receiver. Path loss establishes a basis for link budget calculations and is the ratio of power transmitted P_t to the power received P_r . Path loss determines the physical range of the system for which received signal remains above a certain power level to make communication possible. It provides an insight about the capacity and operation of the system under consideration along with other wireless systems without interference. For UWB antennas matched in both impedance and polarization and transmitting in free space, the received power P_r at RX can be described by the Friis equation as follows:

$$P_r(f) = \frac{P_t(f)G_t(f)G_r(f)}{L_o(f)} \quad (2.7)$$

where $P_t(f)$ is the transmitted power, $G_t(f)$ and $G_r(f)$ are transmit and receive antenna gains respectively. The free space path loss is given as:

$$L_o(f) = \left(\frac{4\pi d}{\lambda} \right)^2 \quad (2.8)$$

Here λ is the wavelength of transmitted signal and d is the separation between TX and RX antennas.

The free space channel itself does not depend upon frequency but we see four frequency dependent quantities in (2.7). This, of-course, is not desirable but presents the reality since UWB antennas are frequency selective. Also constant received power is always preferred, however, for mobile applications it is not possible to employ directional antennas and thus constant gain antennas are used. In case of UWB, the frequency selectivity has grave implications on system design if constant gains for antennas are assumed and causes time dispersion in the received signal. The

frequency selectivity will be elaborated in more detail as subsequent discussion is evolved. The expression (2.8) clearly indicates the distance dependence of path loss and implies that path loss increases with distance between TX and RX antennas due to spreading of energy over larger area. A more generic path loss model representing power law relation is:

$$\bar{L}(d) \propto \left(\frac{d}{d_o}\right)^n \quad (2.9)$$

$\bar{L}(d)$ refers to the mean path loss averaged over spatio-temporal domain. However, the spatial averaging area must be large such that it is greater than the largest wavelength in the signal. The exponential factor n is mean path loss exponent which is the indicator for increase in path loss with distance and depends on the propagation environment, especially, on line-of-sight (LOS) situation between TX and RX. The typical value for path loss exponent for free space is $n = 2$. Path loss exponent can be determined by taking ensemble average of path loss at several distances d . For this purpose, linear regression can be employed to achieve a least square fit to the measurement data. The d_o is the reference distance and usually set to 1 m.

The absolute value of path loss in decibel units can be written as follows and equals to the path loss from TX to RX with reference distance d_o plus additional path loss given by (2.10).

$$\bar{L}(d)_{dB} = L_{dB} + 10n \log_{10} \left(\frac{d}{d_o}\right) \quad (2.10)$$

A path loss model that incorporates both frequency and distance dependency together is highly desirable. For modelling purpose we can make this assumption which is theoretical and supported by recent measurements [19].

$$\bar{L}(f, d) = \bar{L}(f) \cdot \bar{L}(d) \quad (2.11)$$

In the preceding discussion we have seen that frequency dependency in the path loss is introduced mainly through antennas. However, path loss exponent also induces this frequency selectivity through propagation effects due environment. For instance, reflection and diffraction coefficients vary with frequency and hence complicate the overall scenario as bandwidth increases. The relation (2.11) can be further generalized as:

$$\bar{L}(f, d) = f^m \cdot d^n \quad (2.12)$$

where the exponents m and n may or may not be equal. Frequency dependency have been modelled in reference [18] as below:

$$\sqrt{\bar{L}(f)} = f^{-m} \quad (2.13)$$

On the other hand, reference [20] suggested following:

$$\bar{L}(f) = e^{-\delta f} \quad (2.14)$$

The relationship in decibel units was observed by [21, 22]

$$\bar{L}(f) \propto -20\chi \log_{10} \left(\frac{f}{f_o} \right) \quad (2.15)$$

where f_o is reference frequency and χ is a frequency decay coefficient whose value depends on environment. Recently, [18] introduced *frequency-dependent path loss* relation as:

$$G(f, d) = \frac{1}{\Delta f} E \left\{ \int_{f-\Delta f/2}^{f+\Delta f/2} |H(\tilde{f}, d)|^2 d\tilde{f} \right\} \quad (2.16)$$

where $H(f, d)$ refers to channel transfer function including antennas and E is the expectation over large and small scale fading. Δf corresponds to the step frequency range and so chosen that reflection coefficients, diffraction coefficient and dielectric constants remain constant within this bandwidth.

2.2.3.2 Large-scale fading: shadowing

The strength of the received signal fluctuates when TX or RX moves over relatively large distance, e.g., 10λ or more. These random variations averaged over the small spatial area is referred as shadowing. Shadowing happens when large scale fixed objects shadows off (attenuate) the radio signal as it propagate through the environment. This effect is influenced to a great extent by the interaction of radio signal with the environment. The random behaviour of the received signal pertains slow variations and therefore also termed as slow fading or large scale fading. The boundaries of shadowing effect lies between path loss and small-scale fading and for UWB case this distinction is challenging. Also recognizing the correct averaging area is very important but still a subtle notion and an unsolved problem. Literature consistently assumes the narrow-band shadowing to be log-normal distributed. Measurements have shown that this assumption is true for UWB channels as well. Hence path loss at a specific location is log-normally (i.e Gaussian in dBs) distributed about the mean value which is given as:

$$\bar{L}(d)_{dB} = L_{dB} + 10n \log_{10} \left(\frac{d}{d_o} \right) + X_\sigma \quad (2.17)$$

where X_σ is a zero mean Gaussian distributed random variable with standard deviation σ both in dB scale. The parameters n path loss exponent and σ depends on propagation conditions and can be determined from measurements. Most prominent conditions are TX-RX separation d , LOS and non line-of-sight (NLOS) scenarios. Extensive UWB indoor channel measurements were performed by [23] in several homes and suggested that values of path loss exponent n varies with different home locations and have normal distribution $N[\mu_n, \sigma_n]$. It is given as:

$$n = \mu_n + N_1\sigma \quad (2.18)$$

where N_1 is a zero-mean Gaussian variable of unit standard deviation $N[0, 1]$. Also, the shadow component X_σ also varies within the homes and is also a zero-mean Gaussian variable and can be represented as:

$$X_\sigma = N_2\sigma \quad (2.19)$$

where σ is given as:

$$\sigma = \mu_\sigma + N_3\sigma_\sigma \quad (2.20)$$

where N_2 and N_3 are also zero-mean Gaussian variables with unit standard deviation $N[0, 1]$. The expression in (2.17), thus, can be transformed as:

$$\bar{L}(d)_{dB} = \left[L_{dB} + 10\mu_n \log_{10} \left(\frac{d}{d_o} \right) \right] + \left[N_1\sigma_n \log_{10} \left(\frac{d}{d_o} \right) + N_2\mu_\sigma + N_2N_3\sigma_\sigma \right] \quad (2.21)$$

In case of path loss exponent n the normal distribution reported for LOS is $N[1.7, 0.3]$ and for NLOS is $N[3.5, 0.97]$. Similarly, in case of shadowing component X_σ , the normal distribution reported is $N[1.6, 0.5]$ and for NLOS is $N[2.7, 0.98]$.

Since UWB is usually employed for short range applications as compared to cellular systems thus they call upon less shadowing effect. A typical shadowing scenario is depicted in Figure 2.4 where propagating signals from base station (BS) are shadowed by a building before arriving at mobile station (MS).

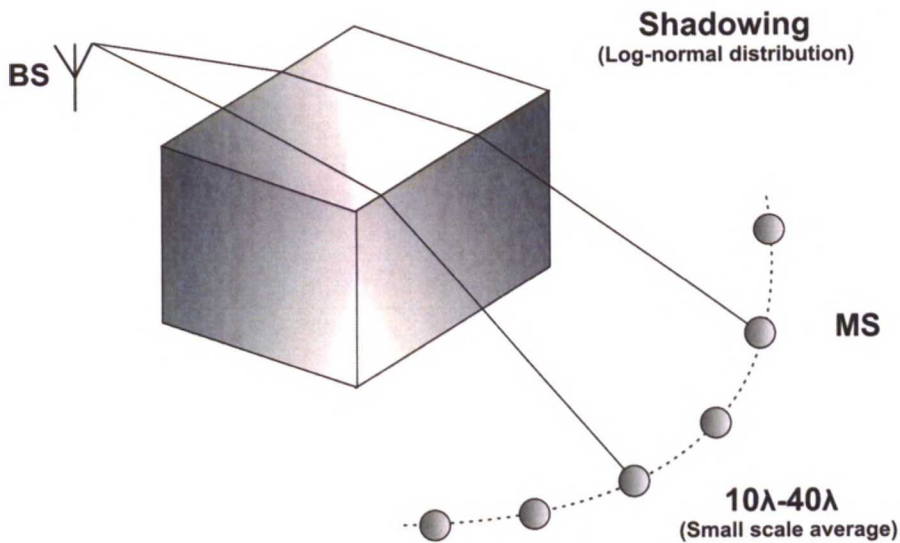


Figure 2.4 Shadowing effect due to building obstacle

2.2.3.3 Small-scale fading

Small-scale fading is a process that makes the received signal strength to fluctuate more rapidly due to multipath and can be encountered for small displacements of TX or RX. These displacement can be less than a wavelength for small-scale fading to materialize. Because of large fluctuations it is also know as fast fading. The multipath propagation results in different copies of the transmitted signal which arrive at RX from different directions and delays. These MPCs at a point in space have random distributions for amplitudes and phases. The interference of MPCs causes distortion or more simply, fading. In and out of phase MPCs with different amplitudes give rise to either constructive or destructive interference. Fading can occur due to the relevant motion of TX/RX or the objects in propagation environment or both. When objects in the propagation environment are stationary and only TX or RX are subject to motion, the fading can be seen entirely as a spatial phenomenon. However, RX perceives these spatial variations totally in temporal domain. As a worst case it may happen during communication at a particular location where signal experiences a deep fade. When a relative motion exists between the TX and RX, each MPC suffers from a frequency shift which is usually termed as Doppler shift and depends on the velocity and direction of motion of TX and RX.

Although UWB systems hold very fine time resolution, it is still a possibility that different MPCs fall into a single resolvable bin and add together to produce fading. By comparing the small-scale fading effect for UWB with other systems, the difference is evident for number of MPCs within a resolvable delay bin. The number of MPCs dropping into a single resolvable delay bin is affected by three main factors, that are; (i) complexity of propagation environment (ii) measurement bandwidth

The environment determines the number MPCs to exist. Large number of objects in the environment results into more MPCs [13]. Large bandwidth means short period of a resolvable delay bin which decreases the number of MPCs per delay bin whereas, large delays provides a feasibility of more paths that can exist on these delay and hence depth of the fading can increase. The narrowband systems utilizes Rayleigh distribution for time varying received signal but due to the factors discussed above, Rayleigh distribution may not be appropriate to describe the amplitude variation of MPCs. Therefore, alternative distributions need to be considered and some of these are briefly discussed below.

- **Rayleigh distribution**

The most commonly employed model for small-scale amplitude distributions in the absence of LOS component is Rayleigh distribution. But it may not suitable UWB propagation channels. The Rayleigh distribution is an envelope of complex Gaussian signal. The probability distribution function *pdf* for Rayleigh distribution is given as:

$$p(x) = \frac{x}{\sigma^2} \exp\left(-\frac{x^2}{2\sigma^2}\right) \quad (2.22)$$

where standard deviation σ is the rms value of the received signal voltage and variance σ^2 is the time averaged power of the received signal.

- **Ricean distribution**

When small-scale fading signal envelope has a dominant and non-fading component such as LOS component along with many other small components, the envelope follows Ricean distribution. If LOS component becomes weaker Ricean distribution approaches Rayleigh distribution. The Ricean distribution is given as:

$$p(x) = \begin{cases} \frac{x}{\sigma^2} e^{-\frac{(x^2 + A^2)}{2\sigma^2}} I_0\left(\frac{Ax}{\sigma^2}\right), & \text{for}(A \geq 0, x \geq 0) \\ 0, & \text{for}(x < 0) \end{cases} \quad (2.23)$$

where A is the amplitude of LOS component and $I_0(\cdot)$ denotes the Bessel function of zero order.

- **Nakagami distribution**

Nakagami probability distribution function *pdf* is given as:

$$p(x) = \frac{2}{\Gamma(m)} \left(\frac{m}{\Omega}\right)^m x^{2m-1} \exp\left(-\frac{m}{\Omega}x^2\right) \quad (2.24)$$

where $m > 1/2$ is Nakagami *m-factor* or *shape factor*, $\Gamma(m)$ is the gamma function and Ω is the mean square value of the amplitude. The *m-factor* is usually modelled as a random variable [24]. Nakagami distribution was suggested for UWB by [25], [26], [24].

- **Log-normal distribution**

Log-normal distribution was suggested for UWB by [27] and is given as:

$$p_x(x) = \frac{20/\ln(10)}{x\sigma_x\sqrt{2\pi}} \exp\left[-\frac{(20\log_{10}(x) - \mu_{dB})^2}{2 \cdot \sigma_x^2}\right] \quad (2.25)$$

where σ_x is the standard deviation of x and μ_{dB} is the mean value of $|x|$ expressed in dB. Log-normal distribution has an advantage that both large and small-scale fading have the same form since superposition of log-normal variables can be approximated by a log-normal distribution [28].

2.2.3.4 Path loss, shadowing and small-scale fading: one picture

To sum up the preceding discussion, it would be more appropriate to present large-scale and small-scale propagation phenomenon in a graphical form with respect to the received signal at RX. Figure 2.5 demonstrates the underlying dynamics of received signal. Let us consider a hypothetical route on which TX moves shown along the horizontal axis of the Figure 2.5. As TX travels along the route, the received signal experiences fluctuation in the power level shown along the vertical axis of Figure 2.5 due to the interaction of transmitted signal with propagation environment. The blue curve represents the received power exhibiting small-scale fading. By averaging over small spatial area, shadowing variations can be seen in the grey curve. These averaged shadowing variations then follow large-scale path loss in dashed black curve.

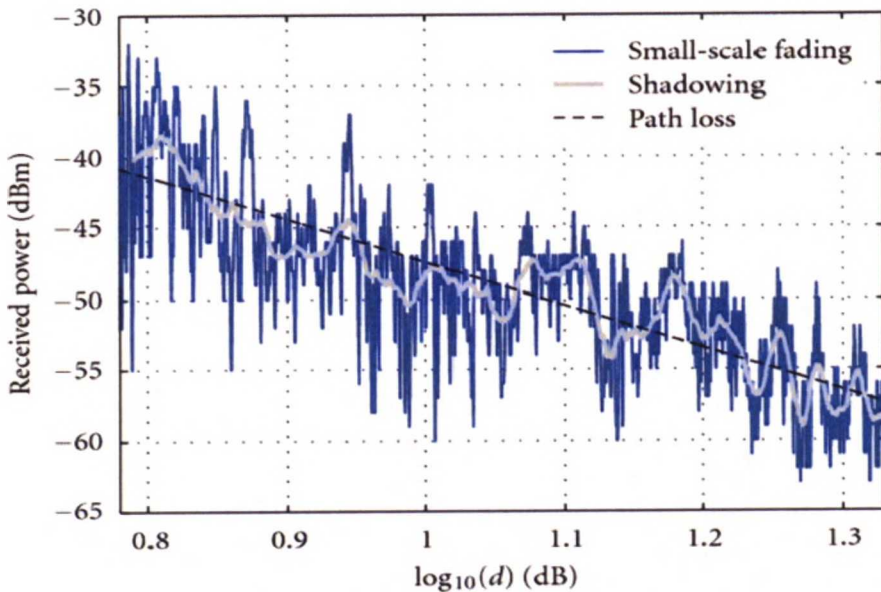


Figure 2.5 Underlying dynamics of received signal [8]

2.2.4 Reflection, transmission and scattering from materials

2.2.4.1 Reflection and transmission

When a radio wave propagating through the environment is impinged on an interacting object which have different electrical properties as compared to the propagation medium, part of the wave is reflected while rest is transmitted or absorbed as heat. Radio wave is an electromagnetic wave with electric and magnetic field components perpendicular to each other and direction of propagation. Electromagnetic waves posses certain polarization which means it can be represented as a sum of two orthogonal instantaneous electric field components oriented in space. These orthogonal field components are sometimes designated as vertical and horizontal components. The orientation of these components may remain fixed (linear polarization) or vary with time (circular or elliptical polarization). The interaction of an electromagnetic wave with the interface of an object can be differentiated between two cases. When electric field component is parallel and magnetic field component is perpendicular to the incident plane, it is said to be parallel polarization and the wave is distinguished as Transverse Magnetic (TM) wave. Similarly, when electric field component is perpendicular and magnetic field component is parallel to the incident plane, it is said to be perpendicular polarization and wave is distinguished as Traverse Electric (TE) wave. The amount of power that arrives to RX is determined by *Fresnel reflection coefficient* Γ and the direction of reflection. Reflection coefficient depends on material properties, polarization of the wave, angle of incidence and frequency of the wave. The discussion here concerns *specular reflections* that appears when wave is incident onto a smooth surface with large dimensions comparable to the wavelength.

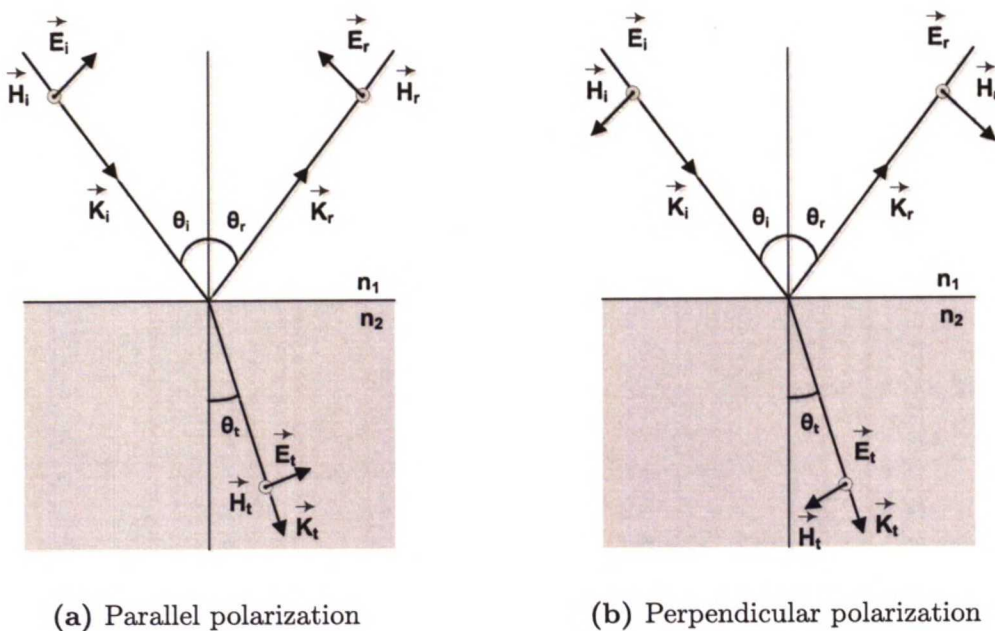


Figure 2.6 Radio wave incident on a surface

Figure 2.6 describes the phenomenon discussed above for the two polarizations. The wave impinges with an angle of incidence θ_i on the boundary between two dielectric media with having refractive index n_1 and n_2 respectively. The energy is partly reflected back into the same medium at an angle θ_r while some energy is transmitted into the second medium with angle θ_t . The respective direction of propagation is represented by propagation vector k . Subscripts i , r and t are attributed to incident, reflected and transmitted field parameters respectively. Refractive index n is a quantity that dictates propagation of waves in medium and equals $\sqrt{\epsilon_r \mu_r}$ where ϵ_r and μ_r relative permittivity and permeability of the media. Both are related to the free space values as $\epsilon = \epsilon_0 \epsilon_r$ and $\mu = \mu_0 \mu_r$. The free space constants are given by $\epsilon_0 = 8.85 \times 10^{-12} F/m$ and $\mu_0 = 4\pi \times 10^{-7} Wb/A \cdot m$. If the material is lossy it will absorb energy and can be described by complex dielectric constant as:

$$\epsilon = \epsilon_0 \epsilon_r - j\hat{\epsilon} \quad (2.26)$$

where $\hat{\epsilon}$ is complex permittivity,

$$\hat{\epsilon} = \frac{\sigma}{2\pi f} \quad (2.27)$$

and σ is the conductivity of the material in S/m and f refers to the carrier frequency. For good conductors, ϵ_r and σ do not rely on frequency but for dielectric materials they are certainly sensitive to frequency. Reflection and transmission coefficients can be calculated by applying boundary continuity conditions for which the tangential field components must remain same on both sides of the material interface. According to the *Snell's law* the angle of incidence must be equal to angle of reflection and is given as:

$$\theta_i = \theta_r \quad (2.28)$$

Thus, the angle of the transmitted wave is related as:

$$\frac{\sin \theta_t}{\sin \theta_i} = \frac{\sqrt{\mu_1 \epsilon_1}}{\sqrt{\mu_2 \epsilon_2}} = \frac{n_1}{n_2} \quad (2.29)$$

where ϵ_1 , μ_1 and ϵ_2 , μ_2 are permittivity and permeability of the two media. Let's assume that $\mu_1 = \mu_2 = \mu_0$ which is true for most cases of interest such as radio waves propagating in free space and interact with some object in the environment, hence, implies that first medium is free space. Hence (2.29) reduces to

$$\frac{\sin \theta_t}{\sin \theta_i} = \frac{\sqrt{\epsilon_1}}{\sqrt{\epsilon_2}} = \frac{n_1}{n_2} \quad (2.30)$$

For the two orthogonal polarizations (*i*) *parallel polarization* and (*i*) *perpendicular polarization*, the reflection coefficients and transmission are given as:

$$\Gamma_{\parallel} = \frac{E_r}{E_i} = \frac{\sqrt{\frac{\epsilon_2}{\epsilon_1} - \sin^2 \theta_i} - \frac{\epsilon_2}{\epsilon_1} \cos \theta_i}{\sqrt{\frac{\epsilon_2}{\epsilon_1} - \sin^2 \theta_i} + \frac{\epsilon_2}{\epsilon_1} \cos \theta_i} \quad (2.31)$$

$$T_{\parallel} = \frac{E_t}{E_i} = \frac{\sqrt{\frac{\epsilon_2}{\epsilon_1}} \cos \theta_i}{\sqrt{\frac{\epsilon_2}{\epsilon_1} - \sin^2 \theta_i} + \frac{\epsilon_2}{\epsilon_1} \cos \theta_i} \quad (2.32)$$

$$\Gamma_{\perp} = \frac{E_r}{E_i} = \frac{\cos \theta_i - \sqrt{\frac{\epsilon_2}{\epsilon_1} - \sin^2 \theta_i}}{\sqrt{\frac{\epsilon_2}{\epsilon_1} - \sin^2 \theta_i} + \cos \theta_i} \quad (2.33)$$

$$T_{\perp} = \frac{E_r}{E_i} = \frac{2 \cos \theta_i}{\sqrt{\frac{\epsilon_2}{\epsilon_1} - \sin^2 \theta_i} + \cos \theta_i} \quad (2.34)$$

Following the *Snell's law*, the relationship between incident, reflected and transmitted fields is give as:

$$E_r = \Gamma E_i \quad (2.35)$$

and

$$E_t = (1 + \Gamma) E_i \quad (2.36)$$

For layered dielectric structures where incident wave from one medium penetrates the second medium and emerges in the third medium, the problem is different. This resembles to the situation when radio waves penetrate buildings from outdoor to indoor communications or vice-versa. For realistic case of interest as mentioned earlier, the situation of radio wave propagation in free space within an environment, the dielectric material is surrounded by free space air. The total reflection and transmission coefficients can be determined by manipulating partial waves and are given as:

$$\Gamma = \frac{\Gamma_1 + \Gamma_2 e^{-2j\alpha}}{1 + \Gamma_1 \Gamma_2 e^{-2j\alpha}} \quad (2.37)$$

$$T = \frac{T_1 T_2 e^{-j\alpha}}{1 + \Gamma_1 \Gamma_2 e^{-2j\alpha}} \quad (2.38)$$

where T_1 is the transmission coefficient from air to dielectric and T_2 is from dielectric to air. Parameter α is the electrical length of dielectric layer which depends upon frequency of the wave, incident angle θ_t and dielectric constant ϵ of the material and is given as:

$$\alpha = \frac{2\pi}{\lambda} \sqrt{\epsilon_r} d \cos \theta_t \quad (2.39)$$

Perfect electric conductors do not allow electromagnetic waves to pass through, therefore, all the energy is reflected back to the same medium. In order to satisfy boundary conditions, we follow *Snell's law* from (2.28). Hence the relationship

between incident and reflected electric field with respect to the plane of incidence are given as:

$$E_i = E_r \quad (\text{Parallel}) \quad (2.40)$$

$$E_i = -E_r \quad (\text{Perpendicular}) \quad (2.41)$$

With reference to (2.40) and (2.41), the reflection coefficients for the two polarizations are $\Gamma_{\parallel} = 1$ and $\Gamma_{\perp} = -1$ where transmission coefficients $T = 0$ for both polarizations.

2.2.4.2 Surface scattering

Scattering of electromagnetic waves from rough surfaces is a significant phenomenon that determines nature of MPCs in a propagation environment. However, it is important to consider the amount of surface roughness in order to evaluate the degree of scattering.

Kirchoff's theory investigates scattering phenomenon in an adequate and simple manner. It does not require detailed information rather only the distribution of height variations are required. The theory makes a plain assumption that scattering points on the surface do not affect each other for small height variations which may not be a case in actual. Nevertheless, with the given assumption fulfilled, it imposes a certain impact on the incident radiation. The power of specular reflected energy decreases and causes energy to spread in different directions. The effective reflection coefficient Γ_{rough} which deals with decrease in power specularly Gaussian distribution for the height variations is given by:

$$\Gamma_{rough} = \Gamma_{smooth} e^{-2(k_0 \sigma_h \sin \phi)^2} \quad (2.42)$$

where σ_h refers to the standard deviation of the height distribution, k_0 is the wavenumber $2\pi/\lambda$, and ϕ is the incident angle. It may be worth to note that for incident angle $\phi = 0$, the surface appears to be smooth to the incident radiation and reflected energy become specular again. The relation (2.42) exhibits strong frequency dependence. Figure 2.7 demonstrate the scattering phenomenon from the rough surfaces in contrast with specular reflection.

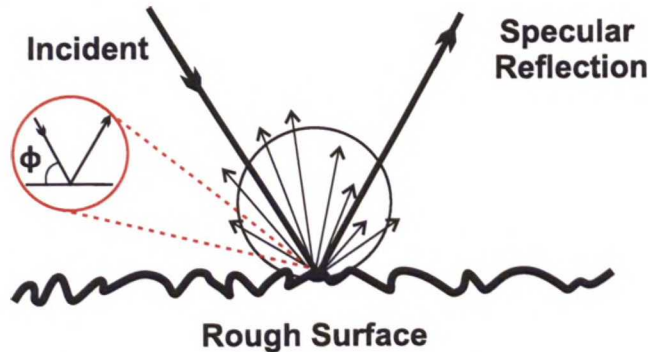


Figure 2.7 Scattering from rough surfaces

2.2.5 Delay domain channel expressions

Two main channel delay parameters, (i) power delay profile (*PDP*) and (ii) Root mean square (RMS) delay spread, that significantly affect system performance are discussed here in detail. Several standard channel impulse response models have also been discussed under the power delay profile.

2.2.5.1 Power delay profile (PDP)

For an UWB signal propagating through a time invariant channel, the average received power as a function of time delay is known as *power delay profile* or simply *PDP*. It defines the power decay of MPCs. The power delay profile of an UWB channel can be evaluated by taking spatial average of magnitude squared channel impulse response over a local area. In more generic terms, propagation channel snapshots at different instants averaged over a local area provides a time invariant power delay profile. It is given as:

$$P(\tau) = E [|h(t, \tau)|^2] = \sum_{k=1}^N a_k^2 \delta(\tau - \tau_k) \quad (2.43)$$

where $E[\cdot]$ defines the ensemble over time. Power delay profile is considered to be a key parameter from system design perspective as its shape reflects channel conditions. It varies from environment to environment. The most common model to represent a power delay profile is exponential decay model and is given as:

$$P(\tau) = \frac{1}{\gamma_d} \exp\left(-\frac{\tau}{\gamma_d}\right) U(\tau) \quad (2.44)$$

where γ_d is the delay decay factor and $U(\tau)$ is the Heaviside step function.

Some main attributes of a power delay profile are excess delay, total excess delay and mean delay. These terms are briefly explained as below:

- **Excess delay:** Power delay profile can be discretised in k individual MPCs in the delay range each having power P_k . The delay of any MPC with respect to the first arriving dominant component or LOS component is called excess delay.
- **Total excess delay:** The delay difference between very first component and the last MPC is referred as total excess delay.
- **Mean delay:** The delay corresponding to the centre of gravity of the profile is known as mean delay and is given as:

$$\tau_0 = \frac{1}{P_T} \sum_{k=1}^N P_k \tau_k \quad (2.45)$$

where P_T is the total power in the channel.

In outdoor environments, the objects are scattered over large distances. On the other hand, the indoor environment are cluttered with objects that are randomly distributed in a small area. More specifically the objects are clustered in the form of groups and these groups can be distinguished from each other by delay differences. This clustering is clearly reflected in the power delay profile as MPCs also arrive in the form of clusters. Location of objects in propagation environment influence MPCs and if the propagating wave experiences a single interaction with an object, the path can be precisely identified by means of simple geometry. Some practical and well known delay domain channel models are discussed in Section 2.2.6 which provide more insight to MPC arrival with respect to the indoor environments.

2.2.5.2 RMS delay spread

RMS delay spread is defined as *the square root of second central moment of power delay profile* and is given as:

$$\tau_{RMS} = \sqrt{\frac{1}{P_T} \sum_{k=1}^N P_k \tau_k^2 - \tau_0^2} \quad (2.46)$$

where P_T is the total power and τ_0 is the mean delay given by (2.45).

The RMS delay spread considers the relative power of MPCs and characterizes delay dispersion, therefore, it is considered to be the most powerful description of the channel as it affects the important properties of the communication system. It does not depend on the mean delay and the path length acquired by MPC since it is defined only by the relative path delays. It indicates the bit error rate (BER) performance of a system for delay spreads within in one symbol duration. If RMS delay spread is much less than the symbol duration, inter-symbol interference (ISI) is avoided and hence channel can be considered as frequency-flat. Mathematically, RMS delay spread is related with bit-error-rate (BER) as:

$$\overline{BER} = K \left(\frac{\tau_{RMS}}{T_B} \right) \quad (2.47)$$

where T_B is the bit duration and K is the proportionality constant which depends on the modulation technique used. Typical values for indoor industrial environment ranges from 50-200 ns [18].

2.2.6 Delay domain channel models

2.2.6.1 Saleh-Valenzuela model

It is one of the most popular statistical model for indoor channel impulse response [29]. The theme behind this modelling was to envision the clustering nature of MPCs arriving at RX after going through various interactions in the propagation environment in a typical NLOS scenarios but it also proves to be valid for LOS conditions. The model considers two main mechanism (i) cluster arrival process and (ii) ray arrival process. Both processes deals with individual entities, i.e., amplitude and arrival times of clustered and ray MPCs. Mathematically it is given as:

$$h(\tau) = \sum_{l=0}^L \sum_{k=0}^K \beta_{k,l} \delta(\tau - T_l - \tau_{k,l}) \quad (2.48)$$

where T_l refers to the arrival time of l th cluster, $\beta_{k,l}$ and $\tau_{k,l}$ are the amplitude and arrival time respectively for k th ray inside l th cluster. Also L and K in the summations represents the number of clusters and number of rays within a cluster. The rate at which a particular cluster arrives is accounted with Poisson process and therefore, cluster arrival times T_l are described by exponential random variables as:

$$p(T_l|T_{l-1}) = \Lambda \exp[-\Lambda(T_l - T_{l-1})] \quad l > 0 \quad (2.49)$$

where Λ is the mean cluster arrival rate. Now within individual clusters, the ray arrivals are also characterized by Poisson process and described as:

$$p(\tau_{k,l}|\tau_{(k-1),l}) = \lambda \exp[-\lambda(\tau_l - \tau_{(l-1),l})] \quad k > 0 \quad (2.50)$$

where λ is the mean ray arrival rate. The average power of both clusters and rays within these clusters is assumed to decrease exponentially. The average power of a MPC is at a some given delay, $T_l + \tau_{k,l}$ is given as:

$$\langle \beta_{k,l}^2 \rangle = \langle \beta_{0,0}^2 \rangle \exp\left[-\frac{T_l}{\Gamma}\right] \exp\left[-\frac{\tau_{k,l}}{\gamma}\right] \quad (2.51)$$

where $\langle \beta_{0,0}^2 \rangle$ is the ensemble average of the power of first arriving MPC, Γ is the decay exponent of the cluster and γ is the decay exponent of the rays in the l th cluster. The expression in (2.51) describes the power delay profile of Saleh-Valenzuela model.

As characterised by a Poisson process, the amplitude of each MPC is considered to be a random variable about an exponential average and the assumption in the model that various MPC delays are not resolvable by the measurement system implies the use of Rayleigh distribution for the amplitudes of MPCs. However this assumption is somehow refutable for UWB propagation channels. In effect of this, many researches render the use of log-normal or Nakagami distributions, whatever provides the best fit. For log-normal distribution, the amplitude of MPC is given as:

$$\beta_{k,l} = p_{k,l} 10^{(\mu_{k,l} + X_{\sigma,k,l}/20)} \quad (2.52)$$

where

$$\mu_{k,l} = \frac{10 \log(\langle \beta_{0,0}^2 \rangle) - \frac{10T_l}{\Gamma} - \frac{10\tau_k}{\gamma}}{\log 10} - \frac{\sigma^2 \log 10}{20}$$

and

$$X_{\sigma,k,l} = N(0, \sigma^2) \quad (\sigma \text{ in dB})$$

where σ is the standard deviation of log-normally distributed MPC power and is combination of variations from both clusters and rays with the clusters. The principle Saleh-Velenzuela model power delay profile is depicted in Figure 2.8.

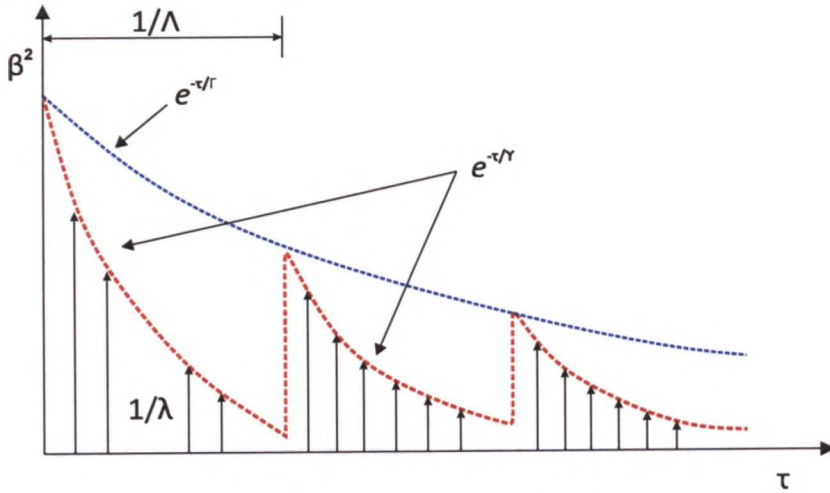


Figure 2.8 Saleh-Velenzuela model

2.2.6.2 The Δ -K model

Like Saleh-Velenzuela model, Δ -K model [14, 30] assumes the clustering properties of MPCs in a channel. The model correlates the arriving components by means of two parameters namely Δ and K . The probability of arriving MPC at some delay is larger by a specific value of K if the MPC has arrived in last Δ seconds. The model exists in a two-state Poisson process. The initial state is S1 while the second state is termed as S2. In the first state S1, the mean arrival rate of MPCs is $\lambda(\tau)$. Soon as MPC reaches RX, the transition to state S2 takes place and the mean arrival rate transforms into $K\lambda(\tau)$. If arriving MPCs fall to zero in next Δ seconds, the process regains its initial state S1. The complete model can, therefore, be described by the transitions between two states. If $\Delta=0$ or $K=1$, the model reformulates itself to standard Poisson process. For $K > 1$, the arriving MPC at any instant of time increases the probability of another MPC in the next Δ seconds. On the contrary, if $K < 1$, the probability of arriving more MPCs in Δ seconds decreases after an individual MPC has already arrived. A discrete form of $\Delta - K$ model has been depicted in Figure 2.9.

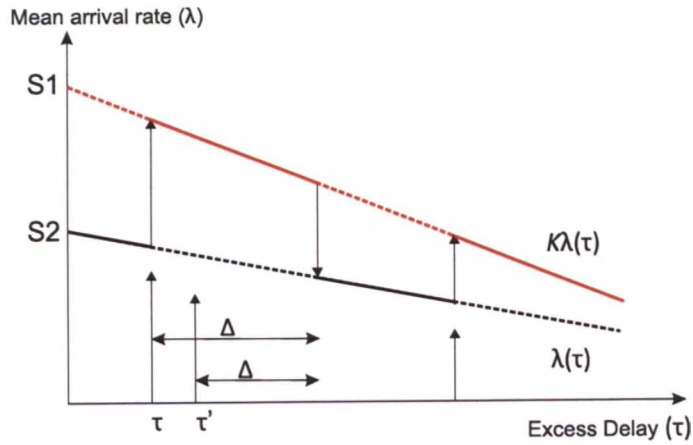


Figure 2.9 The Δ -K model

2.2.6.3 The two-cluster model

The model was proposed by [31, 32] for UWB channels. A evident, from Saleh-Valenzuela and Δ -K model, the channel impulse response is overwhelmed with exponentially decaying clusters. On the other hand, some empirical data suggests the presence of a few clusters only which may be due to short measurement ranges in UWB. The two-cluster model assumes only two clusters in channel impulse response following Poisson arrival times where one cluster is delayed by τ_1 relative to the other as illustrated in Figure 2.10. The first cluster contains strong MPCs which decay quickly and size of the cluster is relatively short compared to the second cluster. While the second cluster is longer consisting of slow decaying MPCs. The first cluster is characterized by parameters $\lambda_1, \sigma_1, \gamma_1$. Similarly second cluster is defined by the parameters $\lambda_2, \sigma_2, \gamma_2$. These refers to the mean arrival rate, standard deviation and decay factor respectively. The channel impulse response finally contains a delayed version of first cluster i.e. second cluster starting from τ_1 where the first cluster is weighted higher by a factor α in order to maintain the continuity in the decay of energy.

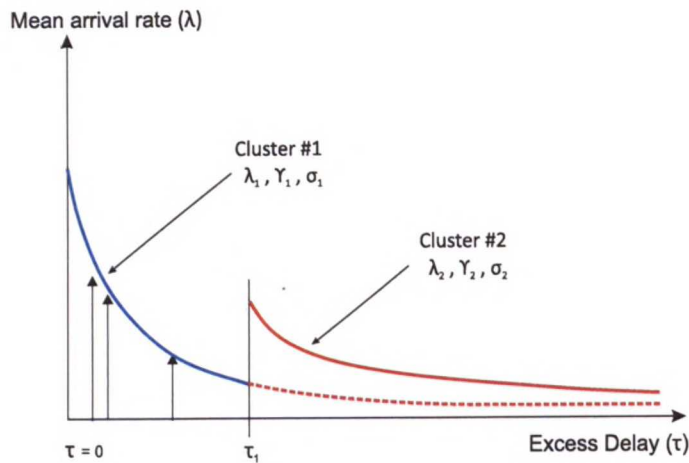


Figure 2.10 The two-cluster model

2.2.6.4 The single Poisson model

The single Poisson model as a simple form of preceding two models. It considers only one cluster in channel impulse response which exhibits no other cluster of MPCs in it. The arrival times follows a Poisson distribution. The probability of l arriving MPCs within an interval T is given as [33]:

$$P(L = l) = \frac{\mu^l e^{-\mu}}{l!} \quad (2.53)$$

where $\mu = \int_T \lambda(t) dt$ is known as Poisson parameter and $\lambda(t)$ is the mean arrival rate. The decay of the MPCs is considered to be exponential with the decay time constant as γ and is given as:

$$p(x) = \lambda e^{-x/\gamma} \quad (2.54)$$

The single Poisson model is depicted in Figure 2.11 below.

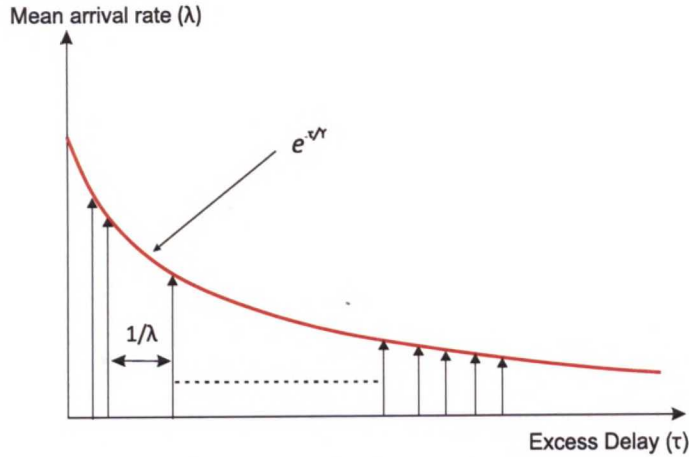


Figure 2.11 The single Poisson model

2.2.7 UWB channel measurement techniques

For the characterization of propagation channels, different measurement techniques exist. However, channel measurements can be broadly classified into two categories: (i) time domain (TD) and (ii) frequency domain (FD). These techniques are quite popular and commonly employed for UWB channel measurements. A comprehensive description of both techniques is presented in this section along with brief account of their advantages, disadvantages and limitations.

2.2.7.1 Time domain (TD) channel measurements

Time domain measurement technique can be practised as a direct method to characterize UWB propagation channels. In an idealistic approach, the impulse response offer complete characterization of a channel over the entire frequency band of use. However, it is not possible to directly measure the actual impulse response of a channel since that requires an ideal dirac-delta excitation signal which has an infinite flat spectrum and is not physically implementable. In order to decrease the effect of measurement system on the estimates of propagation channel, the excitation needs to be close enough to dirac-delta function, otherwise it has to be excluded from the measured impulse response by a deconvolution process such as one suggested by [34] which in turn can cause additional noise and errors.

In practice, very short duration pulses of width T_w are transmitted over the channel and on the receiving side, the signal enters a wideband filter ($BW = 2/T_w$), amplified and detected typically with a digital sampling oscilloscope. The received signal $y(t)$ is the convolution $*$ of the probing pulse and channel impulse response $h(t, \tau)$ given by:

$$y(t) = h(t, \tau) * \prod_{T_w}(t) \quad (2.55)$$

Where $y(t)$ is a close approximation of channel impulse response $h(t, \tau)$ and $\prod_{T_w}(t)$ represents the pulse train. The shorter the pulse width utilized, wider bandwidth can be achieved for which channel characteristics can be measured. The minimum resolvable delay between MPCs is equivalent to the width of the probing pulse. The digital oscilloscope receives a sequence of pulse waveforms with a certain repetition rate and takes one sample per waveform. The time difference between two successive samples equals to the pulse repetition interval T_r with an additional displacement in time T_s i.e. sampling time. If N_s number of samples are required to reconstruct one pulse, the time period T_s consumed for single measurement is given as:

$$T_m = N_s T_r \quad (2.56)$$

Figure 2.12 refers to a typical time domain channel measurement set-up illustrating transmit and receive sides. TX includes a pulse generator injecting short pulses in the channel, a low noise amplifier for amplifying the transmitting signal. The RX comprises of a wide bandpass filter, amplifier and sampling oscilloscope.

One of the main issues with time domain measurements is that they are susceptible to noise due to wideband filter whose bandwidth BW is determined by the multipath resolution i.e. transmitted pulse width T_w . Also the pulse generator characteristics to trigger pulses affect the measurements. Another disadvantage may be experienced by time domain measurements is the phase errors due to detection process. A careful synchronization is required in order to avoid time jitter which can cause considerable variations in the received signal affecting measurement quality. This method appears fascinating but in fact it is difficult to generate short duration pulses and measurement range is limited due to large transmission power required. The transmitted pulse also compromises on dynamic range since the spectrum of transmitted pulse is not uniform over all frequencies in the range.

The main advantages of time domain measurements include quick measurement times and direct probing of channel characteristics without the involvement of any tedious signal processing of measured data. By using averaging mode of digital oscilloscope, local average power delay profile is readily available. Also, the measurement system is not complex with relatively simple implementation.

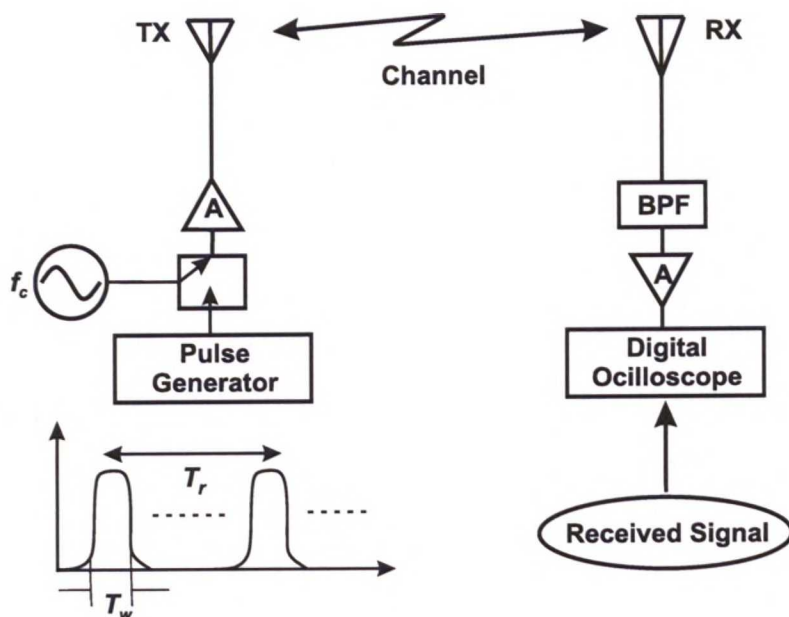


Figure 2.12 Time domain channel measurement set-up

2.2.7.2 Frequency domain (FD) channel measurements

The duality principle between time and frequency domain allows to perform channel measurements in frequency domain as well. The channel impulse response is measured in frequency domain and later transformed in time domain using the Fourier transform. Channel measurements in frequency domain can be easily executed by means of a vector network analyzer (VNA). VNA carries out synthesized frequency sweeping with an S-parameter test to observe channel frequency response. The bandwidth B_w with lowest and highest frequencies as f_L and f_H respectively,

centered around the frequency of interest f_c is scanned in the VNA by stepping through discrete frequencies with equal spacing Δf making a total of N_s samples. VNA transmits a continuous wave signal corresponding to each frequency samples and receives complex channel transfer function $H(f) = S_{21}(f)$ with amplitude and phase information given by (2.57) as depicted in Figure 2.13.

$$S_{21}(f) = H(f) = \frac{Y(f)}{X(f)} \quad (2.57)$$

where $Y(f)$ is the output signal and $X(f)$ is the input signal.

The obtained channel transfer function $S_{21}(f)$ is processed to band-limited time domain channel impulse response using inverse-fast-Fourier-transform (IFFT) given as:

$$h(t) = FFT^{-1}[H(f)] \quad (2.58)$$

The number of frequency samples N_s and step spacing Δf affects the time resolution of channel impulse response. The multipath capability can be quantified using two terminologies (i) width of delay bin and (ii) maximum detectable delay. The width of delay bin can also be seen as spatial resolution that refers to the separation Δd between two consecutive MPCs and is given as:

$$\Delta d = c \cdot \tau_r \approx \frac{c}{B_w} \quad (2.59)$$

where τ_r is the the width of delay bin and c is the speed of light. Whereas the maximum detectable delay represents the limit for the last MPC and should be long enough to ensure that all MPCs are received and is related as:

$$\tau_{max} = \frac{1}{\Delta f} \quad (2.60)$$

Calibration is a key element required for the correct assessment a propagation channel. Therefore, in order to reduce the effect of VNA itself, back-to-back calibrations are required for a an accurate estimate of a channel impulse response. VNA specific calibration is short-open-load termination (SOLT) calibration where it establishes the reference planes and measures its own frequency response which is then compensated from channel measurements by VNA itself. The back-to-back calibration does not include antennas and in order to decouple antenna effects additional calibration steps have to be taken. A typical frequency domain measurement set-up is depicted in Figure 2.13 which includes VNA as a data-acquisition device, TX and RX antennas, low noise amplifier (LNA) on the receive side.

Although frequency domain channel measurements are straightforward and accurate, they suffer several disadvantages by taking into account different issues of practical nature and are discussed here. Since frequency domain measurements involve frequency sweeping through all the frequency samples, this increases the measurement times. If channels is time varying, the captured channel transfer function also varies translating into errors in channel impulse response. Hence these measurements demand static environment for accurate results. The measurement

set-up requires cable connection between TX and RX as illustrated in Figure 2.13 and hence measurements are limited to short range. Another noticeable aspect about frequency domain measurements is that it requires considerable post-processing of the measurement data to evaluate time domain results which means additional work as a consequence.

However, on the positive side, frequency domain measurements provide high dynamic range, i.e., high sensitivity and tends to increase signal-to-noise ratio (SNR) due to inherent noise averaging ability of VNA. These kind of measurements also have a uniform dynamic range for each frequency with respect to the system noise.

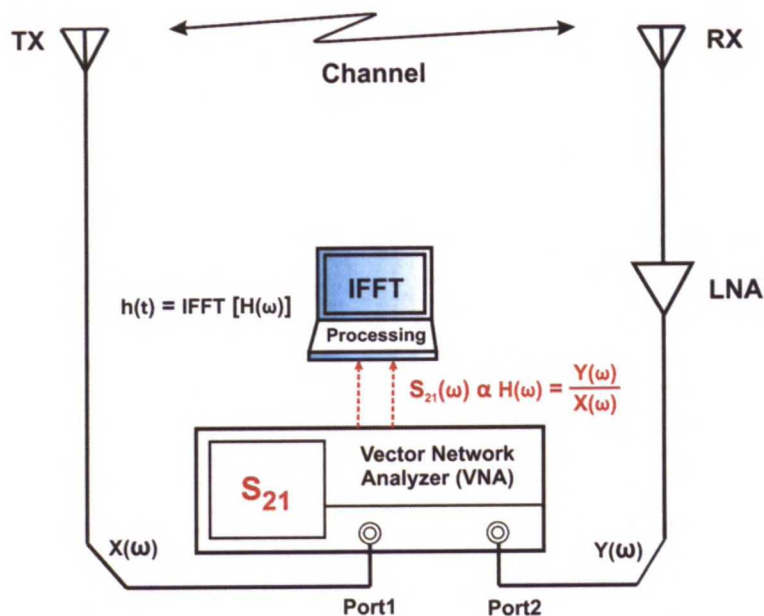


Figure 2.13 Frequency domain channel measurement set-up

2.3 UWB antennas

Various kinds of antennas are used for communication purposes depending upon system and application. They can be distinguished on the basis of geometrical structure, frequency of operation, material used for manufacturing etc. Many different types of broadband antennas are used for UWB radio systems. However, these can be classified into four categories on the basis of their directional characteristics and implementation and are given as:

- **Two dimensional directional antennas:** Vivaldi, Tapered Slot, Log-periodic, Log-spiral, Conical-spiral antennas etc.
- **Two dimensional omni-directional antennas:** Planar dipole, Planar Slot antennas etc.
- **Three dimensional directional antennas:** TEM Horn, Ridge Horn, Reflector Horn antennas etc.
- **Three dimensional omni-directional antennas:** Loaded cylindrical dipole, Bi-conical, Disc-cone, Roll antennas etc.

Based on the requirements of an UWB radio system, a radio engineer decides technically most suitable and practically feasible antenna. Typical planar vivaldi, TEM horn and biconical antennas are depicted in Figure 2.14.

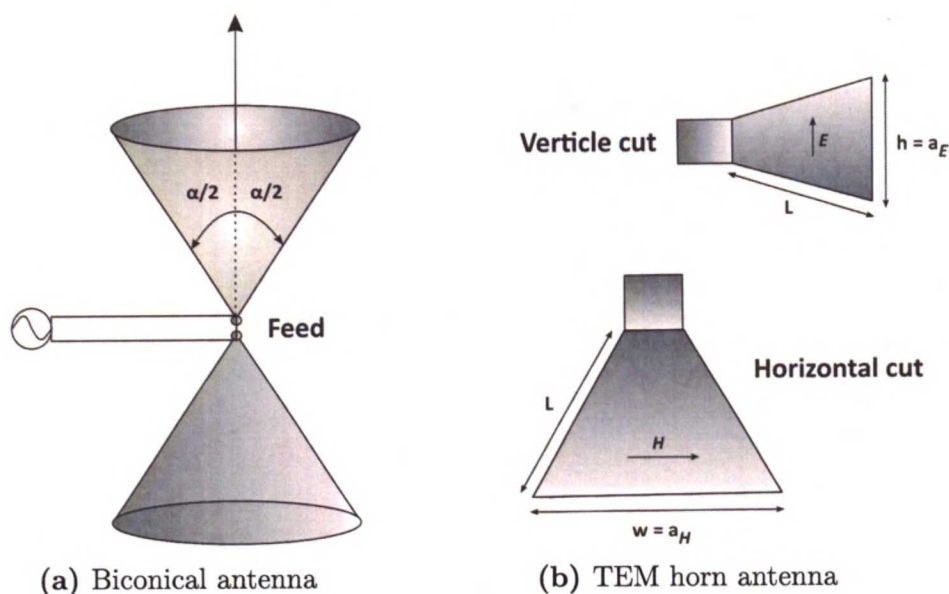


Figure 2.14 Typical examples of UWB antennas

2.3.1 Antenna design considerations

The traditional way to characterize the performance of narrowband and broadband antennas, is based on impedance matching bandwidth, radiation pattern, gain,

beamwidth and polarization characteristics. Since UWB systems may not use carriers, they need to be treated specially. Conceptually, an UWB system must transmit and receive signal with considerable quality in order to achieve sufficiently good signal-noise-ratio (SNR). A distorted received waveform may degrade SNR badly.

UWB antennas can be most properly assessed by system transfer function and radiation transfer function. The TX-RX antenna system is depicted in Figure 2.15. Assuming far-field conditions, the Friis transmission relation describing transmit and receive power relationship is given by (2.61) where frequency dependency of UWB antennas is also considered.

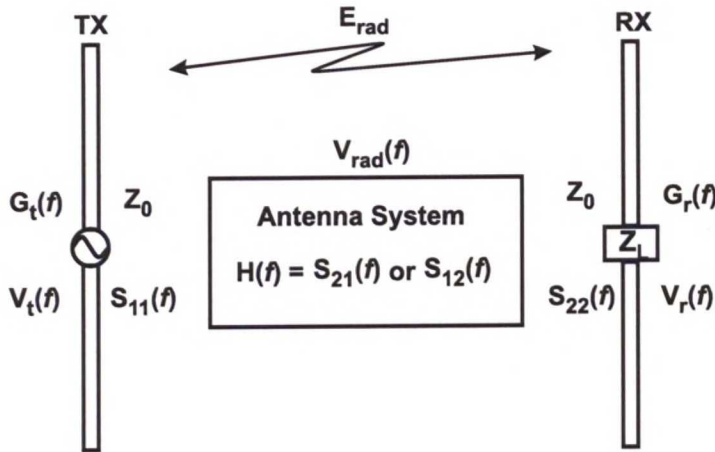


Figure 2.15 TX-RX antenna system

$$\frac{P_r(f)}{P_t(f)} = (1 - |\Gamma_t(f)|^2)(1 - |\Gamma_r(f)|^2) (|\hat{\rho}_t(f) \cdot \hat{\rho}_r(f)|^2) G_t(f) G_r(f) \left(\frac{\lambda}{4\pi r} \right)^2 \quad (2.61)$$

where

P_t, P_r : Transmit and receive power at antenna ports.

Γ_t, Γ_r : Insertion loss of transmit and receive antennas.

$|\hat{\rho}_t(f) \cdot \hat{\rho}_r(f)|^2$: Polarization mismatch between transmit and receive antennas.

G_t, G_r : Gain of transmit and receive antenna.

λ : operating wavelength

r : Separation between transmit and receive antenna.

The gain and polarization factors also depend upon angular orientation but for the sake of simplicity it is not expressed in (2.61). A system transfer function describes the relationship between source and load voltages and is given as:

$$H(f) = \frac{V_r(f)}{V_t(f)} = \left| \sqrt{\frac{P_r(f) Z_{load}}{P_t(f) 4Z_0}} \right| e^{-j\phi(f)} = |H(f)| e^{-j\phi(f)} \quad (2.62)$$

where Z_0 is the characteristic impedance, Z_{load} is the load impedance and $\phi(f) = \phi_t(f) + \phi_r(f) + fr/c$ refers to the phase variations due to transmit and receive antenna. The transfer function hence defines the characteristics of both transmit and receive antenna. Transfer function of antenna systems can be easily determined by the S-parameter test set using a vector network analyser (VNA). The received signal is thus obtained from the magnitude and phase of antenna system transfer function. One of the main objectives in UWB antenna design is to achieve constant magnitude and linear phase response across signal bandwidth, otherwise, distortion may affect the received signal.

Another important parameter to be considered is radiation transfer function \vec{H}_{rad} which describes the relationship between radiated electric field \vec{E}_{rad} and voltage level $V_t(f)$ of the transmitted signal. It is given as:

$$\vec{E}_{rad} = \vec{H}_{rad}(f)V_t(f) \quad (2.63)$$

The radiation transfer function is a vector quantity and is directed along the polarization vector \hat{a} of transmitting antenna. It also depends upon the orientation of antenna and determines the radiation pattern.

2.4 Summary

This chapter has reviewed the basic concepts related to UWB propagation channels and antennas. After the introductory remarks, the frequency regulations for UWB usage have been described. The chapter is then divided into two main sections. The first section begins with wireless channel representation following frequency selectivity of channels and various propagation channel characteristics which include large-scale and small-scale effects and delay domain characteristics. Later, the path arrival delay domain models have been discussed. The second section introduces a brief account of UWB antennas and closes the chapter.

Chapter 3

Shielding theory and literature review for Vehicle Penetration Loss

3.1 Introduction

The Vehicle Penetration Loss (VPL) is the term associated with the attenuation experienced by the radio waves while they penetrate the interior of a vehicle. The ecumenical definition of VPL would be “*The ratio of the power level P_{out} immediately outside the vehicle to the power level P_{in} inside the vehicle*”. Mathematically it is given as:

$$L_{\text{VPL}}[\text{dB}] = 10 \log_{10} \frac{P_{\text{out}}}{P_{\text{in}}} \quad (3.1)$$

In general, the vehicle chassis being a metallic structure can be viewed as a shielding enclosure with various discontinuities such as window apertures and small openings throughout the chassis. In this perspective, an intuitive description of electromagnetic shielding theory in connection with VPL provides a deep insight for understanding propagation of radio waves into a vehicle. Therefore, the first part of this chapter discusses electromagnetic shielding mechanism and related concepts in detail. The succeeding part of the chapter comprehensively reviews the previous literature concerning VPL pointing out missing links for the effective assessment of VPL and the contribution of this thesis to overcome these gaps.

3.2 Electromagnetic shielding

In electromagnetic theory, the term shielding refers to the method of precluding undesired electromagnetic radiation into electronic equipment allowing it to operate in its compatible electromagnetic environment. A shield can be viewed conceptually as a barrier for the propagation of electromagnetic fields and is essentially in the form of a metallic enclosure that either confines emitted radiation within it or rejects radiations from some external source. Typical shielding environments are illustrated

in Figure 3.1 with two possible configurations. Figure 3.1a depicts a shielding enclosure that excludes external radiations while Figure 3.1b shows a shielding enclosure confining radiated emissions within itself.

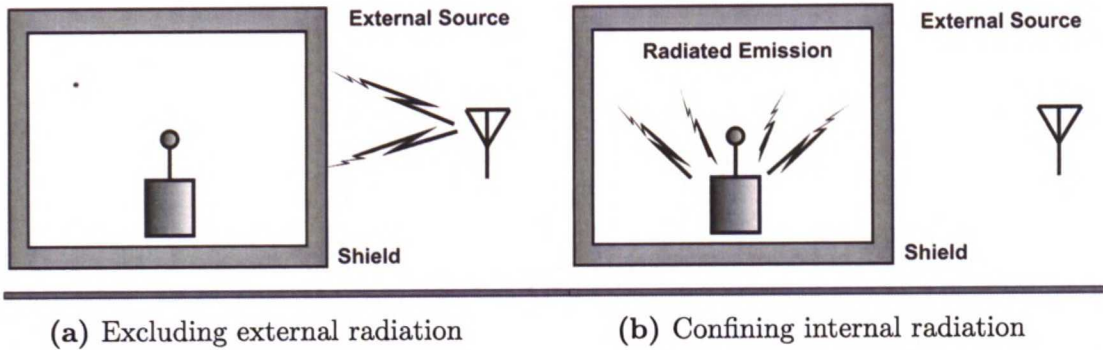


Figure 3.1 Shielding enclosure

Practically it is not possible to achieve perfect shielding due to the presence of discontinuities in the shielding wall such as joints, access windows and ventilation holes. Hence the practical problems include these discontinuities and solution is approximated. Performance of shielding depends on various parameters such as frequency, distance of interfering source from shield walls, polarization of the incident fields, discontinuities etc. The typical way to achieve shielding is the introduction of a metallic obstacle between a transmitting source and equipment to be shielded. When electromagnetic waves while propagating through space interacts with the metallic obstacle, it experiences the characteristic impedance offered by the metal which is mathematically given as:

$$Z_0 = \sqrt{\frac{\omega\mu_0}{2\sigma}}(1 + j) \quad (3.2)$$

The value of characteristic impedance for good conductors is extremely low. The electromagnetic wave impedance is, however, given by a simple relation as follows:

$$Z_w = \frac{E}{H} \quad (3.3)$$

Revisiting (3.2), which is a general description of characteristic impedance of a metal, the explicit absolute expression of shield impedance is, therefore, given as:

$$|Z_s| = \sqrt{\frac{\omega\mu_0}{2\sigma}} \quad (3.4)$$

Reflection and absorption of the incident electromagnetic waves are the two basic mechanisms that govern shielding. Hence, shielding depends on the reflection of electromagnetic waves from metal surface and transmission through it. The electromagnetic waves upon striking metal surface, partly get reflected from the low impedance boundary due to mismatch and rest of it is transmitted to the other side

after partial absorption in the shield. A situation of plane wave incident on the shield boundary is illustrated in Figure 3.2. Multiple internal reflections also exist between the interfaces of the shielding material due to difference of impedance values at the interfaces which produces subsequent secondary reflections and transmissions.

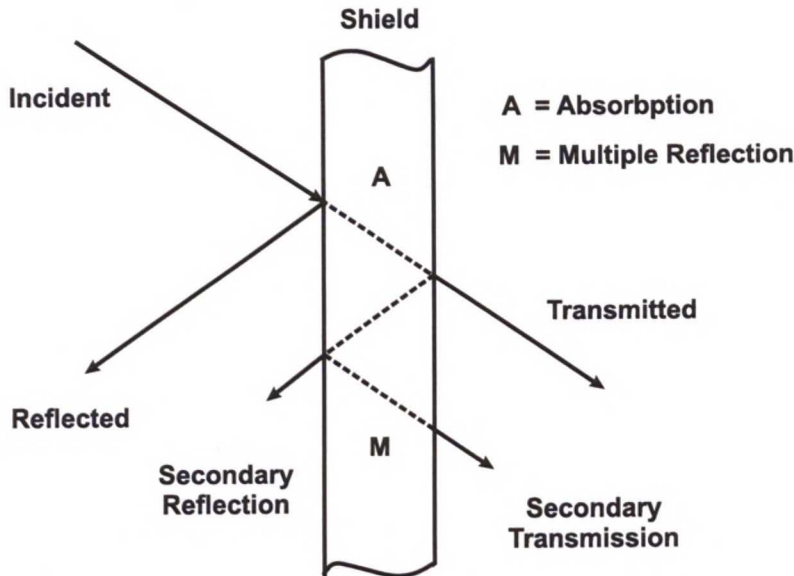


Figure 3.2 Plane wave incident on a shield

3.2.1 Shielding effectiveness

Based on the principle indicated by Figure 3.2, we can define another term that qualifies shielding and is known as shielding effectiveness. The shielding effectiveness is a measure to determine the quality of shielding and is defined as a ratio of incident to transmitted fields given as:

$$SE[\text{dB}] = 20 \log_{10} \left[\frac{E_i \text{ or } H_i}{E_t \text{ or } H_t} \right] \quad (3.5)$$

Hence, shielding effectiveness can be divided into three components namely reflection loss, absorption loss and multiple internal reflection loss and in terms of these integrated components the shielding effectiveness is expressed as:

$$SE[\text{dB}] = R_{\text{dB}} + A_{\text{dB}} + M_{\text{dB}} \quad (3.6)$$

The expression (3.6) with its individual terms can be quantified by considering a single layer shield of thickness t , conductivity σ , relative permeability μ_r and relative permittivity ϵ_r .

Absorption loss: As the electromagnetic wave passes through a conductive medium of the shield its amplitude is attenuated exponentially according to the factor $e^{-\alpha}$ where α is the attenuation constant. The propagation constant inside the shielding material is given as:

$$K = \sqrt{\frac{\omega\mu\sigma}{2}}(1 + j) \quad (3.7)$$

The attenuation constant is, thus:

$$\alpha = \sqrt{\frac{\omega\mu\sigma}{2}} \quad (3.8)$$

This attenuation is referred to as absorption loss. A is related inversely with the skin depth δ of the material given as:

$$\delta = \frac{1}{\alpha} = \sqrt{\frac{2}{\omega\mu\sigma}} \quad (3.9)$$

If the thickness of the obstacle is greater than the skin depth of the obstacle material at the frequency of the incident wave, this wave transmitted from the first interface is attenuated to a great extent before it strikes the next interface. If the shield is designed such that its thickness is much greater than the skin depth of the shield material at the frequency of incident wave, the part of the incident wave is absorbed completely within the shield. Also there is a little magnitude to the continued multiple internal reflections between the interior interfaces of the shield and that can be ignored. The absorption loss is thus given as:

$$A[\text{dB}] = -20 \log_{10}(e^{-\alpha}) = 8.69\alpha = \frac{8.69}{\delta} \quad (3.10)$$

Reflection loss: The reflection loss appears due the difference in impedance value at the interface between two media. In terms of impedance of the incident wave Z_s and the shielding material Z_w , the incident and transmitted electric fields are related to each other by following expression [35].

$$E_t = \frac{4Z_s}{Z_w} E_i \quad (3.11)$$

Therefore, the reflection loss is given as:

$$R[\text{dB}] = \frac{E_i}{E_t} = \frac{Z_w}{4Z_s} = -20 \log_{10} |T| \quad (3.12)$$

where T is the net transmission coefficient through the shielding obstruction. This reflection loss is valid for a plane wave approaching the shield at a normal incidence. If the wave approaches at some other incidence angles, then the reflection loss increases with the angle of incidence since reflectivity increases with the increase in angle. For thick shields, the multiple internal reflection M_{dB} loss can be neglected.

3.2.2 Shielding apertures

In the introductory remarks for this section, it has been introduced that it is difficult to achieve an ideal shielding because of the presence of discontinuities in the shield which are inevitable. The discontinuities come from the practical requirements such as cabling, joints etc. Common type of discontinuities that exists in shielding wall may be in the form of slots in the gaps or ventilation holes, and so forth. The electromagnetic energy leakage in a confined metallic enclosure is dominated not by the physical characteristics of the metal but by the size, shape and location of the discontinuities. The amount of leakage from an aperture depends primarily on following factors:

- (i) Maximum linear dimension of the aperture.
- (ii) The impedance of the incident wave.
- (iii) The frequency of the incident wave.

When the size of these discontinuities becomes equal to their resonant values (where a structure causes oscillating electromagnetic fields), shielding effectiveness at corresponding frequencies would be very low. The apertures in the shielding wall can be modelled as simple geometrical shapes such as rectangular slots and circular holes. Approaching the problem from circuit theory, the incident electromagnetic field on the shield induces currents in the shielding material. These induced currents in consequence generates additional scattered or reflected field which tends to cancel the effects of incident field by having polarity satisfying boundary conditions. For perfect field cancellation to happen, the induced currents need to flow unimpeded. However, if some kind of aperture is experienced by induced currents their normal path is diverted resulting in imperfect field cancellation and reduced shielding effectiveness. Figure 3.3 illustrates the effect of various apertures on the induced shield currents. Figure 3.3a presents a shield without any discontinuity where induced currents flow unimpeded. Figure 3.3b represents a shield with rectangular slot aperture with its linear dimension perpendicular to the flow of induced currents. It is worth to mention that width of the slot does not have significant impact on induced shield currents as depicted in Figure 3.3c. Also if the slot is oriented parallel to the direction of flowing currents, the shielding is affected less illustrated in Figure 3.3d. The circular slot apertures does not cause significant obstruction to the flow of induced currents shown in Figure 3.3e.

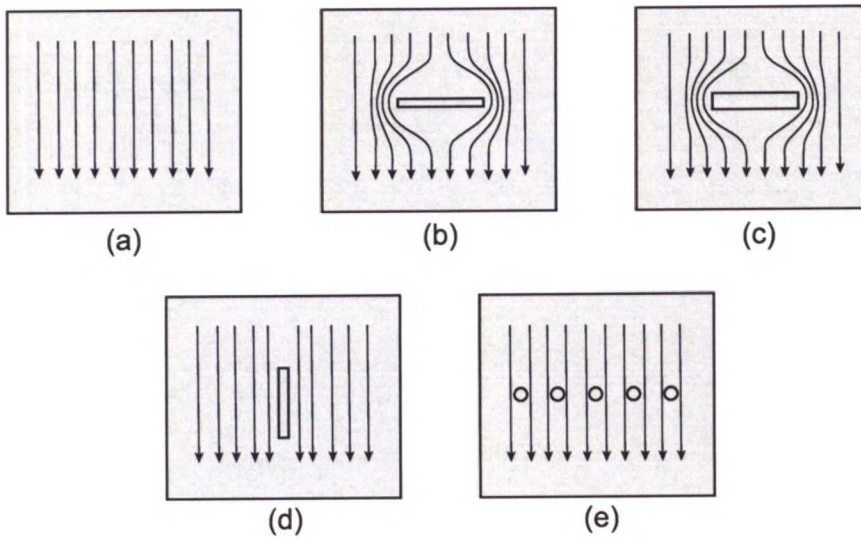


Figure 3.3 Effect of shielding aperture slots on induced currents

From antenna theory, if size of the slot aperture is such that its linear dimension equals half wavelength it act as a radiating slot antenna which is an efficient radiator at half wavelength and its radiation efficiency decreases as aperture become shorter. A slot antenna with its complementary structure, a dipole antenna is depicted in Figure 3.4. The complementary structure as per theoretical articulation have similar radiation characteristics as that of the original antenna.

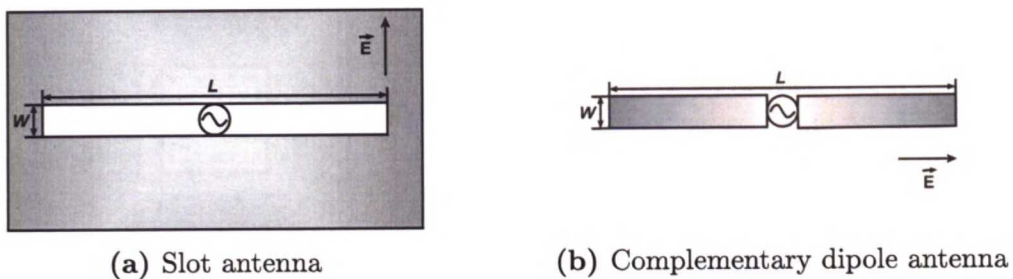


Figure 3.4 Slot antennas

The field transmitted to the other side of the conducting shield wall can be visualized as a dipole field in case of a slot aperture and is shown in Figure 3.5. The shielding effectiveness for a radiating aperture with maximum linear dimension equal to half wave length is given as:

$$SE_a[\text{dB}] = 20 \log_{10} \left(\frac{\lambda}{2l} \right) \quad (3.13)$$

where λ is the wavelength of the incident wave and l is the linear dimension of the radiating aperture.

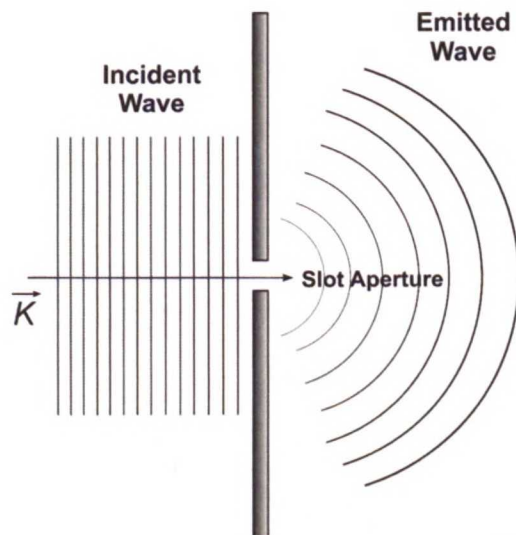


Figure 3.5 Plane wave incident on a shield with a slot aperture

3.3 Previous investigations for VPL

Previous investigations for the evaluation of VPL are presented here in chronological order. In order to maintain consistency, the literature review given in this section contain same abbreviations and terminologies as used in the original literature.

3.3.1 Hill and Kneisel (1991)

The vehicle attenuation characteristics were evaluated for the first time by Hill and Kniesel [1] in the year 1991 while determining portable radio antenna performance at 150, 450, 800 and 900 MHz frequency bands inside a vehicle in outdoor environment.

This investigation aimed at empirical measurements of portable antenna performance at different body positions for various frequency bands in order to support propagation prediction and coverage acceptance. As a part of the objective, the measurements performed were also subject to variation of several factors such as frequency of observation, type of antennas used for measurements, antenna position on the human body and handset carry case type.

The measurement setup comprised of vertically polarized test antennas at the transmit side in the car including Helical, Quarterwave whip, Coaxial dipole and speaker microphone antennas. A regular sedan car was used and mounted on a turntable for horizontal rotation. Spectrum analyser was used in connection with a computer for measurement data display and storage. The turntable rotation was also facilitated by the computer.

For the evaluation of antenna performance, two scenarios were considered which include In-Vehicle measurements dealing with outside to inside vehicle communication and Outdoor measurements for assessing antenna performance inside a specialized anechoic chamber. However, only the first scenario is related to vehicle attenuation and is described here. The In-vehicle measurements were performed at

typical body positions in each frequency band with a variety of male and female human subjects having different heights and weights to realize practical situations. The body positions include head level, left side hip level with swivel case, left side hip level with belt-loop case and shoulder level. The test antennas, as mentioned above, were attached with the human subject at these positions turn by turn for carrying out measurements. The two hip level positions with swivel and belt-loop case correspond to vertical and horizontal antenna orientation at the same level to observe the proximity effects of human body with these antennas. The car on the turntable was rotated through 360° with a step size of 2° for each measurement. The in-vehicle received power level was measured by rotating the vehicle with log-periodic receive antenna outside the car having line-of-sight (LOS) and approximately 55 meters away. A reference measurement was performed with dipole antennas at transmit and receive sides which does not include the car in the setup. The measurements conducted were free space and not environment dependent.

The reported mean vehicle losses are approximately 5 dB, 7 dB and 4 dB at the head level for 150, 450 and 800/900 MHz respectively. Whereas, vehicle loss of about 8 dB, 10 dB and 9 dB are reported for left side body position at 150, 450 and 800/900 MHz respectively. The reported VPL values are summarized in Table 3.1.

The reported vehicle loss values appear to have a strong dependence on in-vehicle antenna orientation. The effect of window films, used for heat rejection purposes, has not been exploited in this investigation. In addition, the measurements are essentially free space and so the scenario is fairly simple and does not reflect the complexity of multipath propagation environments. The measurement equipment qualifies the output results and, is however, not described in detail.

Table 3.1 Mean VPL results from [1]

Type of vehicle	In-vehicle antenna positions	Frequency	Mean VPL [dB]
Four door sedan car	Human head level	150,450, 800/900 MHz	5, 7, 14
	Human belt level		8, 10, 9

3.3.2 Vogel, Torrence and Kleiner (1996)

The measurements for penetration loss into vehicles for a satellite communication link at 1600 MHz (L-band) were performed by Vogel, Torrence and Kleiner [2] in the year 1996.

The measurement equipment included a transmitter using cavity-backed spiral antenna (right hand circularly polarized (RHCP), beamwidth= 90° , gain=7.8 dBi). The data acquisition equipment comprised of a quadrature detector receiver with a sampling rate of 1000 sample/sec for each measurement. The receiver exploited two different antennas in the test vehicles, microstrip patch antenna (RHCP, beamwidth = 125° , gain = 2.6 dBi) and quadrifilar helix antenna (RHCP, beamwidth = 150° el and 360° az, gain = 1.2 dBi) attached to a dummy handset. For measurement

purposes, five vehicles of different size and design were used including a large and small pickup truck, a small and large sedan, and a minivan. These vehicles were settled on a turntable, approximately 10 cm above a pavement. The measurements were taken at every 5° step through a 360° rotation.

For satellite communication links, the propagation paths are mostly vertical. With respect to the elevation angles considered for the measurements, two scenarios were designed, (i) Elevation angle 8° to 73° measurements and (ii) Elevation angle 90° measurements. The measurement setup is different for the two mentioned scenarios.

For the first scenario, elevation angles 8°, 15°, 27°, 46°, 73° were selected for the transmit antenna. Due to the unavailability of low earth orbiting satellite for measurements, a tower mast was used as a transmitting platform to achieve the required elevation angles. This tower mast was mounted on a van and its height was adjusted to approximately 18 m. The data acquisition equipment was also placed inside the van. The van with tower mast was moved to three different distances from the test vehicle to be measured containing receive antenna. The natural holding positions for the handsets in human hands inside the car were considered for receive antenna orientation. The measurements were taken with human subjects sitting on the driver seat, front passenger, and rear passenger seats.

For elevation angle of 90° measurements, the location was exactly the same as that of the first scenario but with a bit modification in the experimental setup. The direction of transmission was reversed such that the earlier receive side now becomes the transmit side with the same test antennas. The transmit antennas in this case were elevated exactly above the test vehicle rooftop by connecting them with a rope 10 m high from the ground level and tied between the tower mast and a pole to avoid the van being too close to the test vehicle. The vehicles were not rotated this time and measurements were performed with a 60 sec interval pointing in four compass directions. For averaging the results, the person holding the antenna was moved with a slow rocking motion during the measurements.

A reference measurement was also performed in both measurement scenarios for calibration purpose in which the test vehicle was removed from the environment. All measurements were done with open windows in free space environment.

It has been reported that signal level inside the test vehicles followed Rayleigh distribution and for most of the part the line-of-sight (LOS) path did not exist as power was coupled through strong multipath components. The vehicle loss reported was 15-20 dB over all elevation angles and do not significantly depend on these angles. The reported VPL values are summarized in Table 3.2. It was also reported that vehicle type doesn't have any effect on the loss according to the measurements.

The measurements are different from previous investigation [1], which was targeted for terrestrial communication links with mostly horizontal propagation paths. Vehicle windows were opened for all measurements and window films have not been used.

Table 3.2 Mean VPL results from [2]

Type of vehicle	In-vehicle antenna positions	Frequency	Mean VPL [dB]
Sedan, pickup truck, mini-van	Front and rear passenger seats	1600 MHz	15-20

3.3.3 Kostanic, Hall and McCarthy (1998)

VPL characteristics in 800 MHz frequency band were investigated by Kostanic, Hall and McCarthy [3], in the year 1998.

The defined objective of this investigation was to obtain realistic VPL values in order to determine benchmark parameters which can be used in the design of wireless communication systems for in-vehicle communication.

The experimental setup comprised of a transmit sleeve dipole antenna raised considerably above the vehicle rooftop in order to minimize the near field reflections of signals having low angles of incidence and for this purpose, a plastic mast of height 45 cm was used. The receive sleeve dipole antenna was located in two positions inside the test vehicle including drivers hat and front passenger seat. The measurements were carried out with these antenna positions on successive drives over the same route. Both the antennas were attached to the test receiver with RG-58 cables of the same length for equalizing the cable losses. For data acquisition, linear power averaging was employed at a rate of 400 samples per second over the spatial intervals of 9.15 m. All the measurements were performed in both urban and suburban propagation environments for three different kinds of vehicles including mini-van, full sized car, and sports car.

The average penetration loss reported for the mini-van is 8.2-9.6 dB. For the full sized car, the reported average penetration loss is 7.3-9.0 dB while for the sports car it was reported between 9.3 to 14.4 dB. The reported VPL values are summarized in Table 3.3. The obtained values of penetration loss follow log-normally distribution. It was also reported that the mean values of the penetration loss does not depend on the type of vehicle used and the position of the receive antenna inside it.

Although the study covers different types of vehicles and propagation environments, the environments have not been described properly. The status of car windows whether opened or closed has also not been reported. Window films were not exercised to analyse their effect on penetration loss.

Table 3.3 Mean VPL results from [3]

Type of vehicle	In-vehicle antenna positions	Frequency	Mean VPL [dB]
Sedan car	Drivers hat, hand, pocket	800 MHz	7.3-9
Sports car			9.3-14.4
Mini-van			8.2-9.6

3.3.4 Harrysson (2003)

Fredrik Harrysson attempted to model directional path loss in the year 2003 [4], based on measurements and ray tracing simulations at 1.9 GHz frequency.

Measurements were performed by using half wave dipole antennas as transmitter and receptor inside and outside a regular sized sedan car respectively. Two measurement configurations were adapted which include (i) azimuth plane radiation measurement (ii) elevation plane radiation measurements. For the azimuth plane measurements, the dipole terminal outside the car was raised to 2.5 m height and moved in a semicircular path around the car at a constant radius of 14 m. For the elevation plane measurements, the outside terminal was raised to a height of 8 m above the ground and the car was moved in the same longitudinal direction. The height of the inside terminal was considered to be 80 cm and 35 cm above car bottom to exploit two positions, the head level and pocket level.

For simulations, the car was modelled with two different geometries (i) 6 PEC pannels: open box with roof (ii) 16 PEC panels: model resembling a real car structure. The panels here refer to the thin PEC plates for modelling car geometry. The reason for considering two geometries was to explore the level of accuracy achieved with the complexity of simulation models. The car was assumed to be a box like structure made of PEC with window openings. The ray tracing simulations were limited to double bounce case where a ray can interact only twice with any object in the environment.

The comparison between measurements and simulations has been carried out with polar and rectangular plots of antenna patterns on the angular domain. Based on both measurements and simulations, the effect of car structure on the pathloss has been discussed in a realistic fashion by stating that windows contribute more to the wave propagation from front and rear of the vehicle as compared to the side windows. Hence the attenuation level is different for all 4 sides of the car. The attenuation level of 5 dB at 50 degrees elevation has been reported. The VPL results are summarized in the Table 3.4. The path loss model has been formulated in the study by Fresnel edge diffraction mechanism and is given as:

$$u(\theta, \phi) = \frac{1}{\pi} \sum_{n=1}^4 (-1)^{b_n} \arctan a \sqrt{s'_n(\phi)(\theta - \theta'_n(\phi))} \quad (3.14)$$

where $u(\theta, \phi)$ is the unit path loss as a function of angle due the knife edge, perpendicular to the direction of propagation at the distance s' and at the angle θ'_n . The weights b_n represents attenuations for different directions. The model is assumed for rough prediction performance.

The study, however, has been presented with an improper description. Details about car structure and type, measurement environment, simulation tool etc. have not been reported. Also, measurements were performed without considering any window coating. The measuring equipment has also not been discussed at all.

Table 3.4 Mean VPL results from [4]

Type of vehicle	In-vehicle antenna positions	Frequency	Mean VPL [dB]
common car	Driver ear and pocket	1.9 GHz	5

3.3.5 Berens, et al. (2007)

In order to develop a framework for the regulation of the deployment of UWB devices in cars, European regulatory domain the CEPT ECC working group TG3 conducted UWB car attenuation measurements at joint European Research Center, (JRC) in Ispra, Italy in the year 2007 [5]. The working group TG3 is a collaboration of car manufacturers, equipment manufacturers and semiconductor companies.

The defined goal of the measurement campaign was to evaluate the car attenuation for the total radiated power (TRP) over full UWB spectrum and intended to be used for assessment of interference aggregation for fixed wireless and similar services.

The measurement setup was comprised of a large anechoic chamber in European Microwave Research laboratory (EMSL) located at Joint European Research Center, Ispra, Italy equipped with an adjustable turntable in the center to facilitate the rotation of the car on it along with a circular peripheral arm for mounting antennas. Network analyser HP8510 was used for data acquisition. A 32 dB broadband amplifier was used to compensate for cable attenuation and ensure sufficient transmission power for the measurement range. A balun was utilized on the transmit side at the output of the amplifier to transform the single ended signal into a differential signal which is employed by the reference antenna. The receiving side used two antennas for exploiting both horizontal and vertical polarizations in a single measurement step. For measurements, two different cars were used including BMW-E66 long version with and without window metallization and Mecedez Benz (MB) C-class T-model estate car without window metallization. Network analyser was configured with a frequency sweep of 0.85 GHz to 11 GHz with 401 frequency points having frequency step size of about 25 MHz.

The measurements were performed by processing the complete sphere space around a car object on the turntable. The measurement sphere around the car was sampled by rotating the car on turntable from ($0^\circ \leq \phi \leq 172.5^\circ$) with a step

size of 7.5° and yielding 24 measurement locations on the azimuth plane ϕ . In a similar fashion, the receiver antennas were moved on the concentric peripheral arm around the car from $(-97.5^\circ \leq \theta \leq 97.5^\circ)$ with a step size of 7.5° contributing a total of 26 measurement locations in the elevation plane θ . Hence the total spatial steps in both planes were $24 \times 26 = 624$. The measurement distance was kept fixed at 10 m between transmit antenna inside car object and receiver antennas on the peripheral arm around the car. Total nine different transmit antenna positions were considered for measurements inside the car object. These positions include (i) steering wheel (ii) central console/ radio shaft (iii) glove box (iv) A-pillar (v) ceiling (vi) storage font at the rear (vii) engine compartment (viii) rear-view mirror inside (ix) instrumental panel near front window. Two antenna positions, that are, (vi) and (ix) were aimed for outside to inside communication scenarios and antenna in these positions was directed outward providing average lowest attenuation of all measurements. The rest of the positions were tapped to consider in-car communication scenarios. A reference measurement was also performed over the complete frequency range under free space conditions in order to obtain corresponding attenuations.

The reported results include antenna radiation pattern of the reference antenna and TRP attenuation values. The typical attenuation values reported for 3-9 GHz band with BMW without metallization are in the range of 9-14 dB, BMW with metallization are in the range of 12-19 dB and for Mercedes Benz (MB) without metallization the attenuation values are in the range 7-9 dB. The reported VPL results are summarized in the Table 3.5.

Although measurements were performed in a specialized environment with qualified equipment, the setup still suffered from relatively low dynamic range and certain measurement points remain below the noise floor -95dBm/MHz . One another important aspect which has not been considered in this study is to evaluate the effect of human presence inside a car object. Also the scope of investigation does not include propagation analysis to explore the propagation phenomenon associated with attenuation due to penetration of radio waves into the car.

Table 3.5 Mean VPL results from [5]

Type of vehicle	In-vehicle antenna positions	Frequency	Mean VPL [dB]
BMW non-metalized	Steering wheel, central console, pillars, rear view mirror, engine compartment, instrumental panel near front window	3-6 GHz	13-16
		6-9 GHz	12-19
BMW metalized		3-6 GHz	14-19
		6-9 GHz	
Mercedes Benz non-metalized		3-6 GHz	7-8
		6-9 GHz	7-9

3.3.6 Tanghe, Joseph, Verloock, Martens(2008)

VPL at 600, 900, 1800 and 2400 MHz was evaluated by Tanghe, Joseph, Verloock and Martens comprehensively in the year 2008 [6].

The experimental setup comprised of a mini-van with two omni-directional antennas RX_{in} and RX_{out} . The RX_{in} was installed inside the vehicle at a height of 0.6 m between driver and front passenger seats in vertical and horizontal orientations for measurements. Whereas, RX_{out} was mounted vertically outside the mini-van and was raised to 1.25 m above the metallic rooftop of mini-van to avoid reflections. On the other hand, the TX antenna similar to the RX antennas was mounted vertically on a mast which was 3 m high from the ground level. Both TX and RX antennas were vertically polarized dipoles. A signal generator was used as a source at TX side introducing 24 dBm input power to the antenna ports.

Measurements were performed along several streets in a suburban environment of Ghent, Belgium. The mini-van was driven in line-of-sight (LOS) with TX antenna having initial separation of transmit and receive sides of 3m and ending at a separation of 75 m. The receiving antennas were connected to spectrum analyser with identical cables for data acquisition. Power levels were sampled at a rate of 14 samples/sec for both receiving antennas. The mini-van was driven at a constant speed of about 1-2 km/h monitored through GPS device. The measurements were performed with front and rear vehicle illumination and various orientations of receive antenna inside the vehicle. The vehicle was only illuminated from the front and rear sides because of the view that in a suburban environment the lateral sides are usually illuminated by the secondary reflections off nearby buildings.

VPL was also simulated by using a 3D ray tracing software package named as Wireless Insite. Mini-van was modelled as a box like structure as perfect electric conductor (PEC). Plastic for car interior and glass windows were also incorporated in the model. The simulations were performed mimicking measurement setup and simulated receive power inside and outside the vehicle was averaged over ten wavelengths in order to calculate VPL samples.

The fading characteristics of the receive signals for both measured and simulated results are reported for outdoor and in-car RX at 600 MHz radio frequency. A reasonable agreement between the outside and inside power levels can be observed for both measurement and simulations. On average, the power level degrades for both cases approximately at the same rate. The received in-vehicle signal level seems to be lower than outside for majority of the samples. However, small numbers of in-vehicle power samples are larger which is concluded to be so because of the significant fading of the outside power level as compared to the in-vehicle power. The reason presented for the observed deviation between simulation and measurements is that the environment and mini-van structure complexity couldn't be modelled appropriately in the simulation tool.

It has also been reported that the mean power in the LOS path is on average 10 dB lower than the reflected paths. Based on this argument, it was reported that the LOS path is not the dominant path and ground and building contribute significantly to the power at the receiver. The mean VPL has been reported for

both measurements and simulations with each illumination and in-vehicle receive antenna orientations. In case of measurements, for rear TX illumination and vertical orientation of receive antenna, the mean VPL values are 16.80, 7.54, 9.48, and 13.8 dB and for 600, 900, 1800, and 2400 MHz, respectively. For the same illumination and horizontal orientation of the receive antenna, the mean VPL values are 23.75, 16.03, 11.99, and 19.86 dB for 600, 900, 1800, and 2400 MHz, respectively. Similarly for the front TX illumination and vertical orientation the of receive antenna the mean VPL values are 4.89, 3.20, 3.81, and 5.25 dB for 600, 900, 1800, and 2400 MHz, respectively. For same illumination and horizontal orientation of receive antenna the mean VPL values are 13.26, 17.56, 9.47, and 15.88 dB for 600, 900, 1800, and 2400 MHz, respectively.

In case of simulations, for the rear TX illumination and vertical orientation of receive antenna the mean VPL values are 15.44, 8.17, 8.63, and 12.44 dB and for 600, 900, 1800, and 2400 MHz, respectively. For the same illumination and horizontal orientation of receive antenna the mean VPL values are 22.54, 23.14, 11.57, and 25.30 dB for 600, 900, 1800, and 2400 MHz, respectively. Similarly for the front TX illumination and vertical orientation of receive antenna, the mean VPL values are 3.16, 4.35, 3.65, and 5.51 dB for 600, 900, 1800, and 2400 MHz, respectively. For the same illumination and horizontal orientation of receive antenna, the mean VPL values are 12.89, 18.45, 9.11, and 12.94 dB for 600, 900, 1800, and 2400 MHz respectively. The results are summarized in Table 3.6.

In most cases a good agreement between the measurements and simulations is observed and values deviate on average by only 1.5 dB. It has been reported that the human subjects and objects within and outside the mini-van possibly cause these deviations. Also the mean VPL values seem to be higher consistently for the horizontal orientation of the in-vehicle receive antenna in comparison with the vertical position. With respect to the illumination type, the mean VPL is lower for the front illumination as compared to the rear illumination.

The statistical properties of the VPL have been reported by introducing CDF of measured and simulated VPL with respect to the type of illumination. A good agreement have been observed between measured and simulated CDFs describing approximately the same dynamic range of the VPL samples.

The results have been analysed in a generic and logical way. Experimental setup and vehicle description is adequate and covered comprehensively with all the major details. It has not been mentioned whether measurements were performed with open or close windows. Window films have not been exercised in the measurements. Only front and rear illumination is considered by assuming secondary reflection sources for the lateral sides of the mini-van.

Table 3.6 Mean VPL results from [6]

Type of vehicle	In-vehicle antenna positions	Frequency	Mean VPL [dB]
Mini-van	Between driver and front passenger seat	600, 900, 800, 2400 MHz	22.54, 23.14, 11.57, and 25.3 respectively (vehicle front illumination)
			12.89, 18.45, 9.11, and 12.94 respectively (vehicle rear illumination)

3.3.7 Harrysson, et al. (2011)

Fredrik Harrysson, Tommy Hult and Fredrik Tufvesson determined VPL while evaluating an outdoor-to-in-car MIMO radio channel with antenna handset and user phantom in the year 2011 [7].

The experimental setup comprised two different Rx antenna configuration at the mobile side (MS). The first antenna configuration was a uniform cylindrical 64 elements (4×16) dual-polarized square patch antenna array (UCA) which was intended to be used for directional estimation of the channel. The second antenna configuration was a handset mock-up with four antennas placed at the edges and was used with a user phantom (abdomen to head). The antenna position considered was to mimic the user operation mode i.e. browse mode which represents the scenario where the user holds the handset to watch the screen and operate it. The car used in the measurements was a regular station wagon (Volvo V70) and the MS was placed in the center of the car. For creating a micro-cell scenario at the Tx base station antenna side (BS), a uniform rectangular 32 elements (4×8) dual-polarized square patch antenna array (URA) was placed on the bulged roof of a building at Lund University campus about 13 meters above the ground. For MS, two different locations were selected. The first location was at about 87 meters distance in an open area in a parking lot where line of sight was obstructed at the BS side by a large tree. The second location was at 37 meters distance between the two parallel bulges of the building. The Medav RUSK Lund channel sounder was used for the measurements in the frequency band of 2570-2630 MHz with signal-to-noise ratio of about 20 dB.

The VPL was evaluated by comparing the empirical cumulative distributions of the received signal. The VPL was averaged over 60 MHz frequency band where the sample space was the TX and RX switcheed channels, four phantom orientations and nine local offset positions. The reported average VPL is between 1.6 and 7.9 dB depending upon the two considered scenarios. The VPL results are summarized in Table 3.7. It has been concluded that the VPL values are dependent on scenario and car orientation with respect to the base station. It has been inferred that the difference of VPL values for the two scenarios is due to the elevation angle of the

impinging waves which is different in case of urban and rural environments. The study, however, does not include the use of automotive window coating.

Table 3.7 Mean VPL results from [7]

Type of vehicle	In-vehicle antenna positions	Frequency	Mean VPL [dB]
Station wagon (Volvo-V70)	Browser mode at rear passenger seat	2570-263 MHz	1.6-7.9

3.4 Contribution of this thesis

The major purpose of the research study under the scope of this thesis was to identify and complement the missing analysis in the previous literature. The three main that are absent in literature discussed in the preceding section and accomplished through this thesis work are briefly listed below.

- This research study has analysed the effect of automotive window coating on VPL by utilizing commercially available automotive window films.
- The study provides an insight to the influence of car structure on the propagation of radio waves into it.
- Comprehensive radio wave propagation analysis has been performed in this study to identify the nature of multipath in a given vehicle environment.
- Numerical analysis based on full wave simulations has been performed which gives a new direction for the related research using numerical techniques.

3.5 Summary

In this chapter, the available literature for VPL has been critically reviewed by first introducing electromagnetic shielding theory which provides an effective background for understanding VPL with respect to the vehicle structure. This is followed by the a brief narrative of the contributions offered by this thesis in order to recompense the missing analysis in previous investigations for VPL.

Chapter 4

Ultra-wideband measurements

4.1 Introduction

Radio propagation channel measurements play a vital role in wireless system design and their optimization. The growing demand of high data rates for modern applications requires diverse knowledge of radio propagation channels. The wide-band measurement systems provide a reliable estimate of radio propagation channels and large sets of channel measurement data acquired are processed to characterize radio propagation channels using parameters that provide a statistical measure of multipath in an environment.

Many channel measurement techniques are in practice by wireless research and development community. However, the utilization of any measurement technique influences the subsequent measurement results and the choice may depend on several factors such as available resources, measurement environment and accuracy of results. The two main prominent and widely used channel measurement techniques, time domain (TD) and frequency domain (FD) techniques have been elaborated in Chapter 2. For the characterization of vehicle penetration loss (VPL) at major wireless communication frequencies, UWB measurements have been carried out under this research study which employ frequency domain (FD) measurement technique with vector network analyser (VNA) as a data acquisition device. The basic goal of measurements is to obtain a description of channel transfer function. The foremost advantage of this measurement technique is that it essentially covers the whole frequency range of interest providing high dynamic range. On the other hand, the key limitation of this method is the requirement of static (time-invariant) environment and cable connections from VNA ports to TX and RX antennas which is not crucial since UWB communications are usually restricted to short range applications.

This chapter comprehensively covers the measurement campaigns performed for subject research. The measurement campaigns can be divided into two main phases; (i) UWB car measurements (ii) UWB window film measurements. The first phase deals with different sets of measurements scenarios that were aimed for the evaluation of VPL in an indoor environment. Whereas, the second phase involved window film measurements for the assessment of film penetration loss using a specialized environment.

4.2 UWB car measurements

4.2.1 Measurement location and environment

The characterization of radio propagation channels relies on the considered propagation environment based on which the measured data is categorized into several popular propagation environments such as outdoor urban, suburban, rural and indoor industrial, office, residential environments. A large rectangular, isolated and enclosed storage facility in Hernesaarenranta, Helsinki was selected for the UWB car measurement campaign since relatively spacious area was required to accommodate the car and measurement equipment for planned measurement scenarios. Moreover, the frequency domain measurement method employed necessitates the use of static or time in-variant environment. The spacious measurement area also enables to capture propagation effects properly and isolated location is desirable for minimum possible interference with radio systems operating within the measurement frequency range. The topographic and satellite view of the measurement location is presented in Figure 4.1.



Figure 4.1 Measurement location maps (a) topographic (b) satellite

The measurement environment is essentially a large open space inside the storage facility with numerous static objects within it but the area around the measurement setup was relatively free and there was enough space for performing measurements. The walls and ceiling of the facility were quite rugged and irregular containing a lot of metallization. Some glass windows on one lateral side of the measurement hall were also present. The measurement environment is depicted in the Figure 4.2. Most of the large obstacles in the environment were different types of parked vehicles. The most prominent vehicle nearby measurement setup was a white caravan truck which can be clearly seen in Figure 4.2a. As mentioned earlier, the measurement area was relatively free from objects and the experimental setup was arranged in order to accommodate all measurement categories of interest under the scope of this thesis. However, the rear portion of the hall was concentrated with large number of object

indicated by Figure 4.2b.



Figure 4.2 Measurement environment: (a) measurement area, (b) rear portion.

Another noticeable structure near measurement setup, as shown in Figure 4.2a, is half metallic wall partition with curved horizontal embossed and engrave line pattern located in front portion of the facility. On the other side of this partition wall, large wooden containers are stacked up.

4.2.2 Measurement environment layout

The portion of the facility where the measurements were conducted was 115.6 m long, 22.3 meters wide and 11.2 meters high. In order to perform UWB car measurements, the car was oriented symmetrically with respect to the lateral sides of the facility with an even spacing of around 9.8 m from the lateral walls. The distance of front wall to the car was approximately 16.72 m. For the sake of convenience in measurements, the reference centre was considered to be the point at which the RF N-connector, as RF cable outlet, was installed on the car rooftop at FM aerial antenna place. The measurement layout with the car in the environment, depicting the measurement arrangements is illustrated in the Figure 4.3.

Although measurement arrangements will be discussed in detail in the subsequent subsections according to the implemented scenario, a brief description with respect to the measurement environment is presented here. The RX antenna was mounted on a tripod stand, represented by a small red circle. The TX antenna, depicted as a small blue triangle, was mounted on a 2D electro-mechanical scanner inside the car. The measurements were carried out by traversing the RX antenna in a circular area of constant radius of 7 m from the reference center shown as a small green circle on the car rooftop. The RX antenna was moved around the car with an angular resolution of 22.5 degrees. This step size approximately corresponds to 10λ at around 1 GHz.

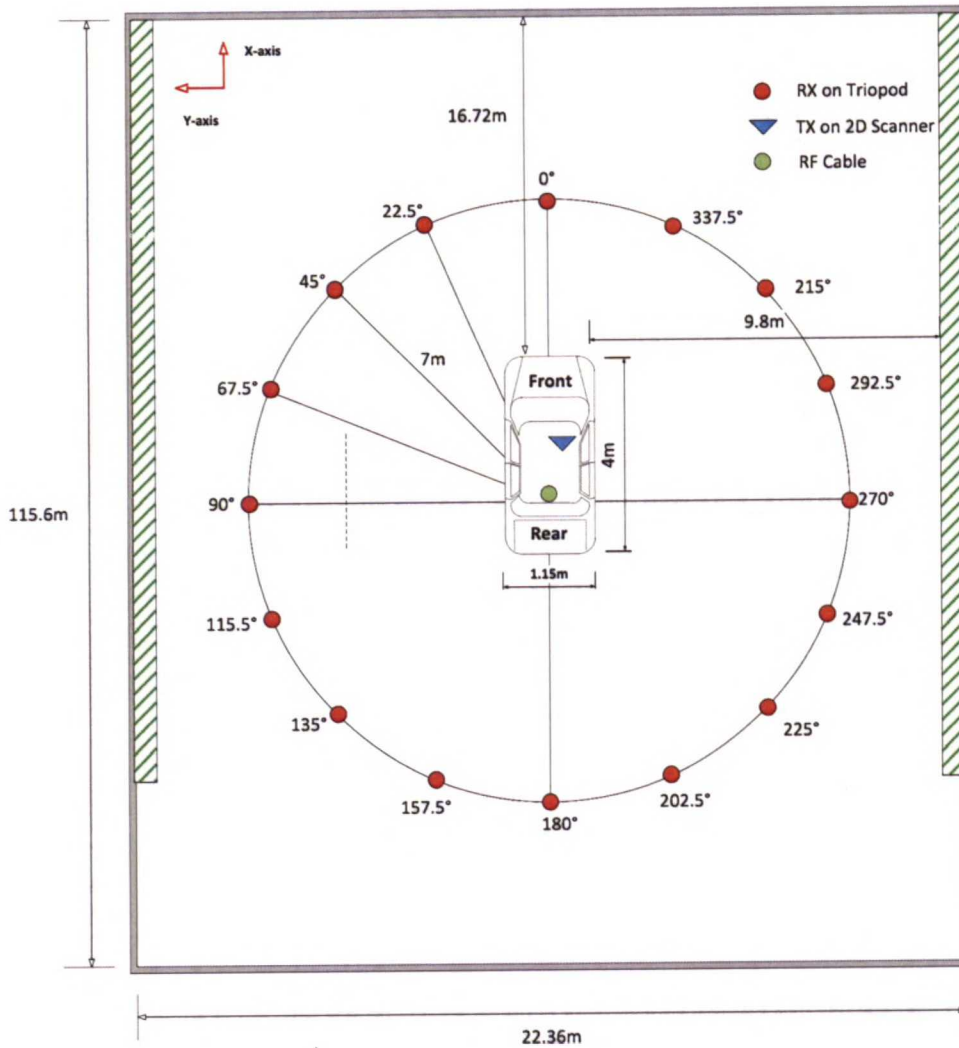


Figure 4.3 Measurement environment layout

4.2.3 Car interior layout

For measurement purposes, the car interior was modified to some extent in order to accommodate the 2D electro-mechanical scanner and facilitate its operation inside the car. The layout with adjustments inside the car is illustrated in Figure 4.4. The front passenger seat of the car was removed and a flat wood board of dimensions (0.5 m × 1.5 m) was firmly screwed in place of the seat for 2D electro-mechanical scanner support. The 2D electro-mechanical scanner was in turn tightly screwed to the wood board making the assembly fixed and provides TX antenna displacements according to predefined settings. Finally, the TX antenna was mounted on the 2D electro-mechanical scanner by using an L-shape fixture. For a set of measurements that were performed with TX and RX antennas inside the car, a 1.5 m long and approximately 0.2 m wide fixture was installed between the neck support of driver and back seat as discussed in detail in measurement scenario Subsection 5.13a . This

fixture contain five fixed measurement points with an even spacing of about 20 cm from each other for mounting RX antenna. Three of the points on this long fixture extends above the back seat while the other two were just above the front driver seat. The TX antenna on the other hand remains on the 2D electro-mechanical scanner for these measurements. All of the measurement equipment except RX antenna on tripod stand resides inside the car including the control and power equipment which was properly adjusted in the trunk providing an ease in accessing and controlling equipment.

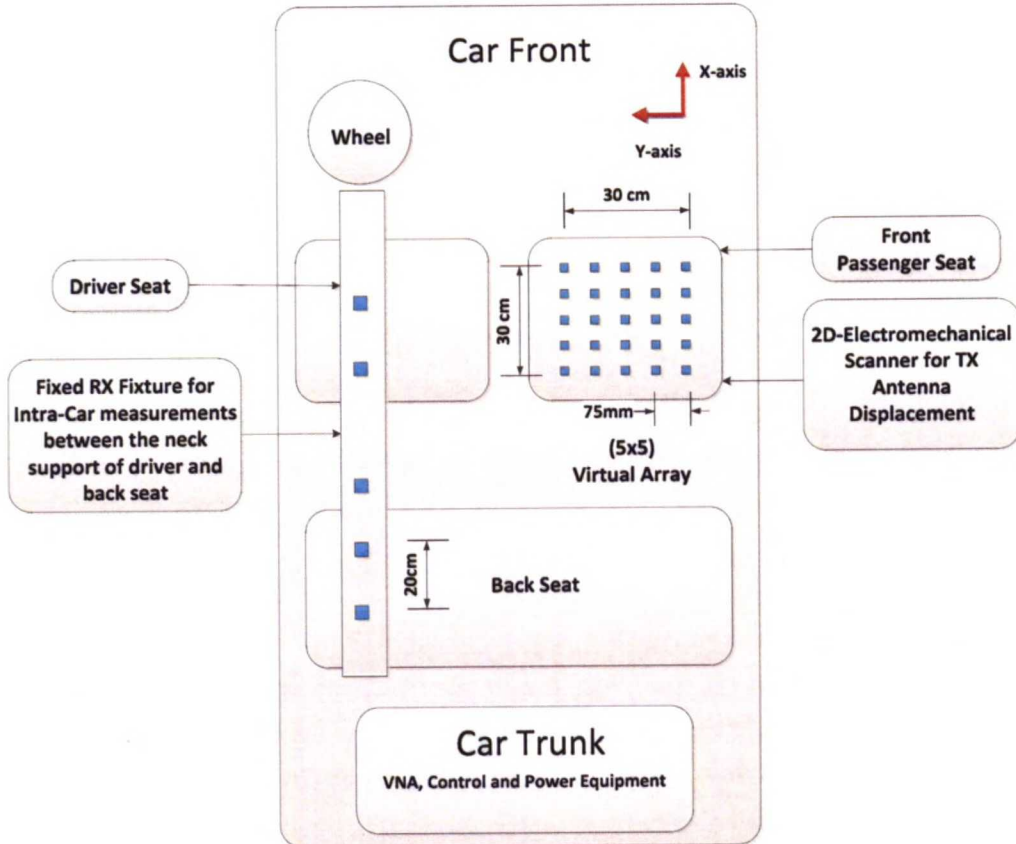


Figure 4.4 Car interior layout for measurements

4.2.4 Measurement equipment

The equipment utilized for any kind of measurement greatly influences the quality of the obtained results. The choice of measurement equipment used for UWB car measurements was based on the measurement technique adopted, being efficient and simple in implementation requirements. The major items include the car, vector network analyser (VNA), TX and RX antennas, RF cables, and the control equipment. The measurement equipment is briefly described below and illustrated in Figure 4.5.

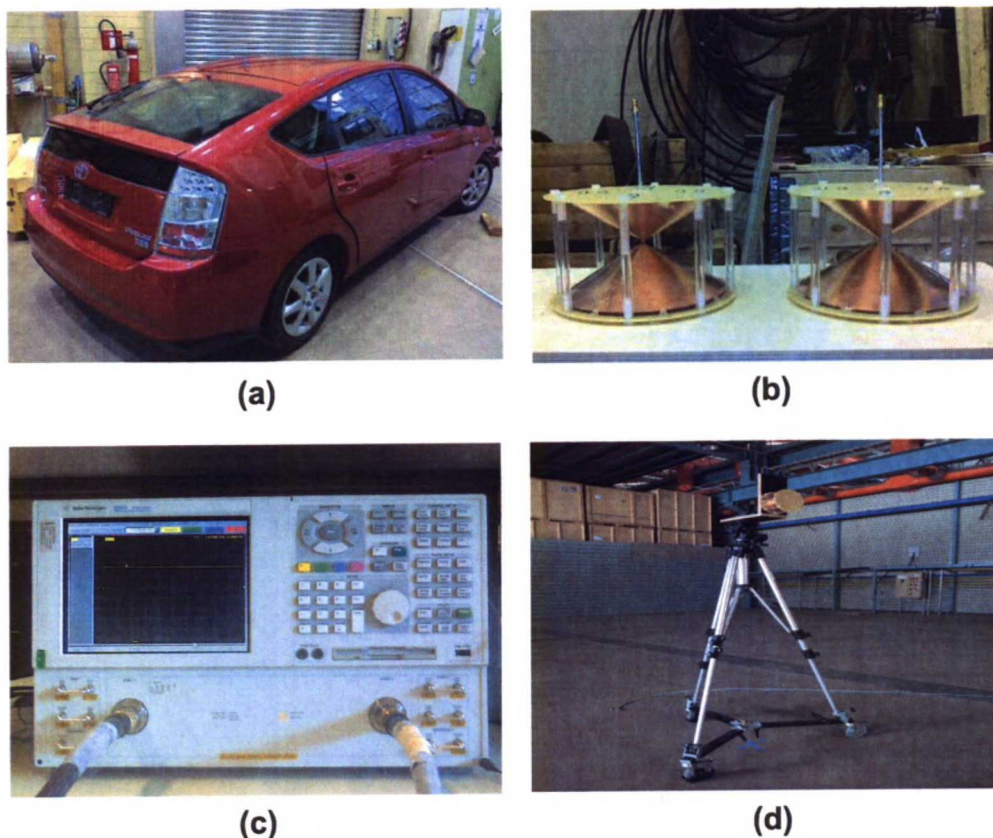


Figure 4.5 UWB car measurement equipment; (a) Toyota Prius car, (b) Bi-conical TX-RX antennas, (c) VNA, (d) Tripod stand with L-shape antenna fixture.

1. **Toyota Prius Car 2008:** In a broader perspective, the car is a part of measurement environment but being a major measurement subject it can be viewed as a measurement equipment. A red colour Toyota Prius car of model 2008 and regular hatchback type, as depicted in Figure 4.5a, is the main measurement subject for which VPL measurements were performed. The skeleton of the car is metallic with the exceptions of glass windows on all four sides, rear and front lights, bumpers and interior assembly including seats, dashboard etc. The side windows are symmetric and similar in shape and size. However, the front and rear windows have large aperture with different vertical orientation as the rear less slanted as compared to the front window. As explained in the previous subsection, the front passenger seat was removed to adjust 2D electro-mechanical scanner. Whereas, the power and control equipment was readily adjusted in the trunk at rear.
2. **TX-RX antennas**

Antennas are the fundamental and one of the most important components of propagation channel measurements since their characteristics affect the output results of measurement systems. As pointed out in Chapter 2, the UWB antennas exhibit frequency selectivity and propagation channel dependency

on antenna increases significantly. It is possible to characterize the UWB channel with different types of antennas. For UWB car measurements in this research study a pair of omni-directional bi-conical antennas were used. Bi-conical antennas are essentially fat dipoles where the lowest order mode is TEM. When bi-conical antennas are fed and start radiating, the current wave travels from antenna terminal towards the outer edge of the cones and gets reflected upon reaching the extreme boundaries. On the way, the wave loses energy and contributes to the radiation loss which increases with frequency. The bi-conical antennas used for subject measurements were designed and built in Aalto University, Department Radio Science and Engineering and are depicted in Figure 4.5b. The measured and simulated return loss for the antennas are shown in Figure 4.6 and indicates that 6 dB bandwidth of the antennas is covering the whole frequency range of interest.

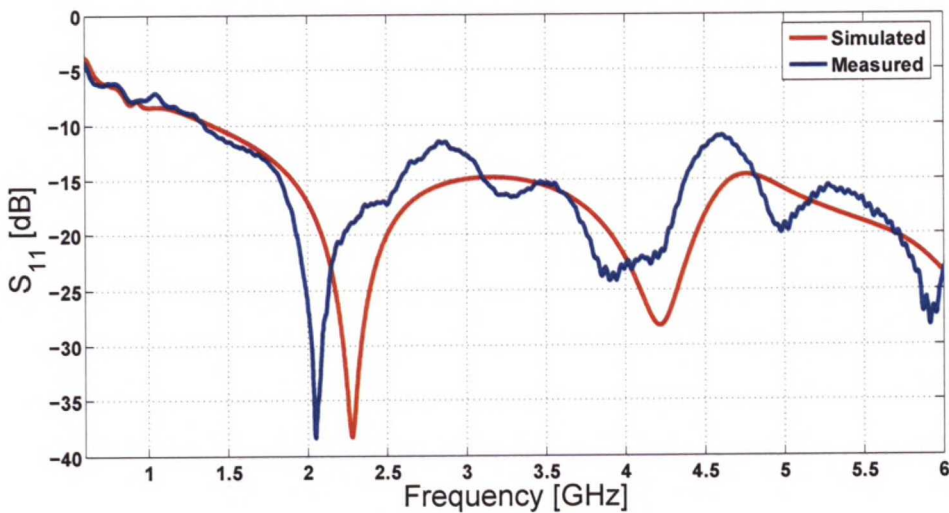


Figure 4.6 Measured and simulated return loss of TX-RX bi-conical antennas

3. **Agilent VNA-E8363A:** The VNA measures the forward transmission coefficient or simply transfer function of the measurement apparatus and the wireless channel under consideration. To obtain the channel transfer function of radio channels, system calibrations are required to remove the effects of other equipment such as cables. The data logged is forward complex scattering parameter $S_{21}(f)$ (amplitude and phase). Agilent VNA-E8363 was used for all measurement campaigns and is illustrated in Figure 4.5c. The supported frequency range is 40 MHz to 40 GHz and the available dynamic range is 138 dB.
4. **Control equipment:** The control equipment consists of a computer loaded with a system design software, LabView. It facilitates VNA measurements by easy parameter configurations in the VNA and linking it with 2D electro-

mechanical scanner operation through programming the movement of the scanner in PC for TX antenna virtual/synthetic array setup.

5. **Cables:** There are three types of cables that facilitated measurements which includes RF cables, GPIB (General purpose interface bus) control cables and power cables. The control computer has connection with both VNA and 2D electro-mechanical scanner through serial and GPIB cables respectively.
6. **RF N-connector:** To serve the purpose of outlet for an RF cable from the car to RX on the tripod, an RF N-connector was installed at place of the car roof FM aerial antenna. It also serves as a reference center for the measurements.
7. **Power equipment:** To maintain constant supply of power to the equipment, ($3 \times 120 \text{ A} \cdot \text{h}$) batteries with power inverter were used since carrying a direct power line into the car requires an inlet which in turn demands drilling a hole in the car and then properly shielding it.
8. **Antenna stand & fixtures:** Two L-shaped fixtures were designed for mounting TX and RX antennas on the tripod stand and 2D electro-mechanical scanner respectively. A third long flat fixture was also used for the Intra-car measurements.
9. **Window coating material** In order to exploit the effect of automotive window coating on VPL and associated propagation phenomenon, two different window coating materials were used; Aluminium metal foil coating and a tinted solar automotive window film PerformX Slate-50.

4.2.5 Measurement system and setup

The measurement configuration adapted was Single Input Multiple Output (SIMO) which exploits diversity enhancement eliminating fading effects and enable directional estimation. This has been implemented using synthetic or virtual array principle which provides channel samples from each array element as TX antenna moves through the 2D electro-mechanical scanner.

There are two significant attributes of a virtual array: excellent user configuration and potentially large array without actual RF implementation. The virtual array concept essentially refers to the modelling of an ideal antenna array constituting arbitrary antenna elements without any mutual coupling positioned at arbitrary coordinates in a given plane. The virtual array grid size was defined as (5×5) , producing a total of 25 array element positions. The scan interval or inter element spacing was set to 75 mm. The scanning speed was adjusted to 10 m/s resulting the single array measurement time duration equals to approximately 4 minutes. Vertical and horizontal polarizations were also considered for the RX antenna in measurements giving co-polar and cross-polar situations with respect to the TX antenna. The TX and RX antennas employed for measurements have been briefly described in the preceding subsection.

The measurements were performed using VNA as a data acquisition device, described in measurement equipment subsection 4.2.4. It measures the channel transfer function of propagation channel under test as scattering parameter $S_{21}(f)$ with amplitude and phase information. For each measurement, VNA swept through the frequency band under consideration, i.e. 0.6 GHz to 6 GHz by stepping into discrete frequency samples $N_s = 2161$. The intermediate frequency (IF) was set to 15 kHz. Low IF bandwidth reduces the effect of random noise on measurements but increases the sweep times. The available bandwidth $B = 5.4$ GHz provides the estimate of maximum detectable delay as:

$$\tau_{max} = \frac{N_s - 1}{B} = 400\text{ns}$$

Whereas the delay resolution is given as:

$$\tau_r = \frac{1}{B} = 0.185\text{ns}$$

The measurement setup is illustrated in Figure 4.7 and is briefly summarized in Table 4.1. The VNA ports are connected to TX and RX antennas through RF cables. The movement of TX is mechanised through the virtual array setup which is explained above and the control connection between PC and scanner is served by GPIB whereas the VNA and control computer has a serial bus connection.

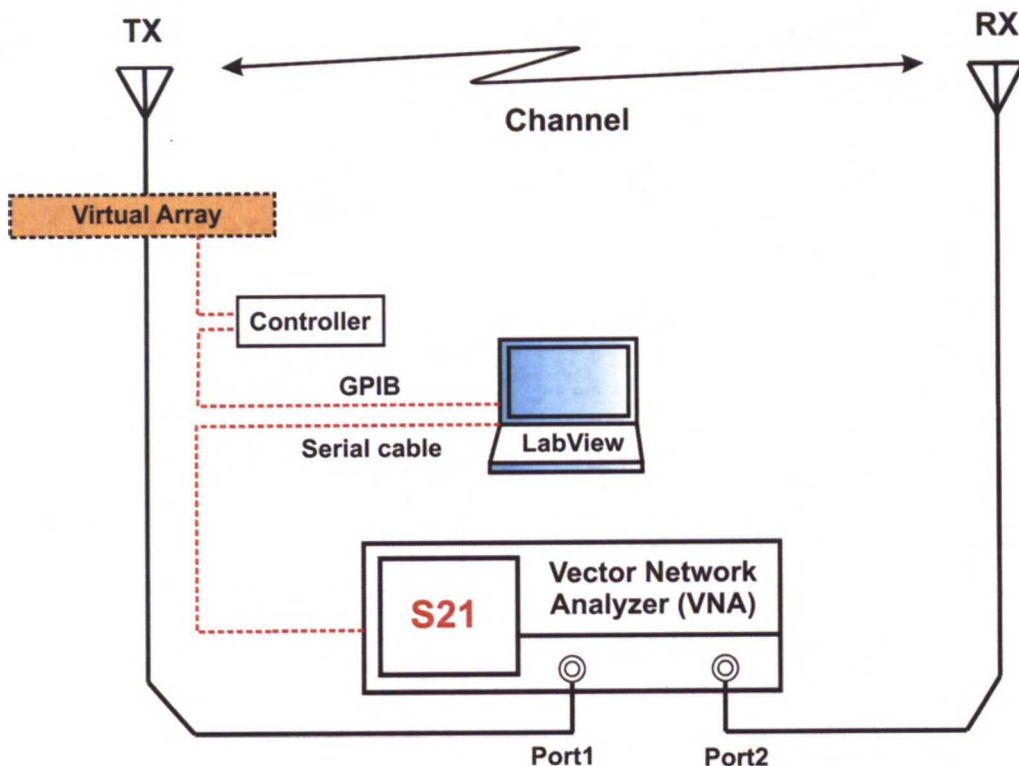


Figure 4.7 Measurement setup for UWB car measurements

Table 4.1 UWB car measurement setup

Setup Name	Description
Antenna array configuration	SIMO/MISO
Frequency band	0.6-6.0 GHz
TX/RX antenna	UWB omnidirectional bi-conical antennas
Antenna polarization	vertical/horizontal
Antennas height	TX = 1.2 m, RX = 2 m
System calibration	Back-to-back cable calibration
VNA settings	<ul style="list-style-type: none"> • IF bandwidth: 15 kHz • Output power: 7 dBm • Number of frequency points: 2161 • Frequency step: 2.5 MHz
2D Electro-mechanical scanner setting	<ul style="list-style-type: none"> • Scan interval: 75 mm • Array grid size: 5×5 • Velocity: 10 m/s
Single array measurement duration	4 minutes approx.
Measurement output	$S_{21}(f)$
Noise floor	-120 dBm

4.2.6 Measurement scenarios

The UWB car measurements have been categorized in four major scenarios. These scenarios along with corresponding detail arrangements are presented here.

4.2.6.1 Inside-outside measurements

As the name indicates itself, in this particular scenario, inside to outside measurements were performed in order to characterize VPL for (i) window coating configurations such as Aluminium foil and solar window film and (ii) Rx antenna positions such as rooftop and around the car positioning.

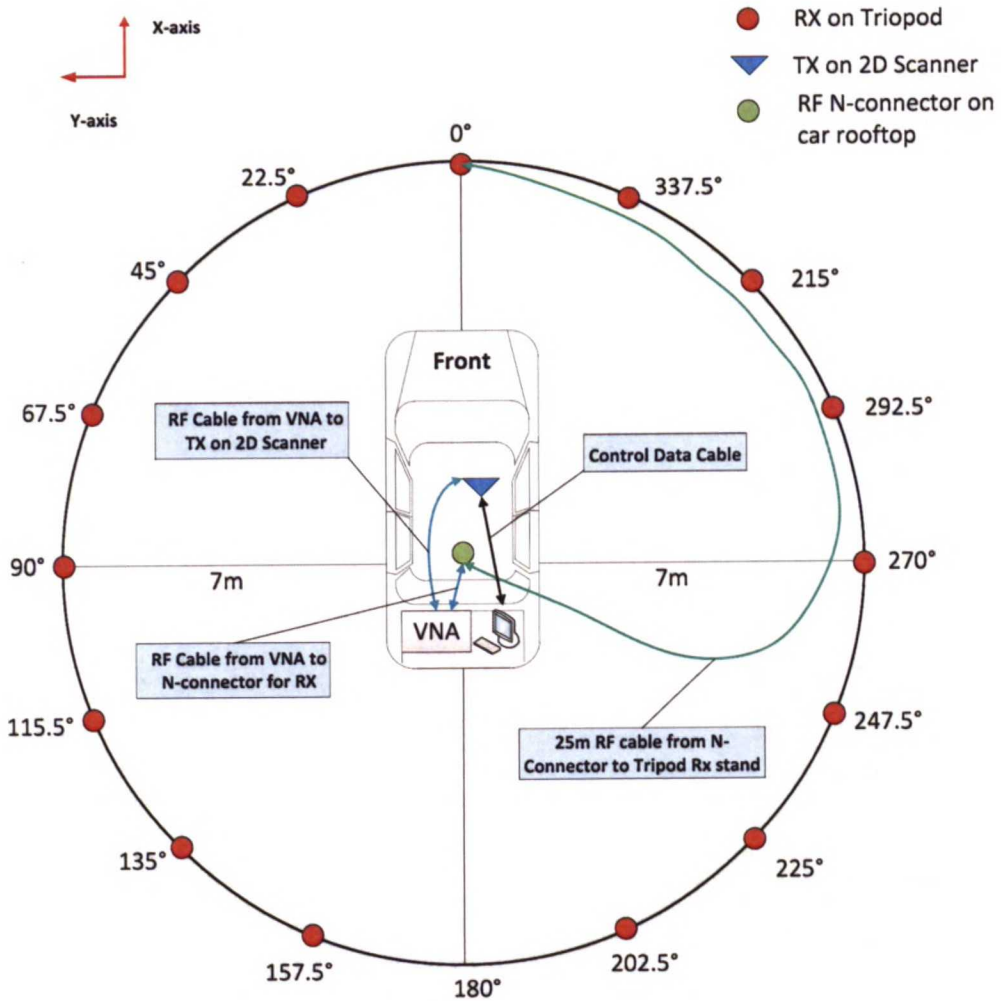


Figure 4.8 Inside-outside measurement scenario

The scenario is illustrated in Figure 4.8 where the legend indicates RX antenna on the tripod stand with a small red circle, TX antenna on the 2D electro-mechanical scanner with a small blue triangle and RF N-connector with a small green circle. The VNA along with the control and power supply equipment was adjusted in the trunk of the car. Port 1 of the VNA was connected to the TX antenna on the 2D electro-mechanical scanner inside the car through a 3 m RF cable while port 2 was connected to the RF N-connector installed at the roof in the place of car FM aerial antenna using a 1.5 m RF cable. This routing was within the car space. The RF N-connector served as the outlet for the connection to RX antenna on the tripod stand outside through a 25 m RF cable. Measurements were taken by traversing the RX antenna around the car in a circular area of almost a constant radius of 7 m and angular step of 22.5 degrees through a 360 degrees rotation for both co-polar and cross polar measurement cases as shown in Figure 4.8. This measurement scenario in the environment is depicted in Figure 4.9a and the TX antenna inside the car on the 2D electro-mechanical scanner is shown in Figure 4.9b.



Figure 4.9 Inside-outside measurements depicting (a) RX around car (b) TX on 2D scanner inside car

In total, twelve measurement sets were performed with different settings in this scenario and are summarized in Table 4.2. As pointed out earlier, two different window coating materials were used for the measurements including Aluminium foil coating and solar window film coating. Three coating configurations were considered for Aluminium foil coating alone; complete covering of windows with car body referred at S.N.3 of Table 4.2, only window covering referred at S.N.4 of Table 4.2 and 10 cm stripped coating along the edges of the windows referred at S.No.5 of Table 4.2. Measurements with human presence inside the car were also conducted in the same measurement scenario which is referred at S.N.9 of Table 4.2. Measurements with variation of RX antenna height of 1.5 m and 2.5 m were also performed to consider the situation with different base station (BS) heights referred at S.N.7 and S.N.8 of Table 4.2 respectively.

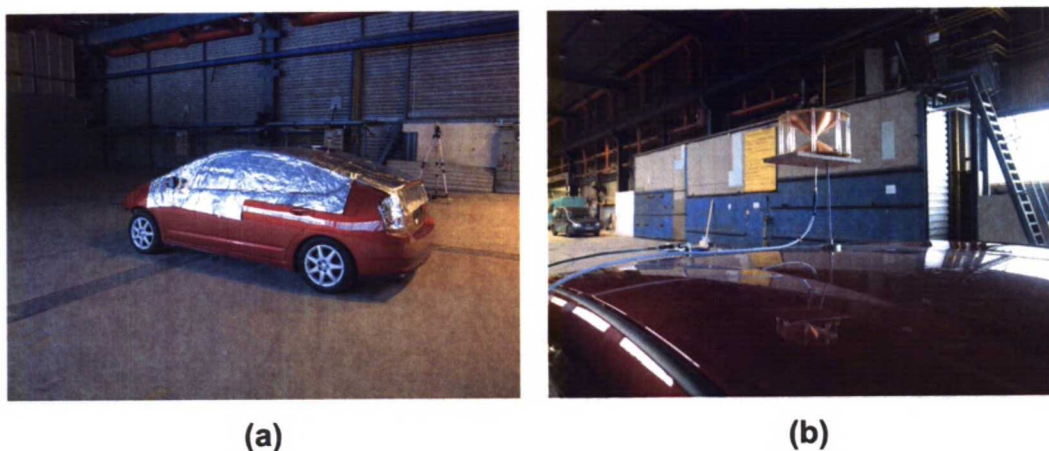


Figure 4.10 Inside-outside (a) window coating measurements (b) car rooftop to inside measurements

Figure 4.10 represents the inside-outside measurement scenario where Figure 4.10a depicts the measurements with Aluminium foil coating and Figure 4.10b shows the RX antenna setting at the rooftop to in-car measurements.

4.2.6.2 Intra-car measurements

The second measurement category is Intra-car measurements. These measurements were carried out to realize the behaviour of signals propagating inside the car if both the transmitting source and receiving antenna are placed inside. The measurement setup is the same as previous measurement scenario but the RX antenna was removed from the tripod stand and was mounted on a fixed flat fixture of dimensions (0.2 m x 1.5 m) installed between the neck supports of driver and the back seat. Five measurement points with an equal spacing of 20 cm extending from the back seat towards the front driver's seat were used for the measurements which illustrate user holding positions for wireless handsets or terminals. Figure 4.11 illustrates the intra-car measurement scenario where virtual array of grid (5×5) is setup on the 2D electro-mechanical scanner on the TX side. In total, two sets of measurements were done in this scenario and are summarized in Table 4.2. The two Intra-car measurements with window film and Aluminium foil coating are referred at S.N.13 and S.N.14 of Table 4.2 respectively.

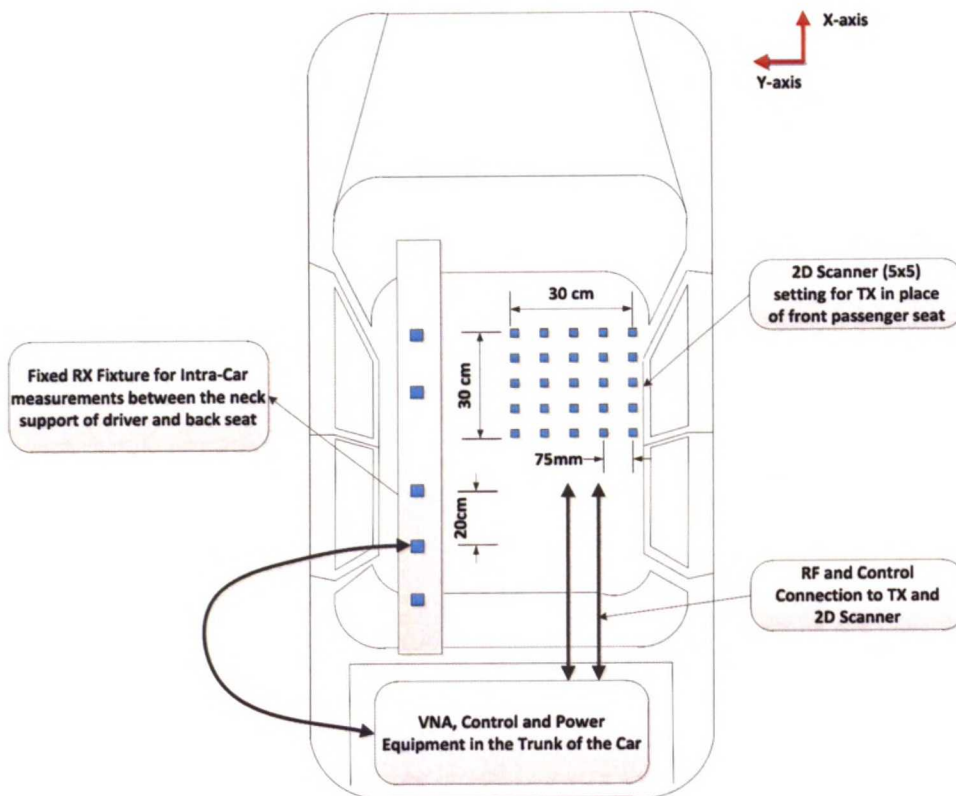


Figure 4.11 Intra-car measurement scenario

Figure 4.12 depicts Intra-car measurements where it points out the location at which the fixture was installed for mounting the RX antenna. The measurements were performed with both Aluminium foil coating and solar window film.

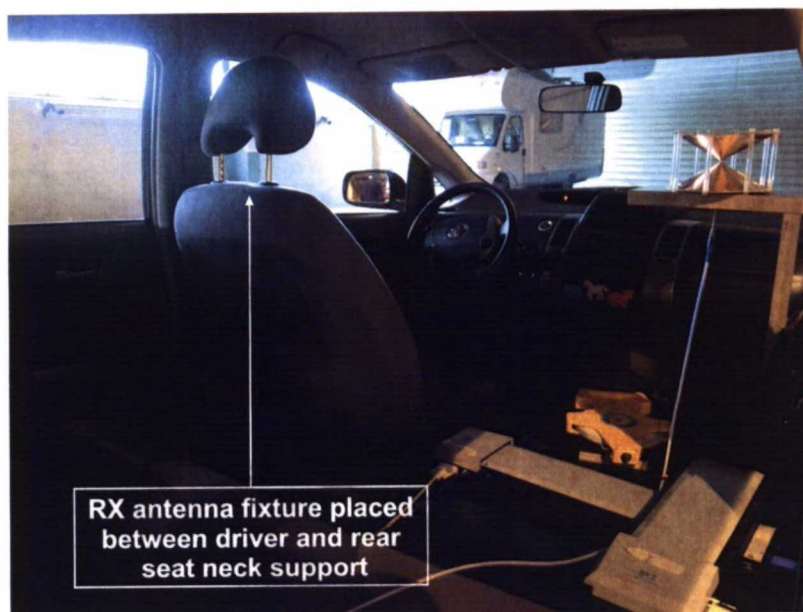


Figure 4.12 Intra-car measurements

4.2.6.3 Outside measurement

The third measurements category considered was Outside measurements which were carried by placing the TX antenna at the centre of the car rooftop mimicking the possibility of a situation when a relay antenna on vehicle roof is used for communication. The measurement setup in this scenario is different from both of the previously measured scenarios since it does not include the 2D electro-mechanical scanner instead the TX antenna was mounted on a 10 cm high fixed fixture and placed at the centre of the car rooftop with the help of a magnetic attachment. In this scenario, the car windows were covered with Aluminium foil. The RX antenna was mounted on the tripod antenna and measurements were performed around the car. The port 1 of the VNA was connected with the TX antenna inside the car using an RF cable which passes through an already existing hole in bottom plate of the car under the rear passenger seat. The port 2 of the VNA was connected with the RX antenna outside on a tripod stand around the car through the RF N-connector installed on the car roof at the place of car FM antenna as explained earlier. The angular step of the RX antenna around the car employed for these measurements was 90° degrees with a total of four measurement points in a complete 360 degree rotation. The Figure 4.13 illustrates the scenario whereas Figure 4.14 presents the pictorial description of outside measurements. The Outside measurement performed is referred at S.N.15 of Table 4.2.

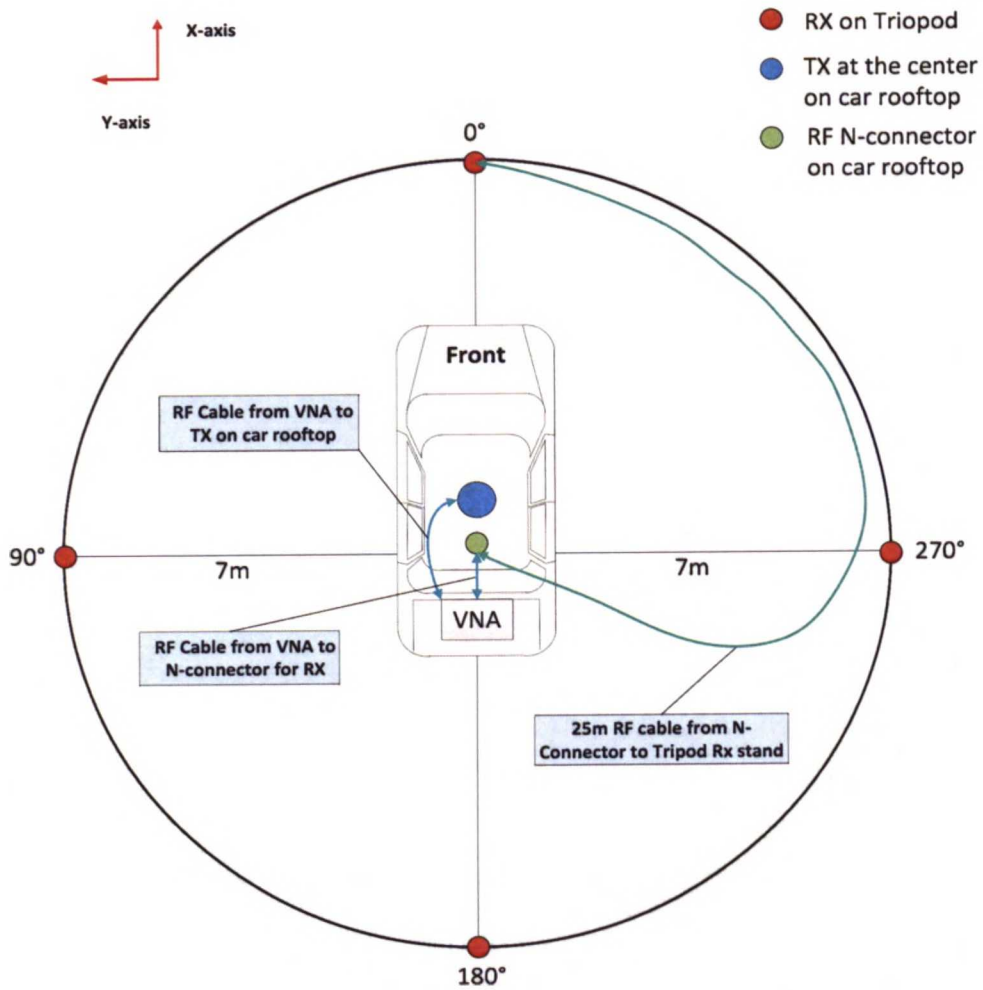


Figure 4.13 Outside measurement scenario



(a)



(b)

Figure 4.14 Outside measurements (a) TX antenna on car rooftop close-up (b) RX antenna around car

4.2.6.4 Reference measurement

The fourth and the last measurement scenario was intended for capturing the measurement environment. It also serves as a reference for all measurements performed with the car. This measurement does not include the car in the environment and instead 2D electro-mechanical scanner along with the measurement equipment was placed at the original position of the car considered for other measurements. The Port 1 of the VNA was connected to TX antenna which was mounted on the 2D electro-mechanical scanner while RX antenna was mounted on the tripod stand at 2 m height similar to scenarios 1 and 3. Measurements were performed by moving RX in a circular area of radius 7 m around the car through a 360 degree rotation with an angular step of 22.5 degrees yielding total sixteen number of measurement points. The measurement is referred at S.N.16 of Table 4.2. The Figure 4.15 illustrates the reference measurement scenario and is also depicted in Figure 4.16 indicating the location of the equipment.

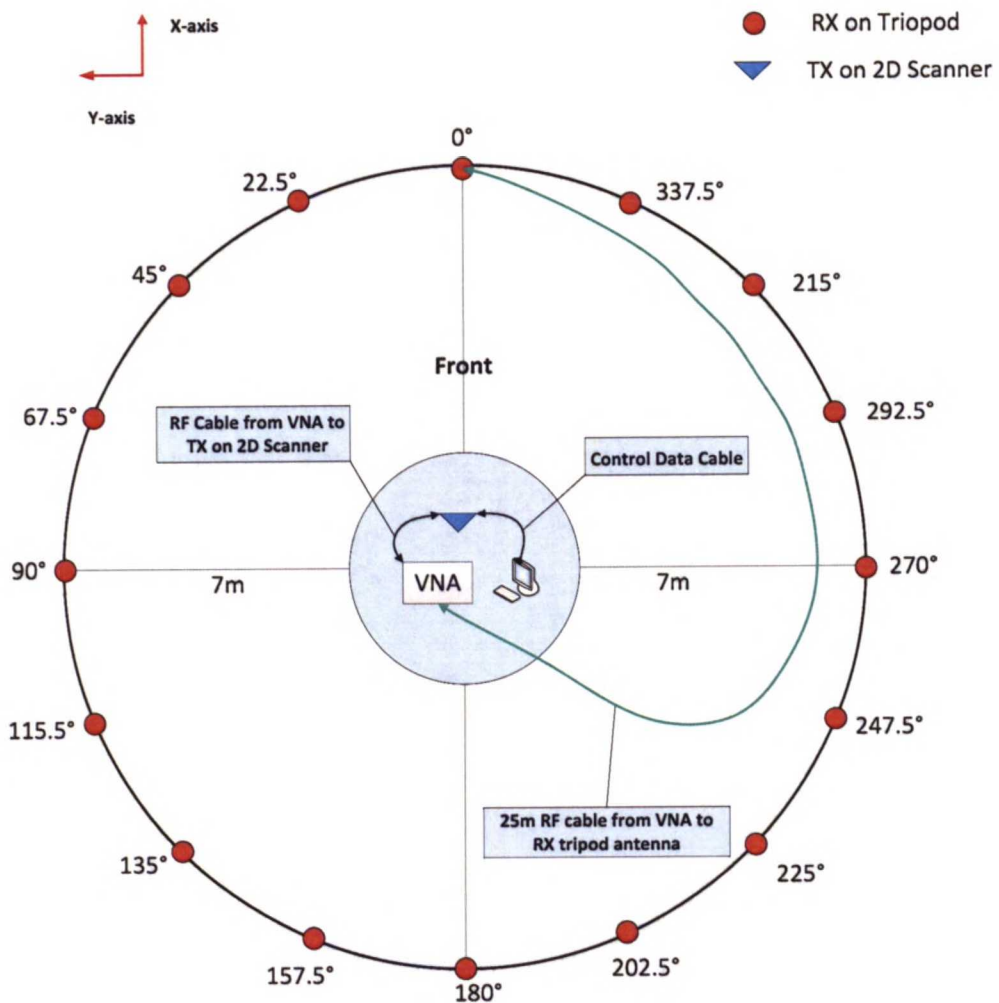


Figure 4.15 Reference measurement scenario

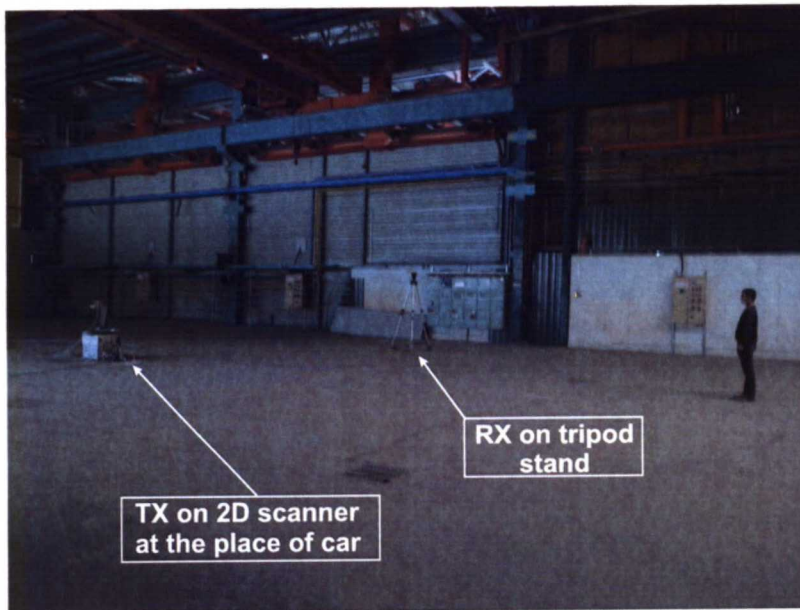


Figure 4.16 Reference measurements

4.2.7 Measurements summary

The measurements performed in UWB car measurement campaign are summarized in Table 4.2.

N = No. of RX locations

M = No. of 2D scanner virtual array elements

FS = No. of frequency sweeps

Table 4.2 Measurements summary

S.N	Scenario	Polarization	Coating	Measurement Points (N×M×FS)	
1	Inside-outside	co-polar	no coating	16 × 25 × 2161	
2			windows with film	16 × 25 × 2161	
3			Al-foil complete car body covering	4 × 25 × 2161	
4			Al-foil window covering	16 × 25 × 2161	
5			Al-foil window stripped covering	16 × 25 × 2161	
6			open windows	4 × 25 × 2161	
7			no coating (RX height = 1.5m)	1 × 25 × 2161	
8			no coating (RX height = 2.5m)	1 × 25 × 2161	
9			no coating	4 × 25 × 2161	
10			windows Al-foil covering	1 × 25 × 2161	
11			cross-polar	no coating	16 × 25 × 2161
12				Al-foil window covering	4 × 25 × 2161
13	Intra-car	co-polar	windows with film	5 × 25 × 2161	
14			Al-foil window covering	5 × 25 × 2161	
15	Outside	co-polar	Al-foil window covering	4 × 1 × 2161	
16	Reference	co-polar	no car	16 × 25 × 2161	
17	Duration:	9 Hours	Measurements:	133	

4.3 UWB window film measurements

UWB window film measurement campaign was carried out in a specialized environment to evaluate the penetration loss through commercially available window films in both automotive and building category. The purpose of carrying out these kind of measurements was to single out the effect of these films on the communication of radio signals through precise and correct evaluation of penetration loss. Penetration loss, in this case, is simply the attenuation offered by the material of the films to the radio waves. For establishing generality, the term window film penetration loss (WFPL) is used throughout the content of this thesis.

4.3.1 Measurement location and environment

Anechoic shielded chamber in the I-wing of Aalto University, School of Electrical Engineering, was selected for window film measurements. The basic idea behind using this facility was to benefit from the shielded environment. The metal door opening was used to install a film under test so that transmitted signals including both LOS and MPCs from TX antenna only reach RX antenna by penetrating through the film. The access to the chamber was in the adjacent room facilitating sufficient spacing for measurements. The measurement environment with RX antenna on a tripod stand inside the chamber facing the metal door opening is depicted in Figure 4.17.

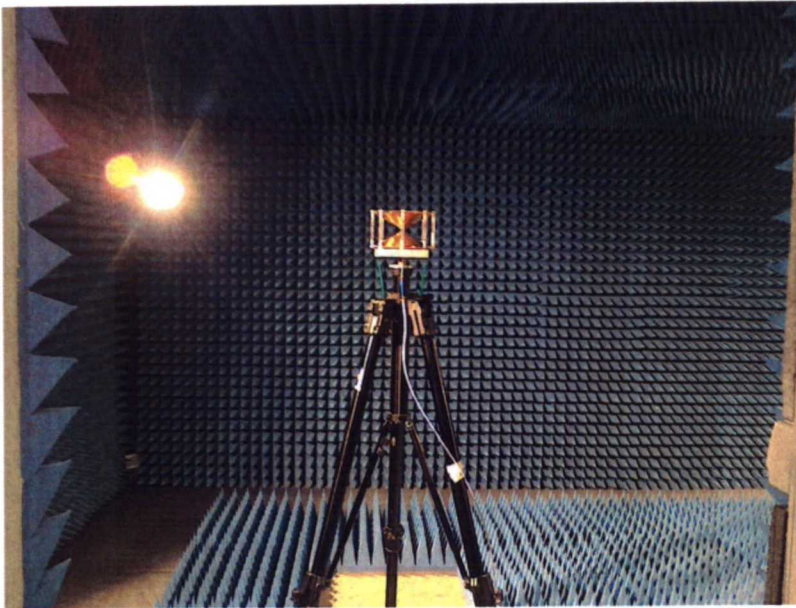


Figure 4.17 Measurement environment

4.3.2 Measurement layout description

The Figure 4.18 illustrates the layout of measurements conducted using anechoic shielded chamber facility. The metal door opening of the chamber is 2.133 m high and 0.8 m wide. The window films are usually manufactured in such a way that one side is adhesive which help in the installation process. The film under test was installed with the aid of its gluey surface sticking the flat metal extrusions on the sides of the metal door opening and reinforced by using a large number of magnetic strips of 30 cm length. The RF cable connection between the RX antenna mounted on a tripod stand inside the chamber and the VNA located outside the chamber was made using connector provided in the shielded wall of the chamber. The TX antenna also mounted on a tripod stand was placed in the line-of-sight (LOS) with RX antenna on the other side of the film. The minimum separation between TX and RX antennas was evaluated by considering the first Fresnel zone clearance at lowest frequency of the frequency range i.e. 0.6 GHz and accounting far field conditions. The room adjacent to the anechoic chamber in which its door opens, has a regular office environment with a large number of relatively small objects and structures. The adjacent room facilitated the measurement by providing sufficient space for performing measurements. As shown the Figure 4.18, VNA was kept outside the chamber for access and performing measurements while environment was kept static during measurements, i.e. no movement of any object.

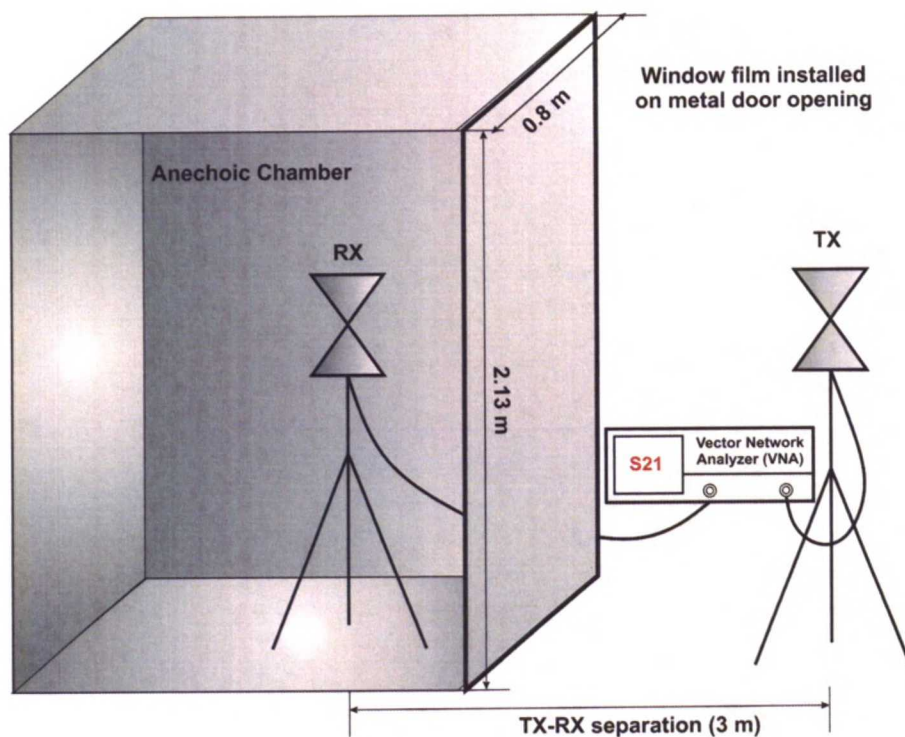


Figure 4.18 Measurement layout

4.3.3 Measurement equipment

The measurement equipment is more or less the same as that used in UWB car measurements described in Subsection 4.2.4. The Figure 4.19 presents the measurement equipment utilized in window film measurements.

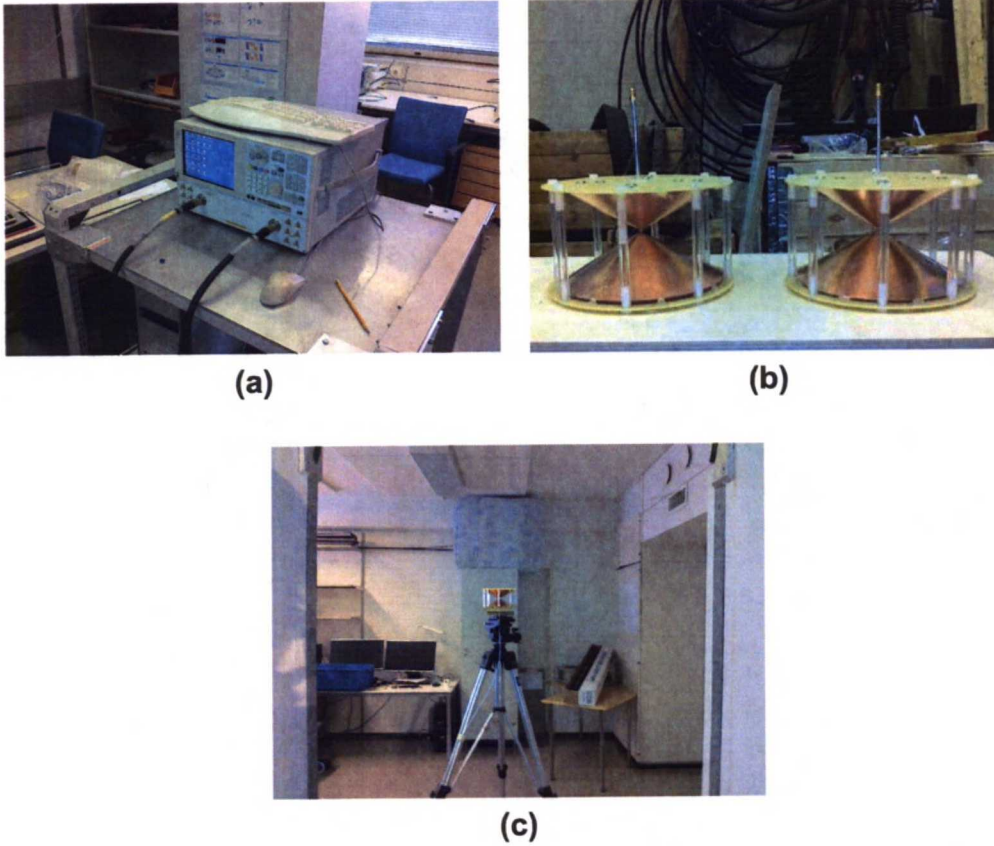


Figure 4.19 Measurement equipment; (a) VNA, (b) antennas, (c) tripod stand.

The measurement equipment used for UWB window film measurements is briefly described below.

- Agilent VNA-E8368A.
- UWB omni directional bi-conical antennas.
- Tripod stands for TX and RX antennas.
- RF cables
- Magnetic strips
- Window films

- PerformX Slate-50 (automotive series): This commercially available automotive window film is exactly the same which was used in UWB car measurements described in Section 4.2. The purpose of measuring this film was to exclusively assess the WFPL in relation to the VPL obtained in UWB car measurements.
- Century Nova-50 (building series): This commercially available building window film was used because it contains a complete integrated metal layer for maximum heat reject performance. Similar films for automobiles are also available and widely used, therefore, the evaluation of WFPL for this film was significant.

4.3.4 Measurement system and setup

The measurement setup is illustrated in Figure 4.20 and summarized in Table 4.3. The VNA measures S_{21} , the channel transfer function, whose magnitude provides the channel path gain. The measurement configuration is Single Input Single Output (SISO) which is sufficient for this kind of attenuation measurements. The frequency band used is 0.6 GHz to 6.0 GHz with the bandwidth of $B = 5.4$ GHz and number of samples defined for the measurements were $N_s = 2161$. A back-to-back calibration test was made to compensate for measurement cables and equipment. TX and RX antenna height was kept the same to 1.5 m. Single measurement duration was approximately 30-40 seconds approximately.

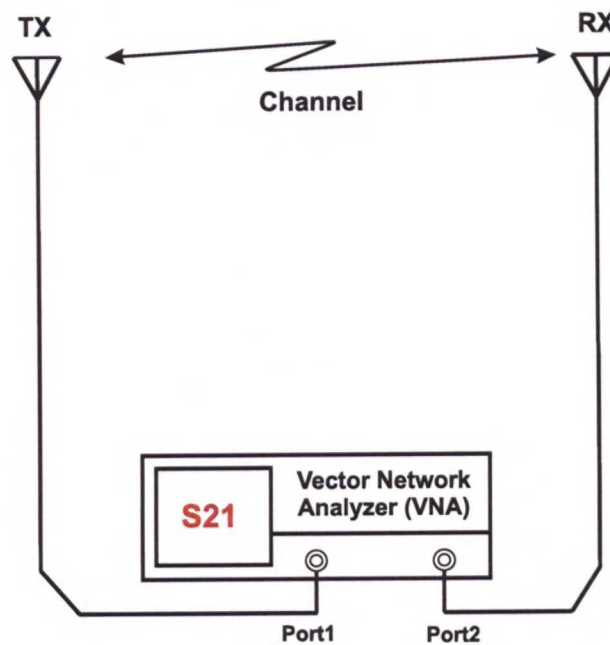


Figure 4.20 Measurement setup for window film measurements

Table 4.3 Window film measurement setup

Setup Name	Description
Configuration	SISO
Frequency band	0.6-6.0 GHz
TX/RX antenna	UWB omnidirectional bi-conical antennas
Antenna polarization	vertical
TX-RX antenna height	1.5 meters
System calibration	Back-to-back cable calibration
VNA settings	<ul style="list-style-type: none"> • IF bandwidth: 15 kHz • Output power: 7 dBm • Number of frequency points: 2161 • Frequency step: 2.5 MHz
Single measurement duration	30-40 seconds approx.
Measurement output	$S_{21}(f)$
Noise floor	-125 dBm

4.3.5 Measurement scenarios

The measurement scenarios considering two different window films and reference measurement are described briefly in this section. The Figure 4.21 presents the measurements performed for the first type of window film; PerformX Slate-50 (automotive series) abbreviated as PX-Slate. The Figure 4.22 illustrates measurements performed for the second type of window film; Century Nova-50 (building series) abbreviated as Century-Nova. The last measurement, shown in Figure 4.23, categorized as reference measurements were performed without any film on the door opening of the shielded chamber. This measurement serves as the reference for the other two measurements discussed above and is utilized to eliminate the environmental effects from the measurements. The TX-RX separation was kept at 1.5 m for all three measurement scenarios where RX antenna mounted on the tripod stand was placed inside the anechoic chamber and the TX antenna on the second tripod stand was placed outside the chamber in LOS conditions with RX through metal door opening of the chamber. The the data acquisition equipment, i.e. VNA resided outside the chamber in the adjacent room near the TX antenna as explained in the measurement layout Section 4.3.2.

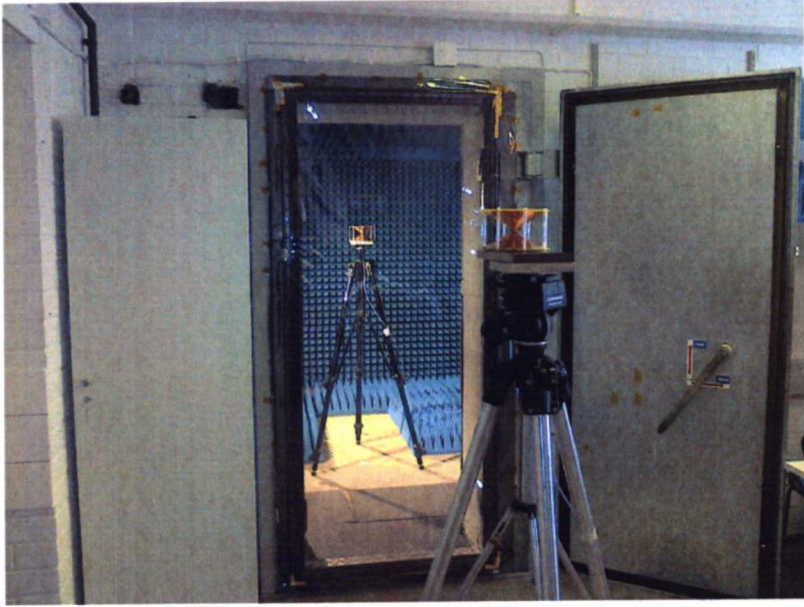


Figure 4.21 PX-Slate measurement



Figure 4.22 Century-Nova measurement

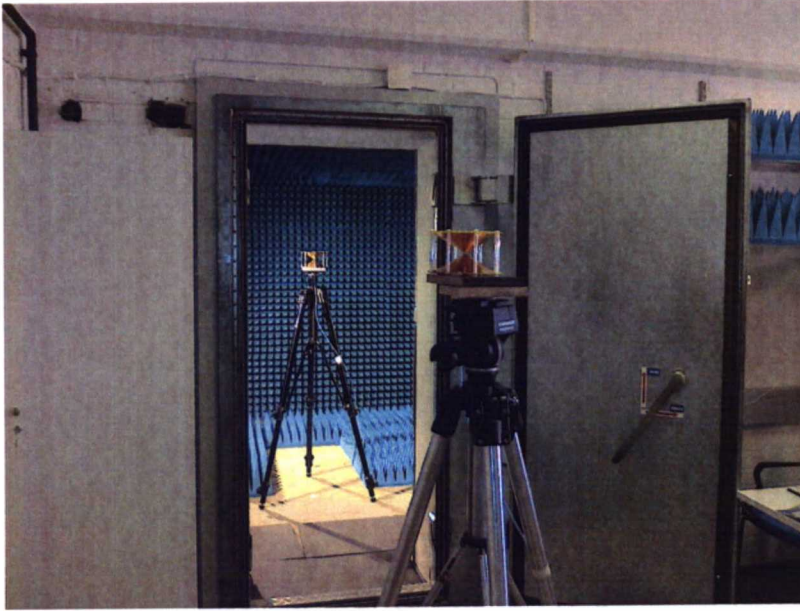


Figure 4.23 Reference measurement

4.3.6 Measurements summary

Table 4.4 summarizes the measurements performed under UWB window film measurement campaign.

Table 4.4 Measurements summary

S.N	Scenario	Polarization	TX-RX Height	TX-RX Separation
1	PX-Slate	vertical	1.5 meters	3 meters
2	Century-Nova			
3	Reference			

4.4 Summary

In this chapter, UWB measurement campaigns have been discussed for the evaluation of VPL and WFPL. The first measurement campaign described is UWB car measurements performed for the characterization of VPL. The measurement equipment used is described in detail along with the measurement system and setup. The measurement layout is given to provide the intuitive understanding of the measurements. Different scenarios considered for the measurements have also been explained comprehensively with illustrations. Finally measurements have been summarized in

a tabular form. The second measurement campaign presented in this chapter is the UWB window film measurements for the evaluation of WFPL. The measurement layout, setup and scenarios have been briefly covered with the help of illustrations.

Chapter 5

Data post-processing and analysis

5.1 Introduction

The data obtained from measurements is in rudimentary form which requires appropriate processing and manipulation to derive convenient and meaningful results identifying different characteristics of channel. The post-processing depends on measurement technique employed and the way measurement results have to be interpreted. In general, measurements are performed in order to characterize a propagation environment for wireless system design and optimization. In this prospect, the measurement data that quantifies propagation characteristics on statistical basis are required to be post-processed by exploiting signal processing algorithms.

Frequency and time domain techniques that are broadly utilized for propagation channel measurements and have been covered comprehensively in Chapter 2, provide observation of the radio channel in frequency and time domain. The duality relationship between frequency and time allows the results to be interpreted and analysed in both domains regardless of the measurement technique used. However, some additional processing steps may be required to achieve accuracy in the results. As described in Chapter 4, frequency domain measurements were carried out for the characterization of VPL. The delay domain characteristics that are closely related to system performance are obtained after frequency to time domain transformation as an initial step and exact parameters are evaluated after appropriate numerical treatment. This chapter deals with the post-processing of the data acquired from the measurement sets that are reported in Chapter 4 and the subsequent post-processed results have been analysed in-depth. The results analysis is the prime realm of this thesis and have been presented in a sequential manner with respect to the two distinct measurement campaigns including UWB car measurements and UWB window film measurements described in Chapter 4. At first, main signal post-processing steps which include data calibration, frequency data windowing and Fourier transformation from frequency domain to time domain data have been discussed followed by deriving channel characteristic according to the post-processing flow diagrams. The process involved in deriving channel characteristics such as channel transfer function (CTF), VPL, power delay profile (PDP) and delay spread (DS) has also been discussed in parallel.

5.2 UWB car measurements

For the evaluation of VPL, UWB car measurements were performed and have been described in Chapter 4. The measurement data obtained from individual measurement sets of corresponding scenarios was post-processed using Matlab and the results are analysed and elaborated in this section.

5.2.1 Post-processing flow diagram

Figure 5.1 presents the post-processing flow diagram of UWB car measurements. The measurement data retrieved from VNA for individual measurements undergoes system calibration by applying corresponding calibration data which serves as a reference for the elimination of other effects than actual propagation channel as discussed in the earlier section. The second common post-processing step involved was the windowing of frequency domain data for reducing sidelobe level and improving dynamic range. After these two common post-processing steps, channel parameters were extracted according to their numerical definition which is presented in the succeeding subsections. However, for delay domain characteristics, IFFT was used first for transforming frequency domain data into time domain.

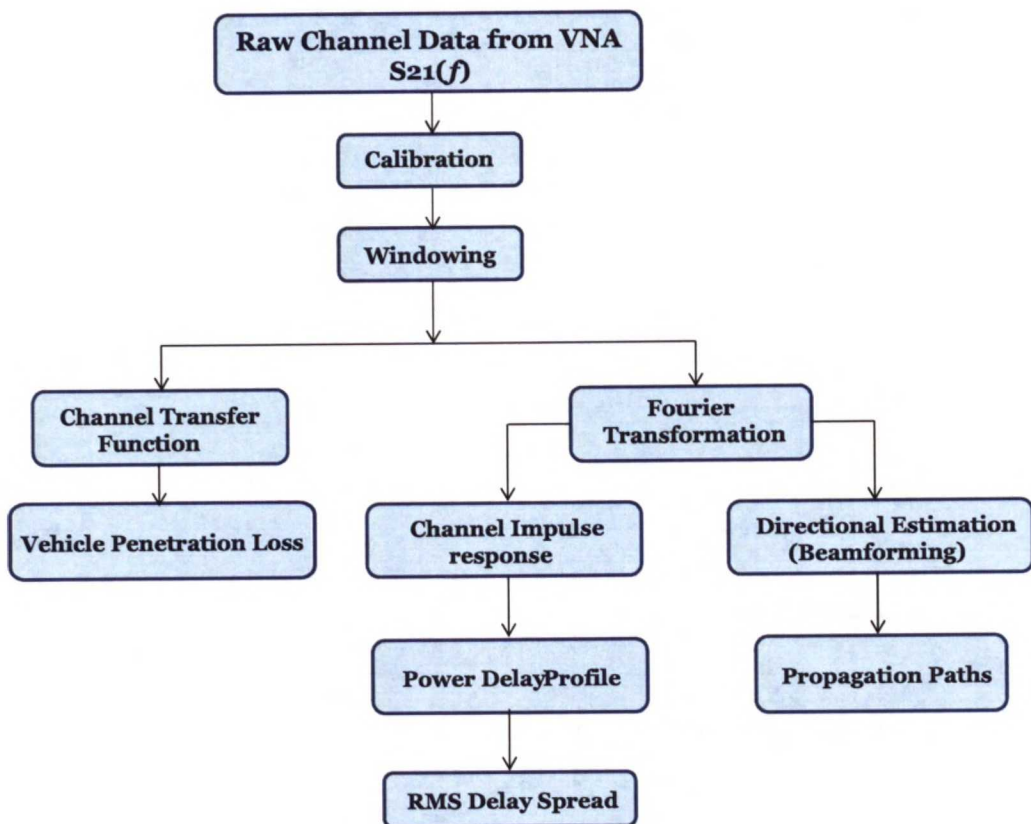


Figure 5.1 Post-processing flow diagram for UWB car measurements

5.2.2 Post-processing steps

The raw frequency domain measurement data obtained from VNA is in the form of forward complex scattering parameter $S_{21}(f)$ with both amplitude and phase information. This $S_{21}(f)$ does not truly represent the channel transfer function since it is engulfed with the effects of measurement system as well which must be excluded to obtain the true channel transfer function. Prior to the extraction of channel characteristics, following essential and main post-processing steps are considered.

5.2.2.1 Data calibration

The VNA measurements result in a transfer function $H_{\text{VNA}}(f) = S_{21}(f)$ which is a combination of three sub-components (i) transfer function of measurement system, $H_{\text{ms}}(f)$ (ii) transfer function of transmit and receive antennas, $H_{\text{ant}}(f)$ and (iii) true propagation channel transfer function, $H(f)$. The transfer function $H_{\text{VNA}}(f)$, obtained from the VNA, is in terms of integrated components given as:

$$H_{\text{VNA}}(f) = S_{21}(f) = H_{\text{ms}}(f) \cdot H_{\text{ant}}(f) \cdot H(f) \quad (5.1)$$

where $H_{\text{ant}}(f)$ is transfer function representing TX-RX antenna effects while $H_{\text{ms}}(f)$ is the transfer function of measurement system and includes the response of TX-RX units and RF cables, given as:

$$H_{\text{ms}}(f) = H_{\text{TX}}(f) \cdot H_{\text{RX}}(f) \cdot H_{\text{C}}(f) \quad (5.2)$$

where $H_{\text{TX}}(f)$ and $H_{\text{RX}}(f)$ are the transfer functions corresponding to TX and RX units of the VNA and $H_{\text{C}}(f) = H_{\text{TX-C}}(f) \cdot H_{\text{RX-C}}(f)$ is transfer function for RF cables connecting these units to respective antennas. The setup illustrating response of individual components is shown in Figure 5.2.

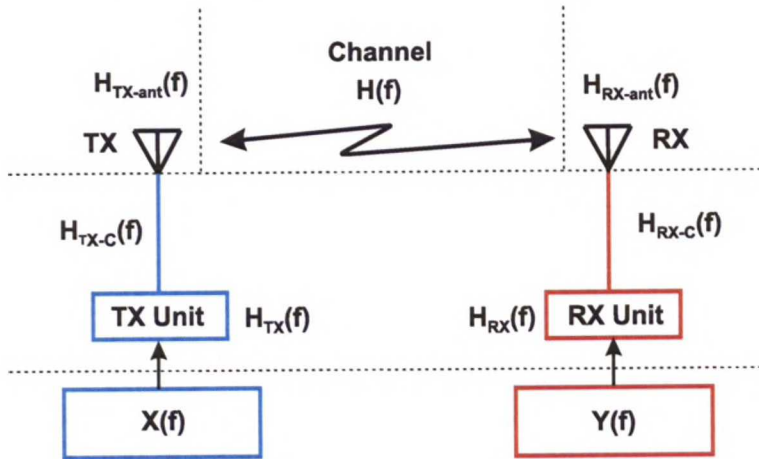


Figure 5.2 General measurement setup

In order to obtain the transfer function $H(f)$ of the propagation channel which is the only quantity of interest, all other effects must be eliminated. The removal of antenna effects is a difficult task and complicated directional estimation measurements are required in this regard. The directional measurements are necessary since MPCs are attenuated and distorted by the TX and RX antennas. These measurements cause additional errors in the results [18]. To avoid complexities, antennas are usually considered as a part of propagation channel particularly if omni-directional antennas are utilized and the combination of both is termed as radio channel. The scope of the measurements under this thesis also includes antenna effects in propagation channel transfer function. The simple and popular procedure that removes the effect of measurement system is back-to-back cable calibration. For this back-to-back calibration setup, the known signal $X(f)$ is transmitted from TX to RX connected through RF measurement cables used in the original measurement setup. The back-to-back cable calibration setup is depicted in Figure 5.3.

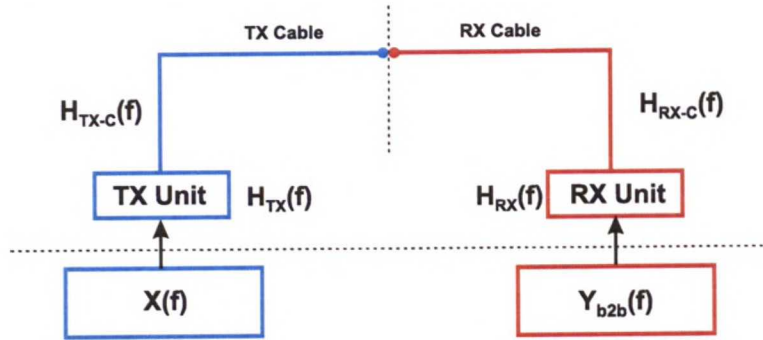


Figure 5.3 Back-to-back calibration setup

The received reference signal in the frequency domain is given as:

$$Y_{b2b}(f) = H_{TX}(f) \cdot H_{RX}(f) \cdot H_C(f) \cdot X(f) \quad (5.3)$$

where $H_{TX}(f)$ and $H_{RX}(f)$ are the transfer functions of TX and RX units in the VNA respectively. The calibration data obtained from this setup is compensated from actual measurement data and serves as a reference. The propagation channel combined with the antenna effects is referred as radio channel and the corresponding transfer function $H_r(f) = H(f) \cdot H_{ant}(f)$, undergoing calibration is thus given as:

$$H_r(f) = \frac{Y(f)}{H_{TX}(f)H_{RX}(f)H_C(f)X(f)} = \frac{Y(f)}{Y_{b2b}(f)} \quad (5.4)$$

While considering back-to-back cable calibrations, a careful step must be taken into account that VNA should not be switched off between back-to-back calibration measurement and actual measurements. Also the duration between calibration measurement and actual measurements should be kept small.

5.2.2.2 Windowing

Preceding the frequency to time domain transformation for obtaining delay domain characteristics, windowing of samples in frequency domain is considered. The ideal scenario for frequency domain measurements would be a continuous measurement over infinite frequency range. However, in practice, VNA is capable of measuring over limited frequency bandwidth.

Windowing is a process for signals measured in a finite measurement time or window. The windowing improves signal dynamic range by filtering frequency domain data before conversion to time domain reducing spectral leakage and producing lower sidelobes level. Thus, the effectiveness of observing time domain responses is enhanced to a great extent. The reduction in sidelobes level, on the other hand, is achieved at the cost of increased pulse width which determines the time resolution. VNA automatically applies a rectangular window for measurements offering a highest time resolution. The rectangular window in time domain gives a sinc function in frequency domain for the pulse with a maximum sidelobes level of 13 dB and the transformation is given as:

$$\text{rect}\left(\frac{t}{\tau}\right) = \tau \text{sinc}\left(\frac{\tau\omega}{2}\right) \quad (5.5)$$

where τ refers to the delay in time domain and ω in the function represents angular frequency. Hence, with rectangular window the time domain dynamic range is limited to 13 dB. The spectral leakage can be further reduced by softening or shaping the rectangular window using other window functions maintaining best fit to the compromise between pulse width and sidelobes level.

For wideband measurements where good dynamic range is one of main requirements, the typical window functions used are hanning, hamming, kaiser and Gaussian windows. For the measurements under the scope of this thesis, Gaussian window was employed for all measurement sets. The mathematical formulation of Gaussian window is given as:

$$w(n) = \exp\left[-\frac{1}{2}\left(\frac{n - (N - 1)/2}{\sigma(N - 1)/2}\right)^2\right] \quad (5.6)$$

where N is the number of frequency samples, n is an integer ranging $0 \leq n \leq N - 1$ and σ refers to standard deviation whose value is restricted to $\sigma \leq 0.5$.

A sample Gaussian window in time and equivalent frequency domain representation with sample size $N = 64$ is illustrated in Figure 5.4. The Gaussian window represented in Figure 5.4 has three characteristic parameters which include leakage factor=0.01% which is the ratio of power in the sidelobes to the total window power, relative sidelobe attenuation = -44.1 dB which is the difference of height of mainlobe peak to the highest sidelobe peak, and mainlobe width (-3 dB)=0.042969 which is the width of the mainlobe at 3 dB below the mainlobe peak.

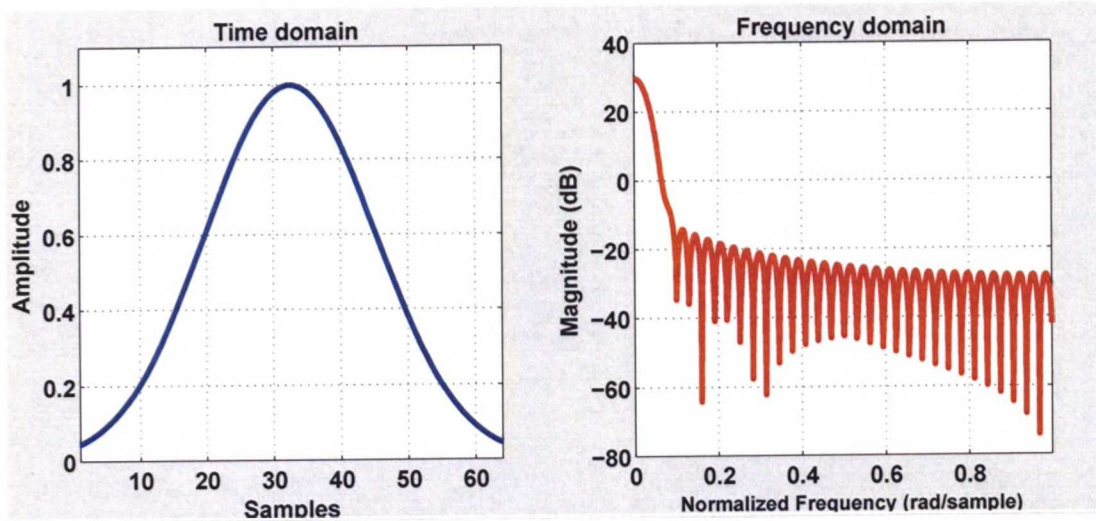


Figure 5.4 Gaussian window

5.2.2.3 Fourier transformation (FT)

The subsequent step after windowing the frequency domain samples of channel transfer function is frequency to time domain transformation which is accomplished using inverse fast Fourier transform (IFFT) producing channel impulse response. The fast Fourier transform (FFT) and its corresponding inverse function is given as:

$$X(k) = \sum_{n=1}^N x(n) \omega_N^{(n-1)(k-1)} \quad (FFT) \quad (5.7)$$

$$x(n) = \frac{1}{N} \sum_{k=1}^N X(k) \omega_N^{-(n-1)(k-1)} \quad (IFFT) \quad (5.8)$$

where ω_N is N th root of unity and given as:

$$\omega_N = e^{(-2j\pi)/N} \quad (5.9)$$

Typically there are two methods commonly exploited for the reconstruction of impulse response. These include complex baseband transformation and non-complex passband transformation. The complex baseband transform interprets the frequency domain samples as a complex baseband spectrum. Therefore, IFFT can be directly used without additional consideration. The impulse response obtained as a result consists of N_s samples with spacing $T = 1/B$ where B is the bandwidth and the maximum time span is given as:

$$T_{\max} = \frac{(N_s - 1)}{B} = \frac{1}{\Delta f} \quad (5.10)$$

where Δf represents the frequency step. Complex baseband transform method is efficient in terms of data processing efficiency and memory requirements.

On the alternate, the passband transform method also known as passband Hermitian reconstruction (PHR) in which passband signal is obtained from the measured signal by zero-padding down to DC and up to an arbitrary high frequency. This positive zero padded spectrum is then conjugate mirrored and added to the negative frequencies leading to the whole desired complex Hermitian symmetric spectrum as depicted in Figure 5.5. This includes the measurement data which is reconstructed to the frequency band in which it was originally measured. The time resolution achieved is twice as compared to complex base band method.

Due to simple and effective approach complex baseband transformation was used for processing all measurement sets under the scope of this thesis.

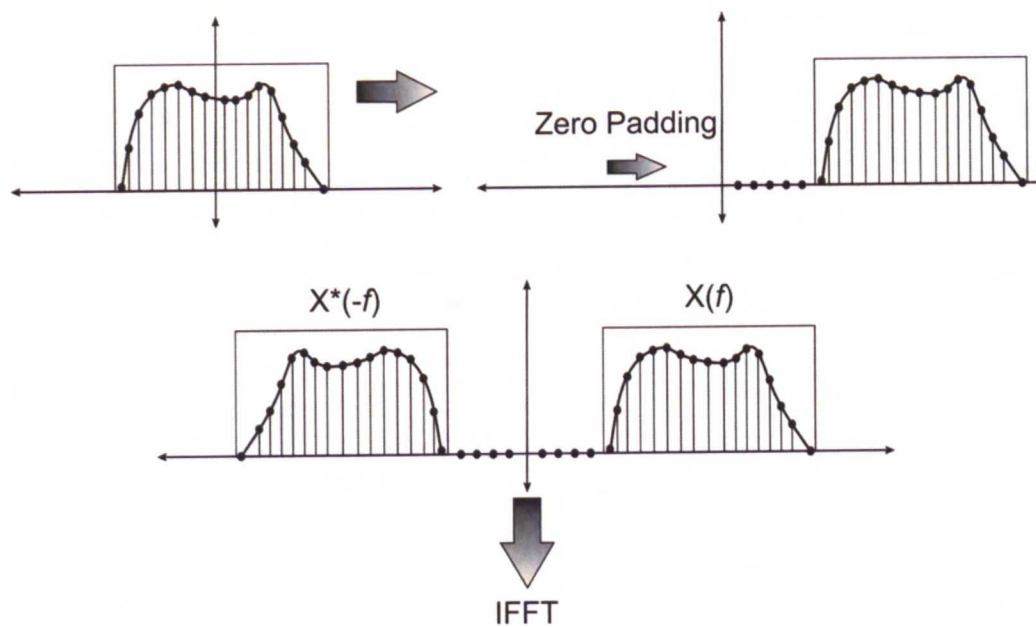


Figure 5.5 Passband Hermitian reconstruction (PHR)

5.2.3 Channel characteristics

Apart from channel transfer function all other parameters were extracted in the complete measurement frequency band i.e. 0.6-6.0 GHz and six different sub-bands with a absolute bandwidth of 0.9 GHz. These frequency sub-bands have been specified below:

- Sub-band I: 0.6-1.5 GHz
- Sub-band II: 1.5-2.4 GHz
- Sub-band III: 2.4-3.3 GHz
- Sub-band IV: 3.3-4.2 GHz
- Sub-band V: 4.2-5.1 GHz
- Sub-band VI: 5.1-6.0 GHz

Since UWB propagation channel is highly frequency selective, it can be expressed in terms of multiple sub-bands such that antenna gain, reflection, diffraction and scattering losses within each sub-band may remain constant. Also the behaviour of different channel parameters with respect to frequency sub-band allows more insight to frequency selectivity of channel characteristics.

5.2.3.1 Channel transfer function (CTF)

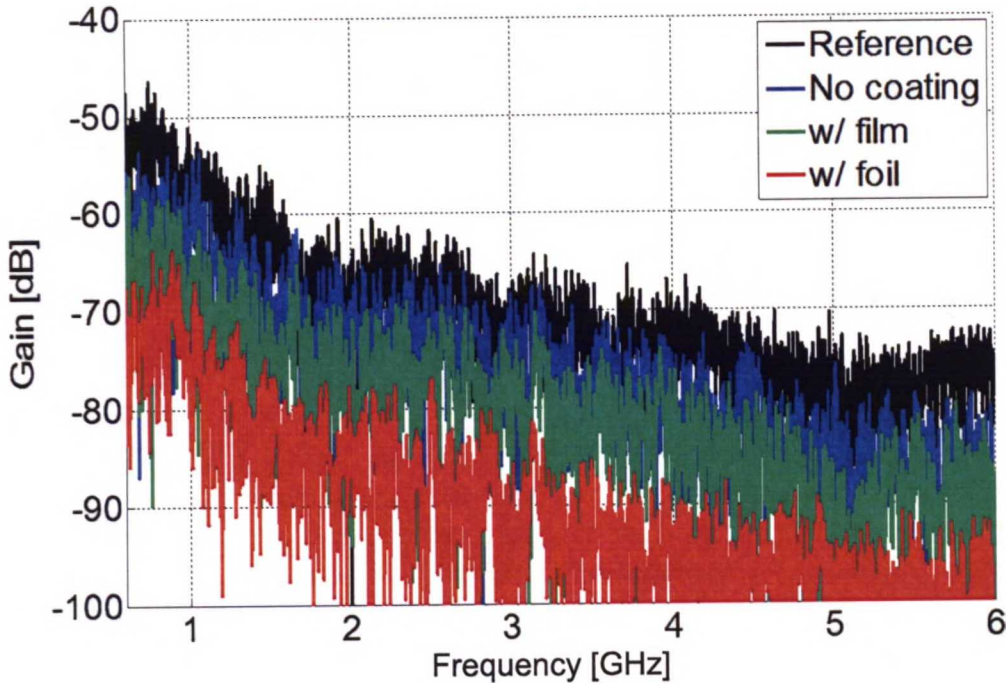


Figure 5.6 Channel transfer function for complete frequency band

The measurement data acquired from VNA in the form of $S_{21}(f)$ produces channel transfer function (CTF) after applying calibration. The plot in Figure 5.6 illustrates transfer functions of the measured channel with different settings. Four curves are plotted on the same Figure over the frequency range of the measurement settings after calibration.

The top most black curve represents the CTF for the Reference measurement scenario described in Chapter 4 subsection 4.2.6 without the car in the given environment capturing the effects of the environment only. All results have analysed with reference to this case. The next three curves include the car in the environment under the measurement scenario Inside-Outside but with different window coating configurations described in Chapter 4 subsection 4.2.6. The blue curve refers to the case when no coating was applied on the car windows. The green curve represents the case when automotive window film was applied to the interior surface of car

windows and the last red curve is the magnitude of CTF when Aluminium foil was used to cover car windows completely.

The curves display fast random fluctuations in the power level and exhibit a similar decreasing pattern with the increase in frequency. It is observable that the introduction of the car, window film and Aluminium foil incur extra losses on top of each other with respect to the reference case. On average 3, 7 and 20 dB losses were caused by car, car with window film, and car with Aluminium foil. It is also noticeable that losses are more prominent at the higher frequencies than at lower frequencies.

5.2.3.2 Vehicle penetration loss (VPL)

The VPL was evaluated in two components, i.e., with respect to the total signal power and line-of-sight (LOS) signal power. Since, the LOS component is the direct path and dominating component from TX to RX it contributes substantially to the received power. The attenuation of the LOS component is also quite significant in comparison to the losses for total signal power. The VPL for total signal power was derived by the difference in magnitude of CTF between the case under observation and the reference measurement. While VPL of the LOS signal power is the difference in magnitude of LOS component for the case under observation and the reference measurement. The magnitude of LOS component for respective cases was obtained from relevant power delay profile. The extraction of two VPL components are mathematically related as:

$$VPL_{(\text{Total-Power})} = P_{TC} - P_{TR} \quad (5.11)$$

where P_{TC} and P_{TR} are the total signal power for the cases under observation and the reference case respectively.

$$VPL_{(\text{LOS-Power})} = P_{LOSC} - P_{LOSR} \quad (5.12)$$

where P_{LOSC} and P_{LOSR} are the LOS signal power for the cases under observation and the reference case respectively.

In order to understand the directional characteristics of VPL, the two VPL components, discussed above, have been plotted in Figures 5.7, 5.8 and 5.9 for six frequency sub-bands with respect to the RX angle representing its traversal around the car in a 360° rotation. The RX angle was defined with respect to the reference center at the car rooftop where the galvanic connector was attached for out-letting the RF cable inside the car to RX around it. The corresponding measurement scenario, Inside-Outside, has been described in detail in Chapter 4 for different settings. Primarily, two main type of curves can be observed in Figures 5.7 to 5.9 including a continuous curve and a dashed curve. The continuous curve represents the VPL for total signal power while the dashed curve represents VPL for LOS signal power. These two curves have been plotted for three cases with the car in the environment considering different window coating configurations, (i) no coating (ii) with automotive window film and (iii) with Aluminium foil coating. During its

movement around the car, RX experience different face of the car. The RX angles in the abscissa of VPL plots stands for RX positioning around the car and hence correspond to different car faces given as:

- 0° or 360° : Car front
- 90° and 270° : Lateral sides of the car
- 180° : Car rear

In this view, it would be better to gain intuitive understanding of the car structure before plunging into the detail analysis of VPL. The car can be visualized as a metallic box like structure with windows as apertures on all four sides. The front and rear window apertures are larger and slanted as compared to the window apertures at the lateral sides. These window apertures provides the main propagation paths for radio waves accounting outside to in-vehicle communication. The other discontinuities include small holes in the chassis especially in engine compartment and rear trunk. A rough description of the car have been reported in Chapter 4.

In general, path loss increases with distance due to spreading of the energy as distance increases from the source. For Inside-Outside and reference measurements, the distance between TX and RX was almost constant in the radial axis. The variation in VPL with RX angle, is therefore, due to the shadowing effect of the car. Another noticeable observation is for no coating and window film cases, both VPL components displays an increasing trend as RX is moved from the front to the rear of the car and again levels with the VPL values as RX reaches back to the initial position. On average the difference of 4-5 dB in VPL values exists between car front and rear RX positions.

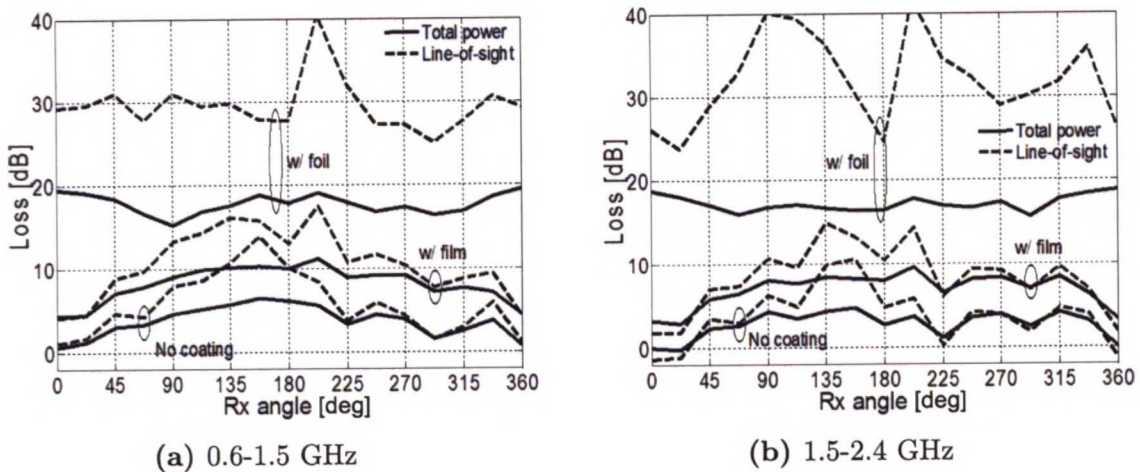


Figure 5.7 VPL for sub-bands I & II

For the no coating and window film case, the VPL for total and LOS power curves are almost analogous with small differences. Both VPL components nearly follow each other with RX angle. However, a difference arises between VPL for total

power and LOS power and become prominent at RX angles on the rear of the car. This difference in VPL level for total power and LOS power components is caused due the hatchback structure of the car and TX antenna being settled on the front passenger seat. Because of these factors, LOS path is easily shadowed at the rear of the car resulting in larger VPL for LOS power than total power. On the whole, the associated propagation mechanism for these two cases is essentially the ray paths through car windows.

When car windows are covered with Aluminium foil, the car is a shielded box with small slots in the chassis. The shielding scenario in this case does not allow radio waves to enter vehicle directly and instead the discontinuities in car chassis cause leakage of signals and contribute in the communication from car interior to outside. The VPL corresponding to the total power for Aluminium foil case shows a less varying trend throughout the RX angle range within sub-bands as compared to the other two cases. On the other hand, the VPL for LOS power varies significantly different RX angles within individual sub-bands. The average difference for VPL values between the RX at the front and the rear is 6-7 dB.

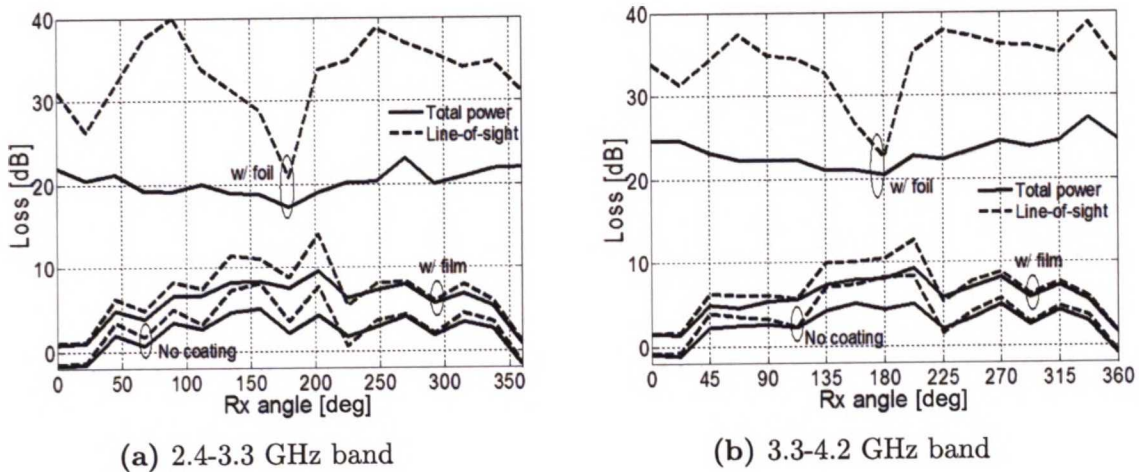


Figure 5.8 VPL for sub-bands III & IV

The difference between VPL for total power and LOS power is approximately 10 dB. The higher value of VPL for LOS is attributed to the blockage of LOS path when it undergoes penetration through shielding Aluminium foil. The shielding theory explained in Chapter 3 suggests that if the thickness of shielding material is much greater than the skin depth δ of the material at given frequency, the interacting signal is completely blocked. The skin depth of Aluminium foil with thickness 1 mm at lowest frequency 0.6 GHz and highest frequency 6.0 GHz is $3.3478 \mu\text{m}$ and $0.1059 \mu\text{m}$ respectively. Hence, the LOS path behaving like an optical ray easily get blocked and scattered from the Aluminium foil on car windows. On the other hand, the smaller VPL value for total power can be explained by a propagation mechanism called diffuse scattering. The diffuse scattering is ascribed to scattering from rough surfaces and near-field coupling. This scattering mechanism is robust against shadowing and shielding.

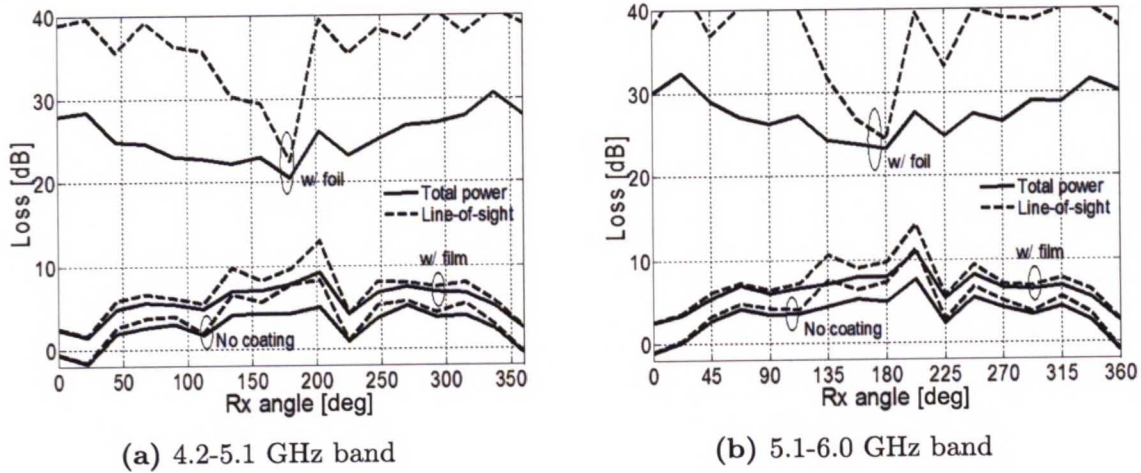


Figure 5.9 VPL for sub-bands V & VI

The VPL for LOS in Aluminium foil case exhibit low values at car rear and front as compared to the lateral sides which clearly indicates that LOS path gets some easy access due to improper shielding at rear and front windows.

Table 5.1 Mean VPL in dBs

Frequency [GHz]	Window coating configuration					
	No coating		Window film		Aluminium foil	
	Total	LOS	Total	LOS	Total	LOS
0.6-6.0	3.0	4.2	6.6	8.0	20.7	36.5
0.6-1.5	4.0	7.4	8.6	12.3	18.0	31.6
1.5-2.4	3.0	5.1	7.2	9.9	17.3	35.1
2.4-3.3	2.6	4.1	6.4	8.2	20.5	34.9
3.3-4.2	3.0	4.6	6.2	7.7	23.6	35.6
4.2-5.1	3.0	4.5	6.1	7.6	26.2	37.7
5.1-6.0	3.9	5.5	6.8	8.2	28.4	38.9

Table 5.1 summarizes the mean VPL over RX angles. The values show that the VPL due to the car with the film and with the Aluminium foil are 6.6 and 20.7 dB for the total power in the 0.6-6.0 GHz band among which the VPL due to the car itself is 3.0 dB. It means that the film and the Aluminium foil on the windows impose 3.6, and 17.7 dB losses in total power for the measurement settings. In general, the VPL for LOS power is larger than that of the total power. For Aluminium foil case, there is an increasing trend for the VPL with frequency. This might be explained with electromagnetic shielding phenomenon with metallic material where

it is more effective at higher frequencies than at lower frequencies since the skin depth is inversely proportional with frequency. A difference of 8 dB for VPL corresponding to total power can be seen between lowest and highest frequency sub-bands.

5.2.3.3 Power delay profiles (PDPs)

In order to form a synthetic array at the transmit side, TX antenna was mounted on an electro-mechanical scanner inside the car as described in Chapter 4. The CTF obtained from the VNA for each measured channel was transformed using IFFT into time domain channel impulse response (CIR) $h(t, \tau)$ after calibration and windowing. The CIR was absolute squared $|h(\tau, n)|^2$ to produce instantaneous power delay profile (PDP) and given as:

$$\text{IPDP}(\tau, n) = |h(\tau, n)|^2 \quad (5.13)$$

where τ is the delay and n is the position attained by TX on the synthetic array. The PDPs were then linearly averaged over the spatial array, in this case (5×5) , to obtain averaged power delay profile (APDP) which is given as:

$$\text{APDP} = \frac{1}{N} \sum_{n=1}^N \text{IPDP}(\tau, n) \quad (5.14)$$

where N is the number of synthetic array positions which is equal to $(5 \times 5 = 25)$ for the array settings. The term PDP is used interchangeably with APDP in rest of the text.

Comparison of PDPs for different cases in complete frequency band: The Figure 5.10 illustrates PDPs plotted in the same Figure for different cases evaluated for the complete frequency band and RX angle at 90° . The APDP in black represents the reference case without the car in the environment, the PDP in blue refers to the case with the car and without any window coating, the PDP in green stands for the car windows installed with automotive window film and the last PDP in red refers to the case when the car was covered with the Aluminium foil.

In the Figure 5.10, all PDPs begin with a strong peak, which is the direct path and dominant component between TX and RX referred as LOS component. The LOS component is followed by an exponentially decreasing tail with several peaks or spikes representing specular reflections and finally levels with the noise floor at -120 dBm. The exception is with the last PDP in red for Aluminium foil which demonstrates a different shape without any peak.

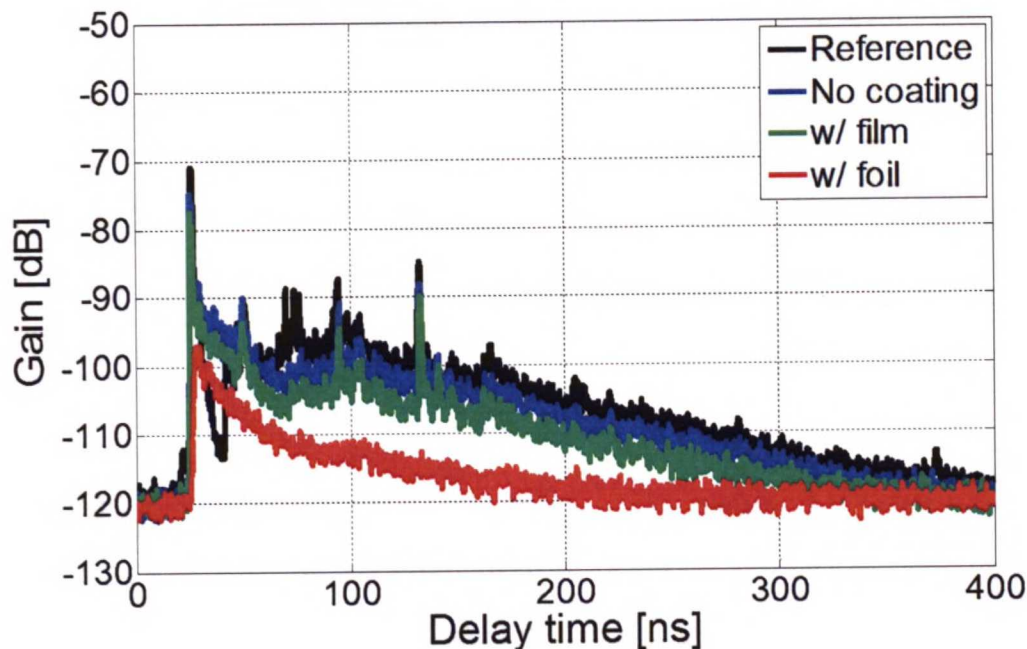


Figure 5.10 Power delay profile for complete frequency band at RX 90°

Now the difference between the PDPs of illustrated cases explain different propagation effects. In contrast with the reference case, the power level of the LOS component for PDPs decreases with the introduction of car by almost 3 dB. When window film was applied on the car windows, a 3 dB loss is further added making the sum equal to almost 6 dB. With the usage of Aluminium foil, the loss grosses up to 25-30 dB approximately. This essentially demonstrates that car windows provides the only exclusive path to radio waves to enter the car interior.

Second most noticeable thing in Figure 5.10 is the behaviour of PDPs within the delay range of 20-40 ns. The power level significantly increases in the this delay range for the three main cases (blue, green, red) with respect to the reference case (black). This is due to fact that when car is introduced the propagation of the radio waves is changed and now they are bouncing within the car compartment. All PDPs cases except Aluminium foil (red) displays a similar shape throughout the delay range and resemble each other except for the variation in power level.

Another prominent difference can be seen within the delay range of 70-80 ns where the peaks disappeared in the reference PDP after introducing car in the measurement setup. This is possibly caused by shadowing due the car.

When car windows were shielded with Aluminium foil, the power level decreases significantly and the shape of the PDP is different as compared to other three cases. All peaks have been suppressed as a result of the blockage caused by the Aluminium foil. The slope is also less abrupt. Ideally, the communication from inside to outside should be completely blocked due to shielding provided by the Aluminium foil on windows since the car chassis is completely metallic. However, we still see a diffuse

spectrum in the PDP which represents leakage of signals due to improper non-ideal shielding and contributions through discontinuities in the car chassis. The propagation mechanism is essentially shifted from distinct ray paths to diffuse scattering which has already been discussed in the preceding section.

Comparison of PDPs for different cases in frequency sub-bands: The Figures 5.11 to 5.13 represent PDPs for similar cases as that of Figure 5.10 but plotted for six individual frequency sub-bands and RX angle at 90° . Comparing the PDPs, the difference of power level becomes apparent. Observing PDP with the Aluminium foil case, the peak level differs by 20 dB between the lowest and the highest frequency sub-bands. In the highest band, the signal level is barely above the noise level of the measurement system. On the other hand, the peak level difference in the car with the film is only 5 dB between the lowest and the highest bands. The observation implies that different radio propagation mechanisms explain the losses. In the Aluminium foil case, the mechanism is leakage of radio waves due to improper shielding and hence is frequency selective. On the other hand, penetration is the dominant mechanism in the film case, which seems to be less frequency selective. The car structure does not significantly influence the losses even at low frequencies where the wavelength of the radio wave, for instance, at 0.6 GHz is about 0.5 m. The side windows have a height of 0.4 m, which almost corresponds to the wavelength at 0.6 GHz. This indicates that the frequency cut-off due to the window aperture is negligible for the frequencies of interest in the measurements.

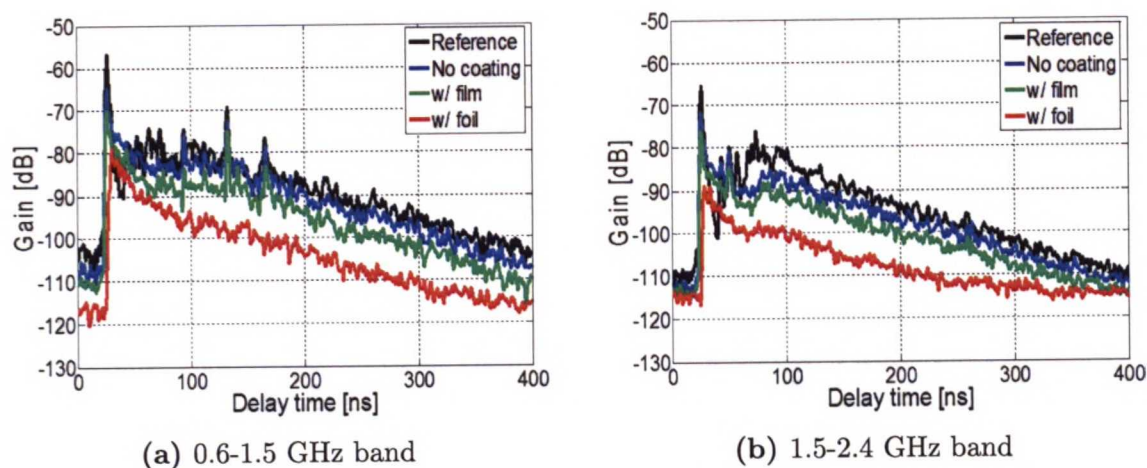


Figure 5.11 PDPs in I & II frequency sub-bands

Figure 5.11 illustrates PDPs for the first and second frequency sub-bands. The difference of power level throughout the delay range is evident which is on average 3-4 dB but the power for LOS component is significantly reduced by 5-6 dBs for all depicted cases. The decay of PDP tail appears to be at a constant rate after 100 ns delay in both frequency sub-bands. Another fact that can be noticed in Figure 5.11a is the suppression of specular peaks at 132 ns and 176 ns in the delay range.

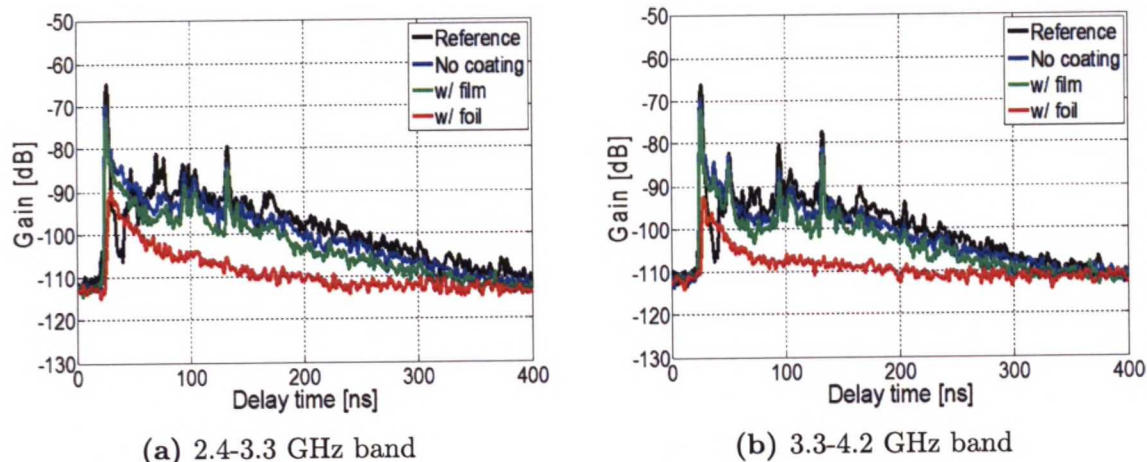


Figure 5.12 PDPs in III & IV frequency sub-bands

Figure 5.12 illustrates PDPs for third and fourth frequency sub-bands. In comparison to the first and second frequency sub-bands, the power level in Figures 5.12a and 5.12b is significantly reduced throughout the delay range, i.e., about 7-8 dB except for the LOS components which almost remain at the same level. The specular peaks have become prominent again. The PDP for Aluminium foil case with diffuse spectrum only is however scaled down and approaches the noise.

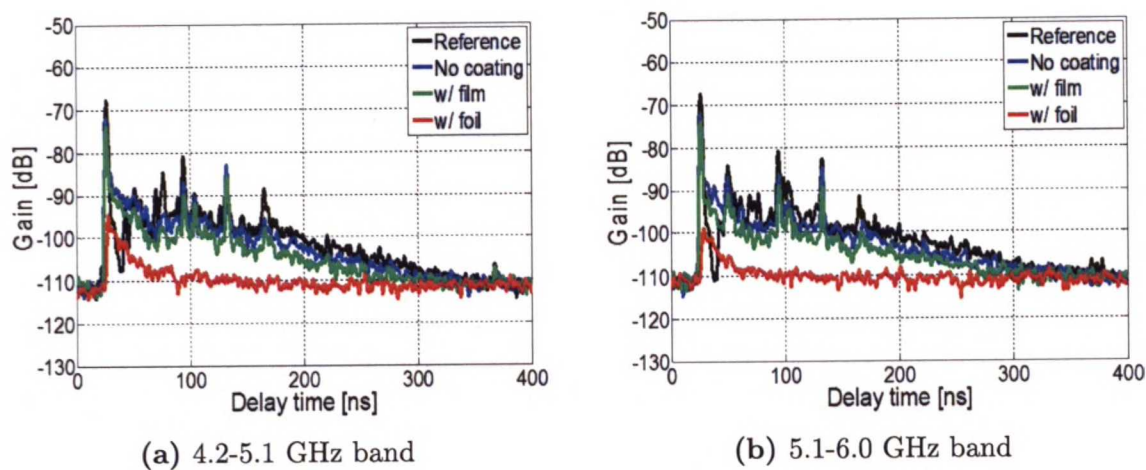


Figure 5.13 PDPs in V & VI frequency sub-bands

Figure 5.12 illustrates PDPs for fifth and sixth frequency sub-bands. The loss corresponding to each case appears to be more profound in the last two frequency sub-bands. The PDP for the Aluminium foil cases now almost levels with the noise floor due to the problem of limited dynamic range.

Influence of RX angle on PDP shape: In the previous cases, PDPs were extracted for RX angle 90° . To gain further understanding about the propagation

effects in the environment, it is interesting to observe the shape of PDPs obtained for RX positioned at different faces of the car. The Figure 5.14 illustrates the PDPs evaluated for the complete frequency band, i.e., 0.6-6.0 GHz for RX angles 0° , 90° , 180° and 270° . The PDPs almost track each other apart from a few salient differences within the delay range of 20-150 ns. A general statement to justify these differences is obviously the car structure. The first noticeable aspect is the difference in power level for the LOS component in all PDPs which come from the fact that LOS component is less shadowed for RX angles 0° and 270° as compared to 90° and 180° since TX was settled on the front right passenger seat which indicates that the extent of shadowing is different for right/left passenger seats depending on the position of RX antenna.

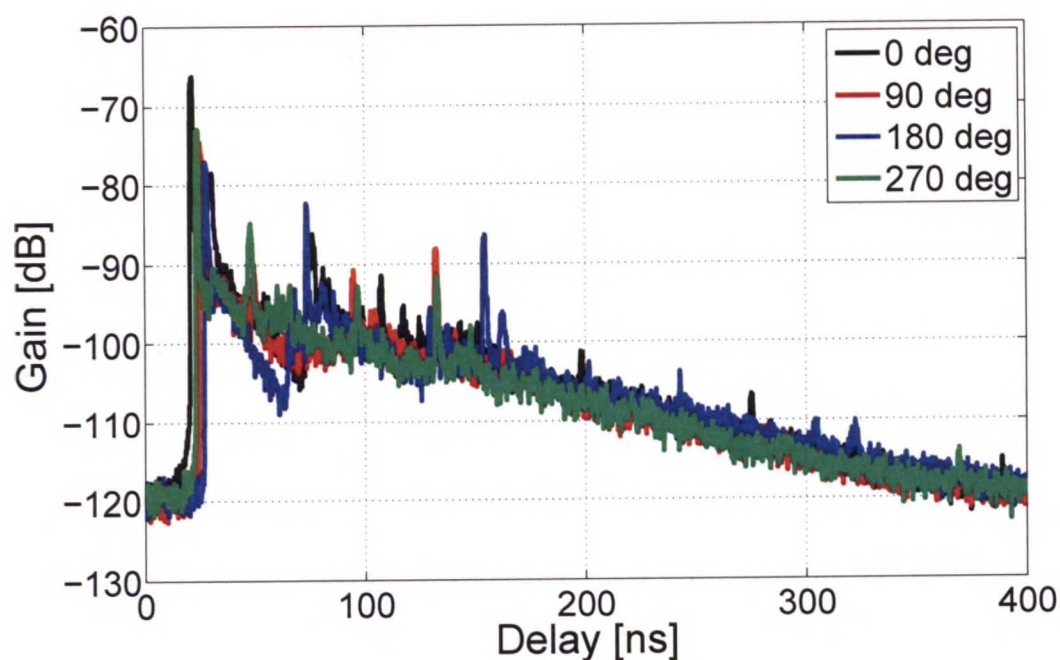


Figure 5.14 PDPs for 0.6-6.0 GHz frequency band with RX around the car

Besides the reduction in the power level, the absolute delay for LOS component for PDPs slightly differ. This difference can be explained from the inaccuracy in the measurement setup. It has already been discussed earlier that RX angles were specified with respect to the reference center at the rooftop of the car where galvanic connector was installed. The radial distance from RX to the reference center was kept constant, however, TX on the electro-mechanical scanner was settled on the front passenger seat resulting into slightly different TX-RX separation depending on the RX angle around the car.

The variation of absolute delay with the RX angles is depicted in Figure 5.15 for the environments with the car and the reference case without the car. The difference of 8 ns is observable between the RX angles corresponding to the front and rear of the car.

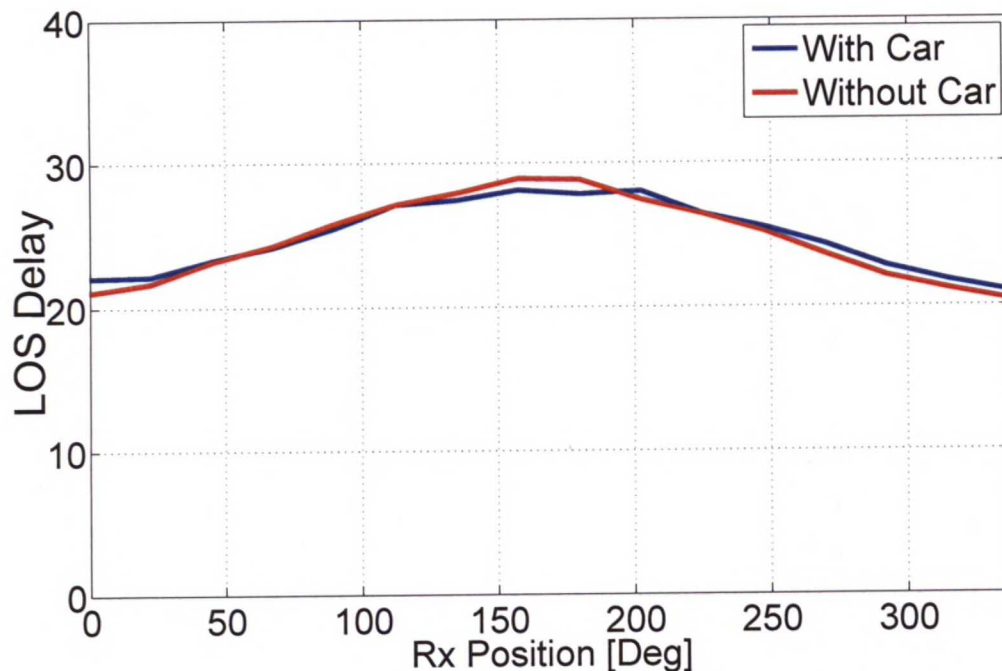


Figure 5.15 Variation of LOS delay w.r.t RX angle around the car

On the basis of resemblance and symmetry of the PDPs, the Figure 5.14 has been fragmented into two separate cases, illustrated by Figure 5.16, in order to present the difference in the shape of PDPs with the delay range of 30-80 ns. The PDPs in Figure 5.16a nearly follow each other except the small difference in delay and LOS power while the specular peak at 150 ns delay is also enhanced in the PDP for RX angle 180°. The PDPs in the Figure 5.16b are nearly the same. However, if comparing Figures 5.16a and 5.16b, indicate a clear difference within the delay range of 30-80 ns. The difference occurs possibly due to the car structure which symmetric on the lateral sides but asymmetric at front and the rear where the window aperture is large as compared to the side windows.

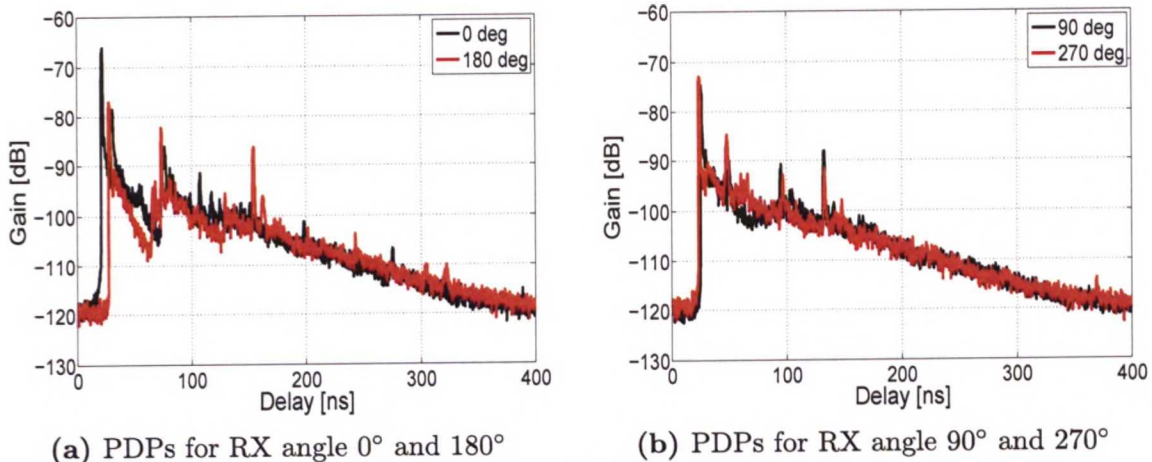


Figure 5.16 PDPs for 0.6-6.0 GHz frequency band with RX at front, rear and lateral sides of the car

PDPs for open and closed car windows: The Figure 5.17 shows the PDPs for RX angle 90° when car windows were open and closed. It is interesting to see that window glass offer negligible loss and the PDPs for the two cases are exactly the same.

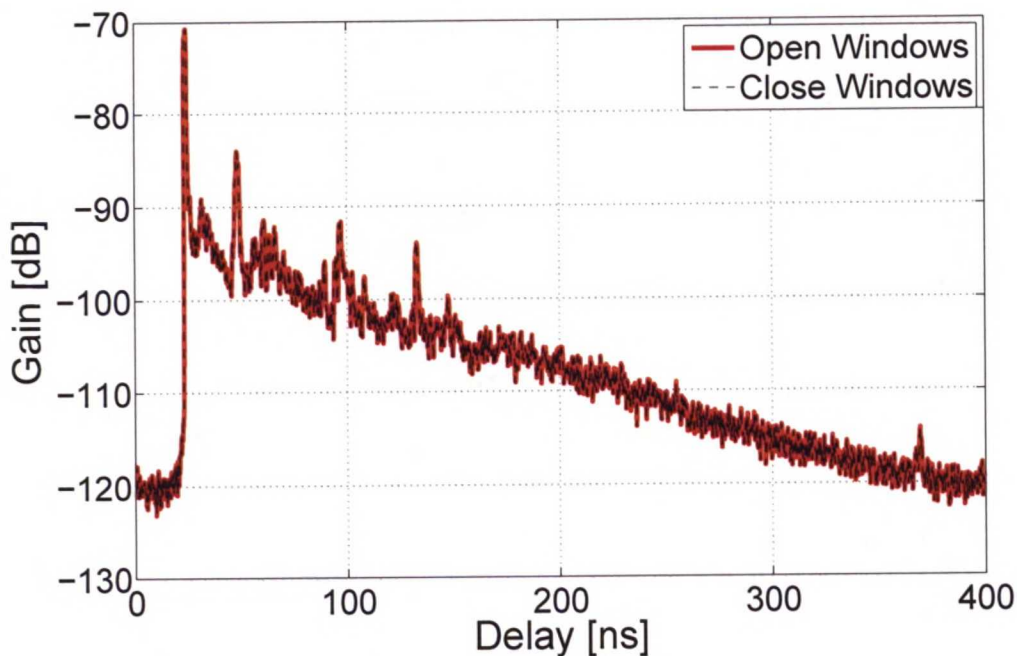


Figure 5.17 PDPs for open and close car windows at RX angle 90°

PDPs for human presence inside the car: In order to analyse the impact of human presence on the received signal, measurements with human subjects on the

driver and rear passenger seat were carried out. The scenario has been described in Chapter 4. Figure 5.18 presents the PDPs for RX angle 90° with and without human presence. In the presence of human subject, the power of the LOS component is reduced by 10 dB whereas the power of specular peaks at delay 90 ns and 132 ns is enhanced due to constructive interaction of MPCs arriving from different directions. The shape of PDPs, otherwise, exhibit a good correspondence.

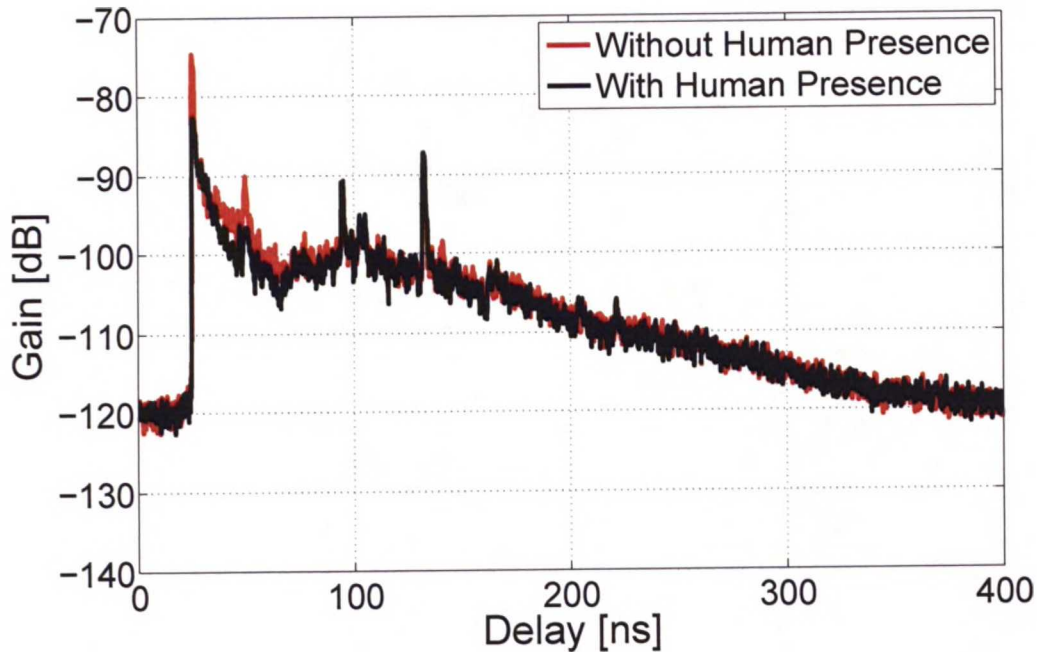


Figure 5.18 PDPs for RX angle 90° with human presence inside car

PDPs for different RX antenna heights: Another scenario that was considered in the measurements to examine the effect of RX height. Normally, all measurements were performed with 2 m height of RX antenna. However, two additional heights, 1.5 and 2.5 m were accounted in the measurements for RX angle 0° . Figure 5.19 illustrates the PDPs for these different heights of RX antenna. It can be observed that all three PDP trace each other except the specular peaks for 2.5 m case have risen by 2-3 dB with the delay range of 110-140 ns.

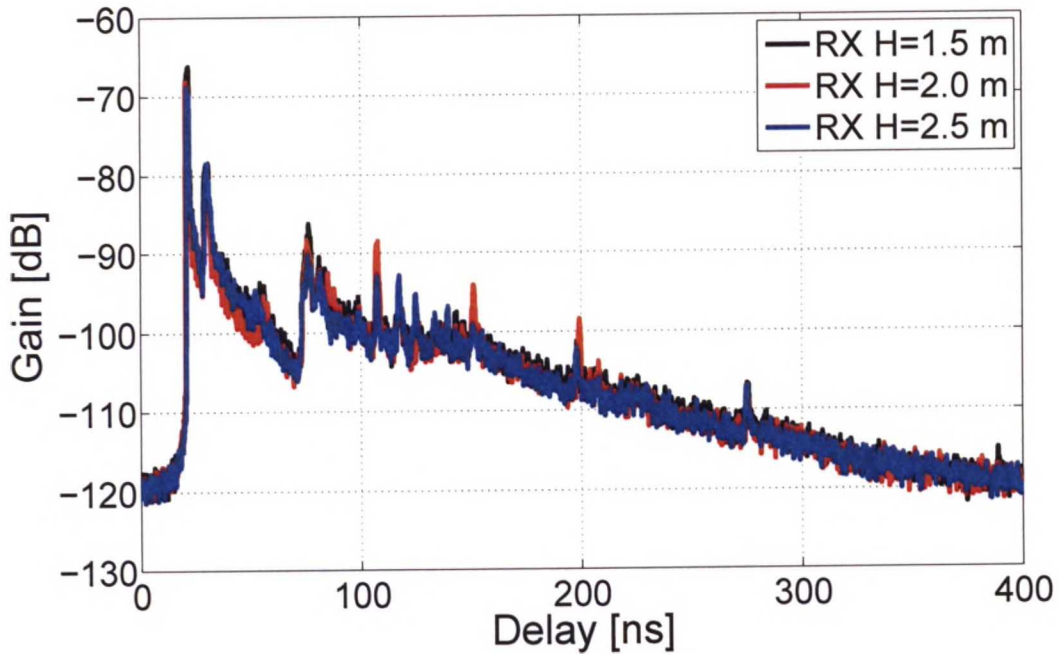


Figure 5.19 PDPs for RX angle 0° with different RX heights

PDPs for different Aluminium foil coating configurations: To imitate the condition of window film metallization, measurements were performed by covering car windows with Aluminium foil creating a shielding effect for interacting radio waves. Figure 5.20 and 5.21 represent PDPs in 0.6-6.0 GHz frequency band from all four sides of the car with different Aluminium foil coating configurations which include (i) complete Aluminium foil covering of windows of the car and part of its chassis (ii) on window covering and (iii) stripped window coating where Aluminium foil was stripped by 1 cm along the edges of the windows. The scenarios have been explained and depicted in Chapter 4.

The diffused spectrum in Figures 5.20 and 5.21 trace each other except for the power level which increases on average by 2-3 dB sequentially from complete Aluminium foil case to the stripped Aluminium foil case. It indicates that stripping of the Aluminium foil along the larger dimension of windows allow more energy to penetrate inside the car as compared to the other two cases.

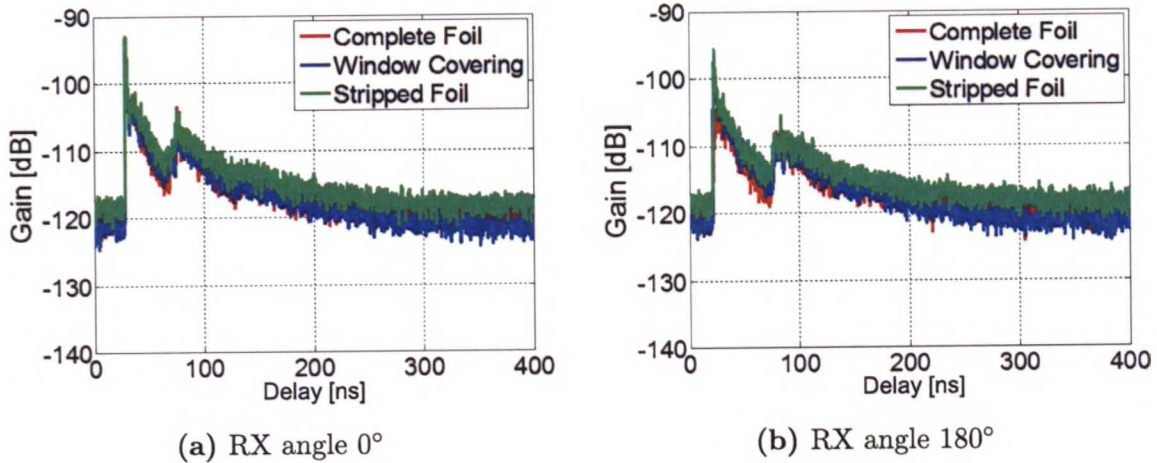


Figure 5.20 PDPs for 0.6-6.0 GHz frequency band with different Aluminium foil coating configurations at front and rear of the car

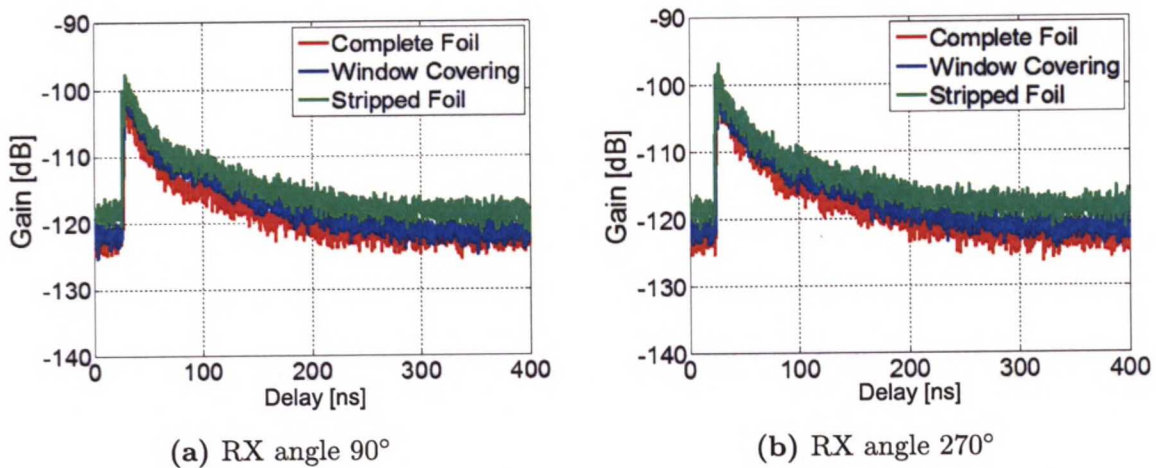


Figure 5.21 PDPs for 0.6-6.0 GHz frequency band with different Aluminium foil coating configurations at lateral sides of the car

PDPs for rooftop-to-car channels: Figure 5.22 shows the PDPs for rooftop-to-car channels with Aluminium foil only window covering configuration for the six individual frequency sub-bands. The specular peaks have been considerably suppressed in all PDPs which is similar to the Aluminium foil case for Inside-Outside measurement scenario. When comparing the highest and lowest frequency sub-bands, the level of the diffuse spectrum differs by 20 dB. On the other hand, the overall power level of PDPs is 10 dB higher in the rooftop-to-car scenario as compared to the Inside-outside case depicted in Figures 5.20 and 5.21 because of the shorter distance between the TX and RX antennas.

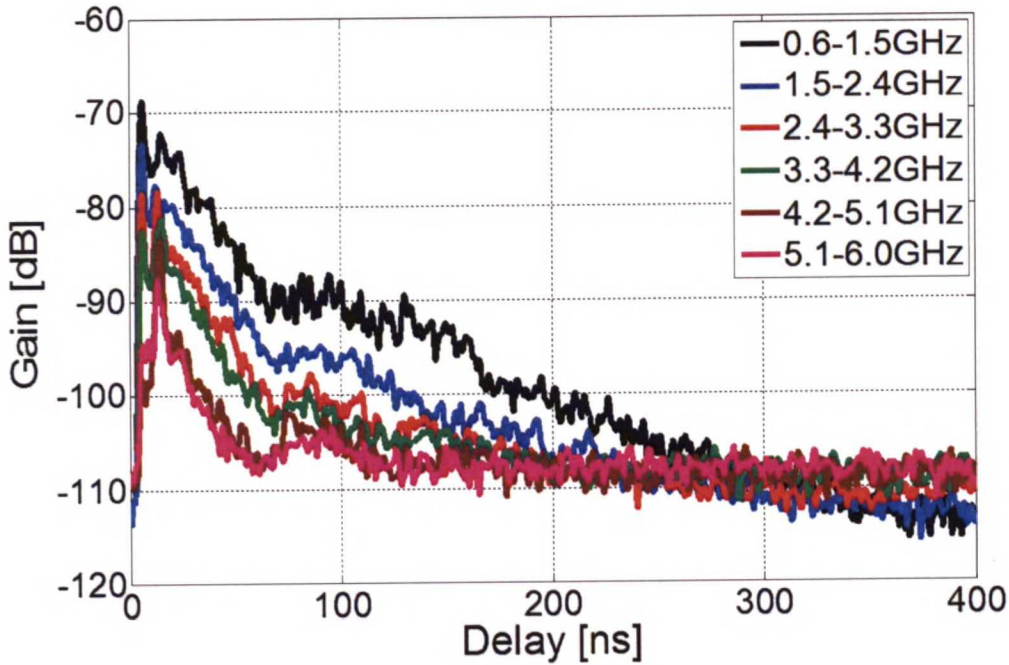


Figure 5.22 PDPs of radio channels from car roof-top to car interior with Aluminium foil covering on windows

Table 5.2 Total leakage level for rooftop-to-car channels.

Frequency [GHz]	Leakage Level [dB]
0.6-6.0	-69.1
0.6-1.5	-59.4
1.5-2.4	-64.8
2.4-3.3	-69.0
3.3-4.2	-71.3
4.2-5.1	-77.1
5.1-6.0	-79.9

The leakage level for rooftop-to-car channels have been summarized in Table 5.2. The coupling between the rooftop and intra-car antennas is -69.1 dB for the 0.6-6.0 GHz band. However, by comparing the lowest and highest frequency sub-bands for the leakage level, the coupling is clearly stronger in the lowest sub-band than in the highest by 20 dB.

PDPs for cross-polar channel: In order to explore the cross-polar channel, the RX antenna was changed from vertical to horizontal and measurements were performed as described in Chapter 4. For the comparison between and co-polar and cross-polar channels, PDPs for RX angle 0° have been plotted for both cases in Figure 5.23 for 0.6-6.0 GHz frequency band. The difference between the two channels is evident between the delay range 25-120 ns where the power level has been significantly reduced for the cross-polar channel and otherwise the tails of both PDPs follow each other and decay with the same rate as the delay increases. For the LOS component the power level difference between both channels is 15 dB. In addition to this, the specular peaks have been considerably suppressed in the cross-polar channel PDP and diffuse components dominate.

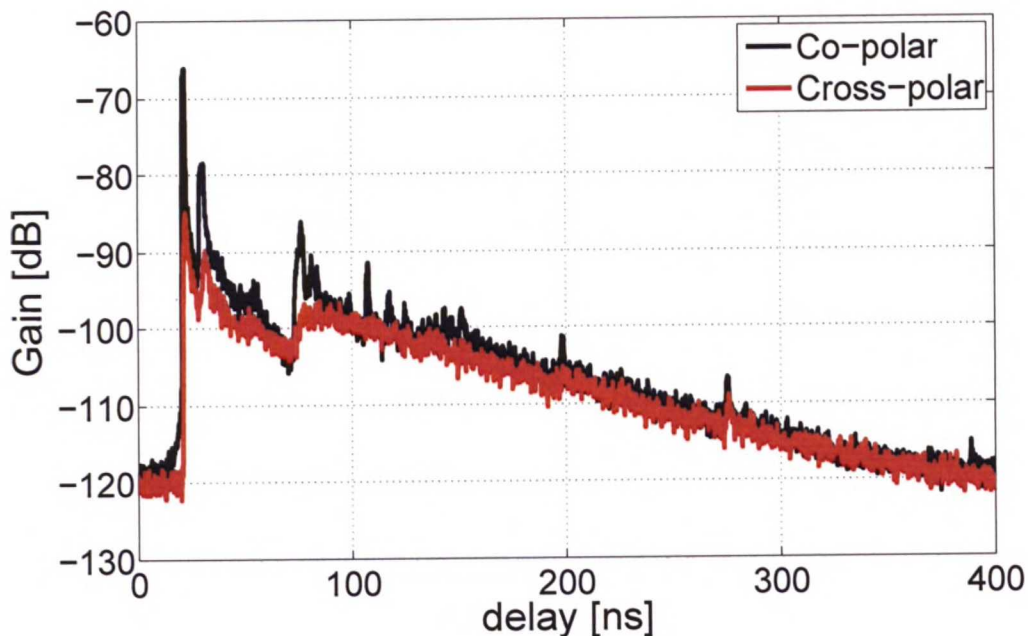


Figure 5.23 PDPs for 0.6-6.0 GHz frequency band at RX angle 0° with co-polar and cross-polar channel

An obvious reason for the suppression of MPCs is the polarization mismatch between TX and RX antenna. It can be understood by considering the surface of objects in the environment. The common objects in the indoor environments have surfaces that either tend to be horizontal or vertical and thus preserves the polarization of the impinging wave that propagates according to the transmit antenna polarization. It is known from the theory that parallel and perpendicular polarizations have different transmission and reflection coefficients which impacts the received signal at RX.

A comparison for the PDPs of cross-polar channels with and without Aluminium foil on the car windows has been performed in Figure 5.24 and 5.25 where PDPs have been extracted for RX at front, rear and sides of the car. The only window covering

Aluminium foil coating configuration was used. The most noticeable observation for all PDPS is that the diffuse spectrum is dominating regardless of the use of Aluminium foil on the car windows.

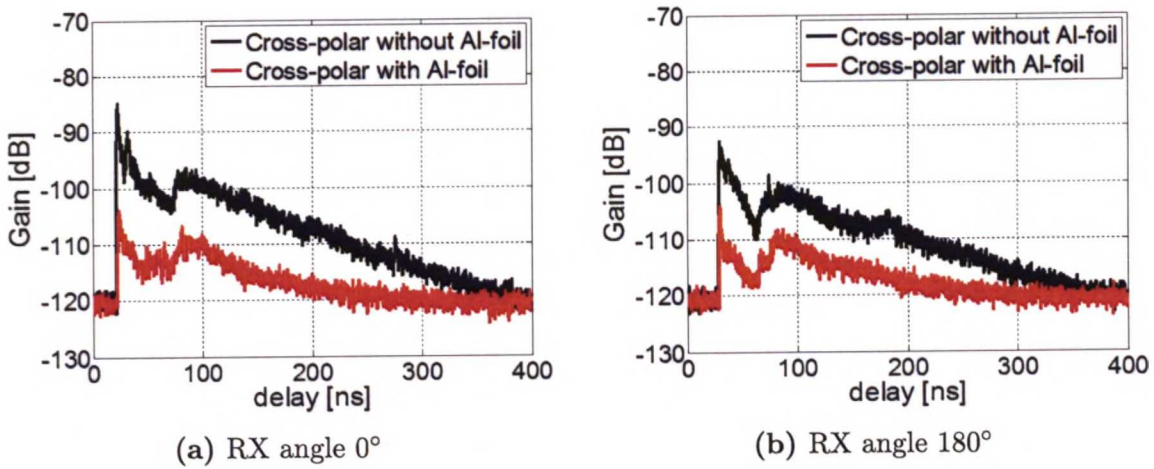


Figure 5.24 PDPs for 0.6-6.0 GHz frequency band for cross-polar channel

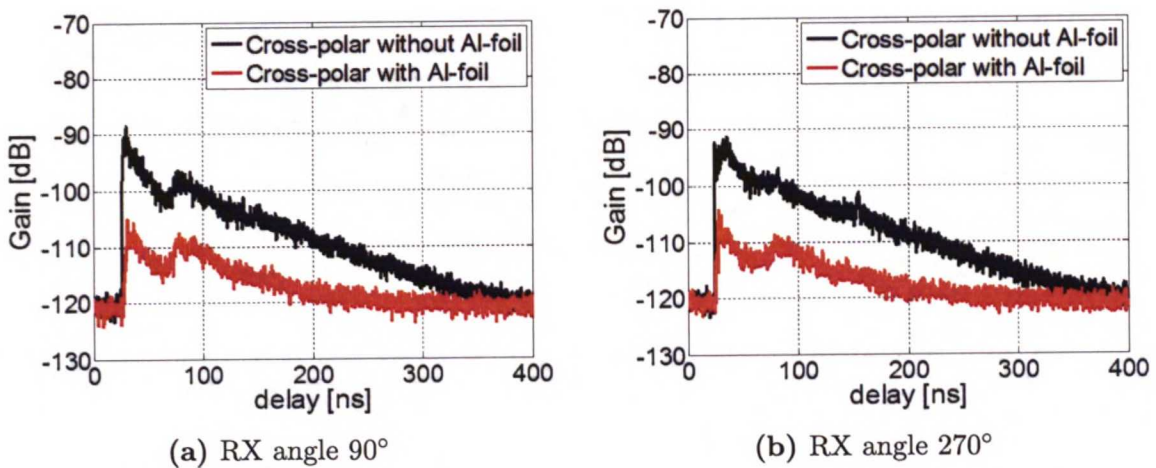


Figure 5.25 PDPs for 0.6-6.0 GHz frequency band for cross-polar channel

A clear influence of Aluminium foil is visible in all PDPs where the power level has been reduced on average 10 dB over all delay up to 340 ns. The decay rate of PDPs with and without Aluminium foil is quite different from each other.

PDPs for Intra-car measurements: To account for the situations when communication happens between car peripherals or terminals inside the car, intra-car measurements were performed. Five RX positions on a fixture inside the car between driver and rear passenger seat were considered while TX rested on the electro-mechanical scanner on the front passenger seat as described earlier in Chapter 4. Figures 5.26a and 5.26b present PDPs evaluated for five RX positions with and

without Aluminium foil coating on the car windows in 0.6-6.0 GHz frequency band. The only window covering Aluminium foil coating configuration was used.

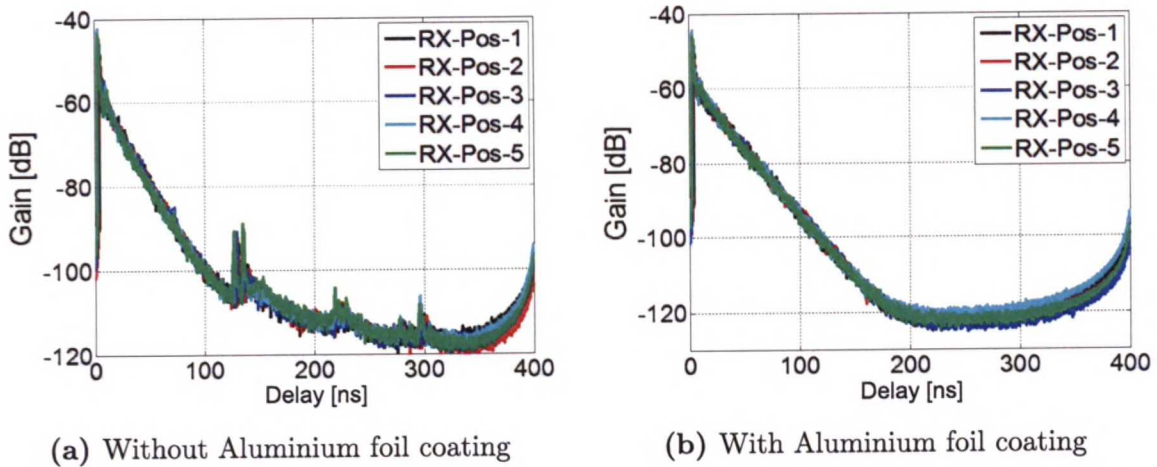


Figure 5.26 PDPs for 0.6-6.0 GHz frequency band Intra-car measurements for five RX positions

The strong response of PDPs in both Figures 5.26a and 5.26b are concentrated up to 200 ns after which the tails continue on the noise floor. In comparison to Inside-Outside measurements, the power level is higher due to the small TX-RX separation. In both cases, with and without Aluminium foil, the LOS component begin at the same level i.e. -40 dB. In Figure 5.26a, the PDPs for all RX position exactly trace each other throughout the delay range. The PDPs consist of four clusters. The first cluster starts with the dominant LOS component at 3 ns delay and decays quickly with a constant rate ending at 120 ns. The second relatively weak cluster begins at 120 ns and decays almost completely by 220 ns. This cluster possibly occurs due to radio waves leaving the car compartment, interacting with the objects outside and received by the RX inside the car. The third and fourth clusters are very weak and approaches the noise floor. On the other hand, the PDPs in the Figure 5.26b with Aluminium foil case shows a single cluster with diffused components which decays at a constant rate and reaches the noise floor at 200 ns. The MPCs bounces within the car compartment and decays due to leakage from the slots in the car chassis. For a close comparison, PDPs for the two cases with and without Aluminium foil have been plotted in Figure 5.27 for RX position 2 on the fixture .

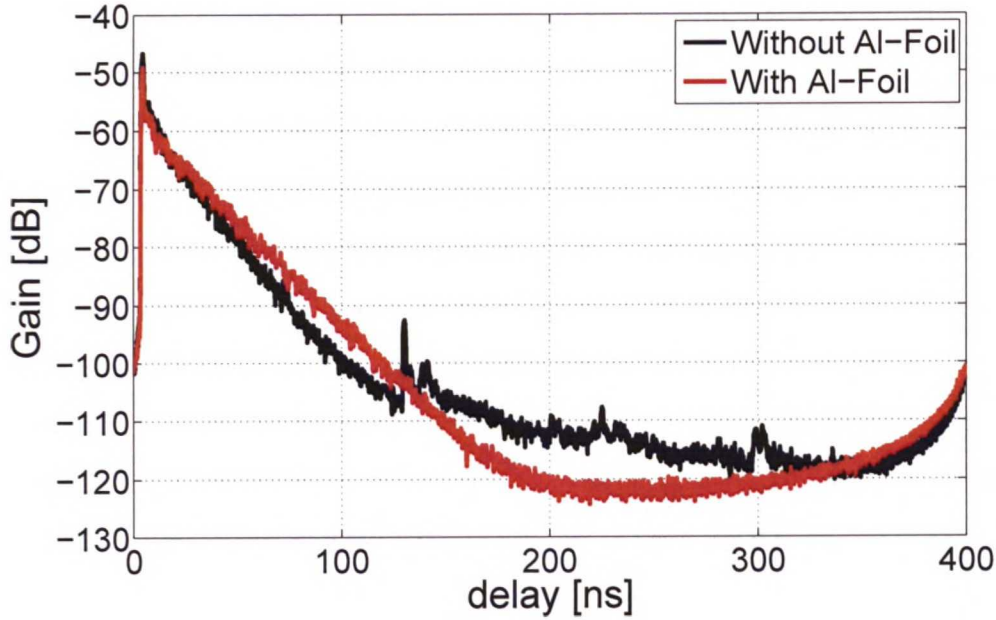


Figure 5.27 PDPs for 0.6-6.0 GHz frequency band Intra-car measurements with and without Aluminium foil

PDPs for Outside measurement: The measurements under the Outside scenario were performed with TX at the center of car rooftop and RX around the car as described in Chapter 4. Figure 5.27 illustrates the CIR evaluated for RX positioned at all four sides of the car 0.6-6.0 GHz frequency band. Due to resemblance, the CIRs for RX angle 0° , 180° and 90° , 270° are plotted together in Figures 5.28a and 5.28b respectively. The CIRs exhibit random fluctuations in magnitude indicating the presence of small-scale variations. The LOS component of all CIRs have a power level of about -57 dB.

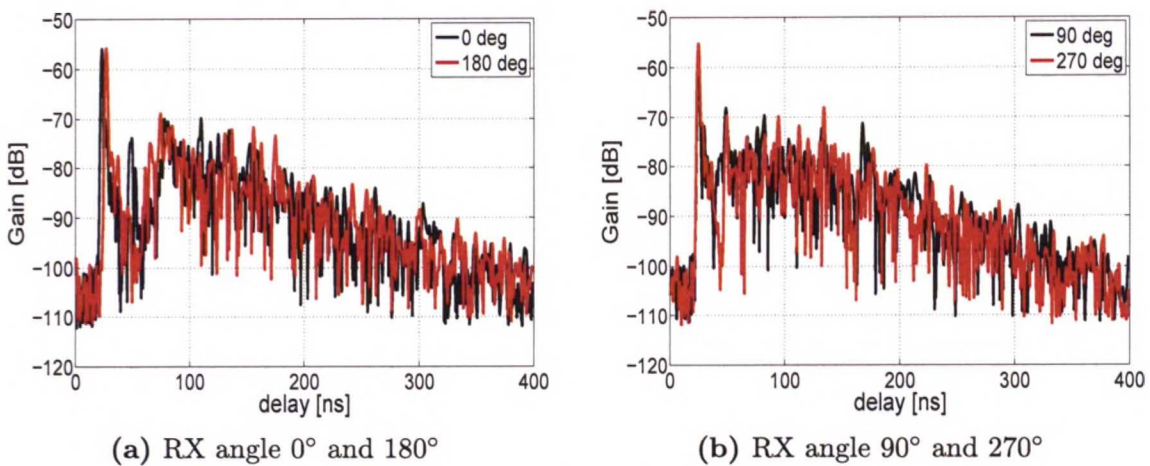


Figure 5.28 CIRs for Outside measurements

5.2.3.4 RMS delay spread (DS)

The RMS delay spread (DS) is the second central moment of PDP and is calculated for individual cases. For evaluating DS, a threshold level was set to consider the meaningful signal only. The threshold level was estimated with a maximum of +5 dB noise level and a peak signal level of -20 dB in the PDP under consideration.

The variation of the DS with respect to the RX angles has been plotted for six individual frequency sub-bands in Figures 5.29 to 5.31 which demonstrate a clear influence of the RX angle on the DS which increases when the car is introduced in the environment. As RX is moved towards the rear of the car, a significant increase in DS can be seen. The difference is more apparent in the lower frequencies as compared to the higher ones. On the other hand, the delay spread remains almost at the same level when the RX is at the front side of the car, regardless of the frequency. The difference can be explained on the basis of the window size and car structure which is different at the front and rear of the car. The front window aperture is large enough and does not shadow the LOS component much while the rear window is relatively smaller and furthermore the large trunk shadows the LOS component easily. The fact is even reinforced from the PDPs evaluated for the rear locations of the car where the power of LOS component was reduced by 10 dB as compared to the front whereas the other MPCs are less shadowed since the pathways are not necessarily through the rear window. As a result, more delayed MPCs are dominating the channel when the RX is at the rear, making the delay spread larger.

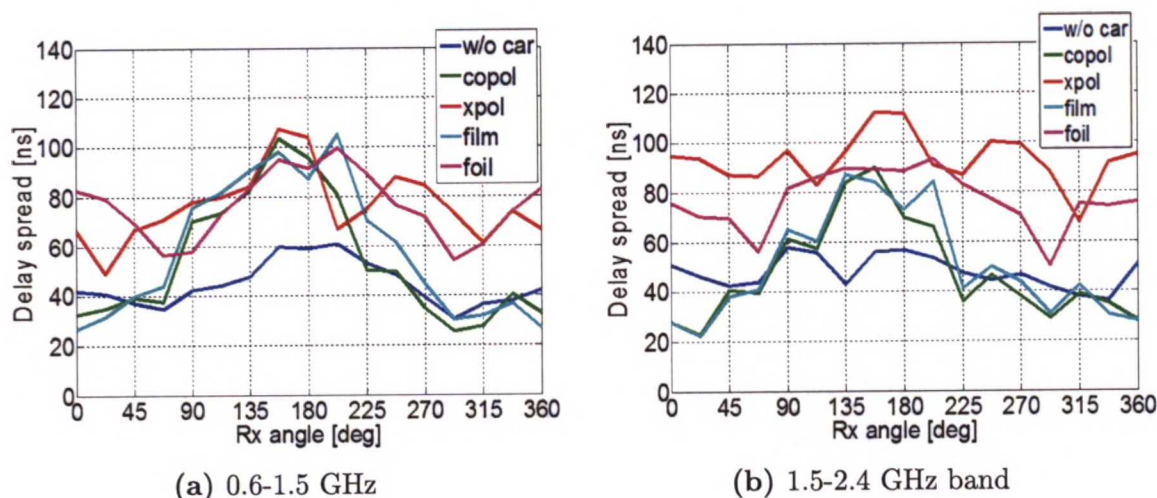


Figure 5.29 RMS delay spread in frequency sub-bands I & II

The shadowing of the LOS component by the rear window is less significant at higher frequencies because the window size become electrically large as the frequency increases, rendering the difference of the DS at the rear of the car smaller at the higher frequencies. It is worth noticing that the DS can be twice as large as it is without the car when the RX antenna is positioned at the rear angles. The DS estimates with and without window film cases appear to be in a similar level with small deviations.

While comparing the DS with and without Aluminium foil at the three lower frequency sub-bands given by Figure 5.30b, 5.31a and 5.31b, the noticeable difference appears when the RX is at the front of the car where the increase in DS is two fold. This is possibly due to the fact that Aluminium foil blocks the LOS considerably and resist its penetration through the front window. On the rear side, the DS is almost the at the same level as that of the no coating case, although the signal level is quite different with respect to the Figures 5.29a, 5.29b, and 5.30a.

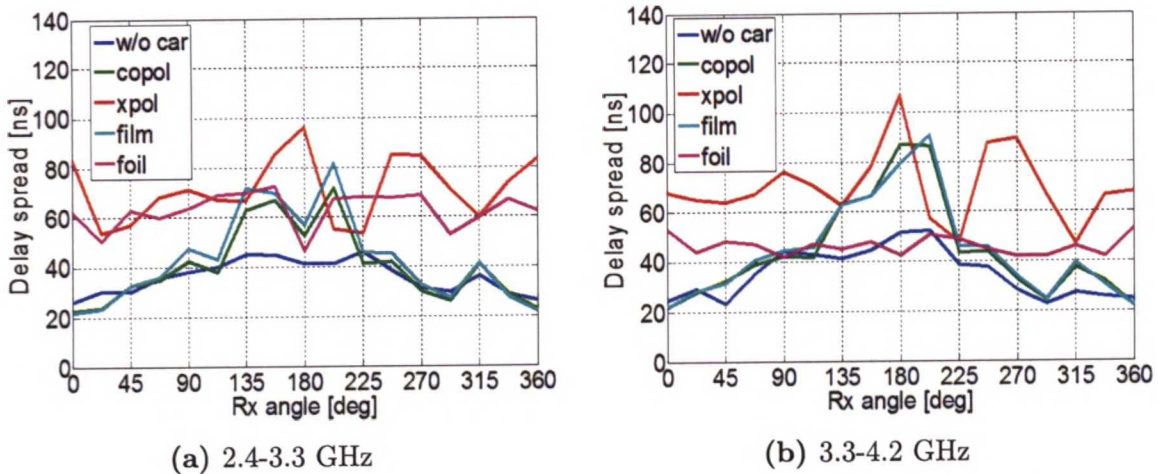


Figure 5.30 RMS delay spread in frequency sub-bands III & IV

In contrast, the DS with the Aluminium foil at the three higher frequency sub-bands exhibits almost the same level as that of no coating case. This happened because of the limited dynamic range of the measurement system. After the application of Aluminium foil on the windows, the signal level reduces to -100 dB. Since DS calculation entertains the signal only above the noise level, the DS is underestimated as compared to an ideal measurement situation with an infinite signal dynamic range.

It is evident from Figures 5.29 to 5.31 that DS of the cross-polar channels for most of the cases the largest among the measured channels. As seen earlier, the PDPs of the cross-polar channels tend to have less specular peaks whereas the signal dynamic range is well above the noise level leading to DS values on average doubled compared to the co-polar channels. The LOS component is shadowed by the roof of the car when the RX is at the rear of the car due RX antenna height, while the LOS obstruction was not as severe as the rear case when the RX was at the other locations because radio waves easily penetrate into the car through side and front windows.

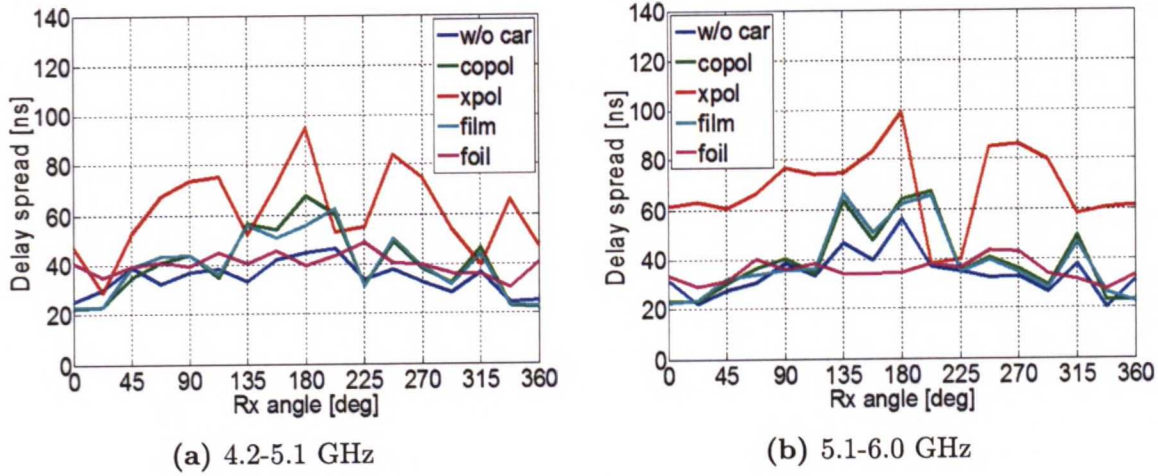


Figure 5.31 RMS delay spread in frequency sub-bands V & VI

5.2.3.5 Directional estimation: Beamforming

Beamforming is essentially a process of spatial filtering or space-time processing of data sampled at an array of sensors, and a spectral estimation technique in allowing the signal sources to be localized. An angular grid is formed corresponding to the array and subsequently an antenna beam created by the array is steered in these discrete directions to sense the maximum array output which determines the signal direction. The performance of beamforming is primarily dependent upon the physical size of the array aperture in wavelengths since the spatial discrimination improves as the aperture size increases. Beamforming has been considered under the scope of this thesis for directional estimation purpose so that specular MPCs leaving the car compartment could be identified helping in the evaluation and analysis of the directional behaviour of VPL.

From electromagnetic theory, the fundamental homogeneous wave equation with the electric field vector \mathbf{E} is given as:

$$\nabla^2 \mathbf{E} - \frac{1}{c^2} \frac{\partial^2}{\partial t^2} \mathbf{E} = 0 \quad (5.15)$$

where the constant c is the speed of light and alternatively speed of propagation of electromagnetic waves in free space given as:

$$c = \sqrt{\frac{1}{\mu_0 \epsilon_0}} = 3 \times 10^8 \text{ m/s} \quad (5.16)$$

The expression (5.15) is a vector quantity and for convenience in formulation we consider a single component of it, for instance $E(\mathbf{r}, t)$, where \mathbf{r} is the radius vector. It is interesting to note that any field of the form given by (5.17) satisfy the wave equation (5.15) provided that $|\alpha| = 1/c$.

$$E(\mathbf{r}, t) = f(t - \mathbf{r}'\alpha) \quad (5.17)$$

where \mathbf{r}' is the transpose of vector \mathbf{r} . The field expressed in (5.17) with its dependence on $(t - \mathbf{r}'\alpha)$, the solution can be interpreted as wave travelling in the direction of α (also referred as slowness vector) with the propagation speed c . In a complex notation a narrowband transmitted waveform at the origin as a reference can be expressed as:

$$E(0, t) = s(t)e^{j\omega t} \quad (5.18)$$

where $s(t)$ is a slow time varying signal as compared to the carrier $e^{j\omega t}$. For $|\mathbf{r}| \ll c/B$, where B is the bandwidth of signal $s(t)$ we can rewrite (5.18) as:

$$E(\mathbf{r}, t) = s(t)e^{j(\omega t - \mathbf{r}'\mathbf{k})} \quad (5.19)$$

where \mathbf{k} is the wave vector $k = \omega\alpha$ with magnitude $|\mathbf{k}| = \omega/c$. It can also be interpreted as $k = 2\pi/\lambda$ with λ as the wavelength.

The expression (5.19) implicitly assumes far field conditions which necessitate that the radius of propagation from the point source is large enough compared to the physical size of the array such that a flat plane of constant phase can be considered for the travelling wave, a *plane wave* referred by (5.19). An isotropic (radiating in all directions) point source gives rise to spherical wave whose amplitude decreases as the distance increases. Hence all points lying on the same sphere have equal phases classified as a *wavefront*. This implies that the distance between the transmitting source and the receiving antenna array determines the condition whether the specificity of the wave is to be considered.

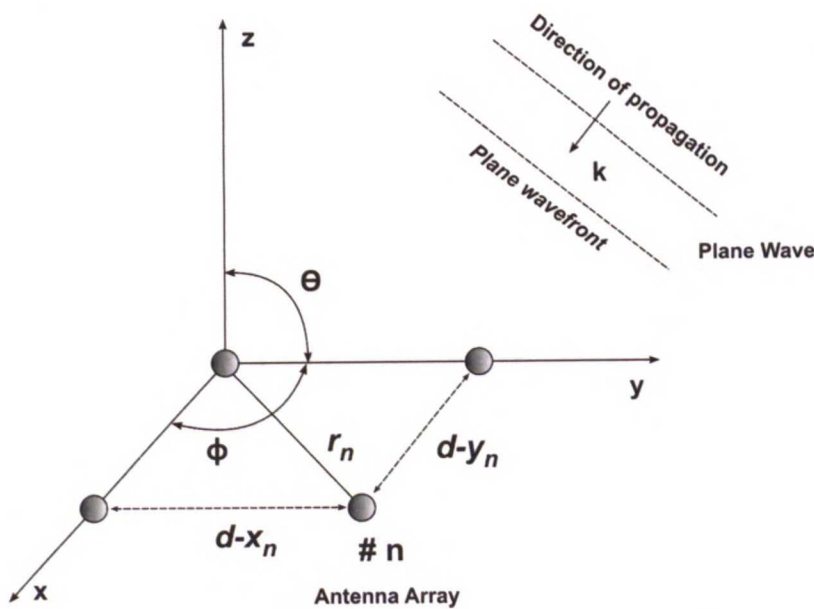


Figure 5.32 Two-dimensional planar array signal model

Considering a two-dimensional planar array depicted by Figure 5.32, an array element is considered as a point receiver in the given spatial coordinates $\mathbf{r}_n = [d -$

$x_n, d - y_n]'$. Using expression (5.19), the field received at an array element n due to a source at azimuth direction of arrival (DOA) ϕ is given as:

$$E(\mathbf{r}, t) = s(t)e^{j\omega t - jk(dx_n \cos \phi + dy_n \sin \phi)} \quad (5.20)$$

where the wave vector in a xy -plane is $\mathbf{k} = k[\cos \phi, \sin \phi]'$.

For a flat frequency response, for instance $G(\phi)$, of the array element n over the signal bandwidth, the measured output is proportional to the field at \mathbf{r}_n . For the baseband notation we can drop the term $e^{j\omega t}$ and therefore the output is given as:

$$x_n(t) = G(\phi)s(t)e^{-jk((dx_n \cos \phi + dy_n \sin \phi))} \quad (5.21)$$

The equation (5.21) essentially requires the narrowband assumption stating that the array aperture must be less than the inverse relative bandwidth (f/B).

The formulation considered so far refers to the narrow-band systems. However, for UWB systems, this can be implemented by dividing the spectrum into frequency sub-bands and use (5.21). The same approach has been considered under the scope of this thesis for performing the directional estimation which provides azimuth DOA information for the specular paths. For this purpose, the algorithm utilized process in following steps:

1. The *peak-finding* routine locate the specular peaks with corresponding delay from the PDP for the case under observation by defining a threshold using sliding window concept.
2. Based on the information obtained through step 1, the frequency domain data is filtered in delay domain after Fourier transformation according to the expression in (5.21).

The spatially filtered data contain delay τ (ns), azimuth DOA ϕ (degrees) and power (dBs) information. This data information has been exploited to build *discrete power angle delay profile* (DPADP) describing the distribution of specular and LOS paths in the environment for different measurement cases as illustrated through Figures 5.33 to 5.35.

5.2.3.6 Discrete power angle delay profile (DPADP)

The DPADPs have been constructed on polar graphs, illustrated through Figures 5.33 to 5.35 for reference, no coating, and Aluminium foil cases. The plots contain azimuth DOA ϕ (degrees) on the circumference, delay τ on the radial axis and coloured circles depicting with power normalized with respect to the dominant component, LOS. Since measurements were performed at many locations around the car, the RX positions at 0° and 90° have only been considered for illustration which provide sufficient insight to the directional characteristics of MPCs in the environment.

Reference case: Figure 5.33 shows the DPADPs for the reference measurement case in the lowest frequency sub-band when car was not included in the environment. For RX angle 0° most of the paths arrive after reflections from the front side where a half metallic wall is situated, however, for the RX angle 90° the wall on the same side of RX antenna positioning have a large window therefore the paths are received in the semicircle 0° - 90° and 0° - 360° . The DPADPs parameters for the reference case in the lowest frequency sub-band have been summarized in Table 5.3.

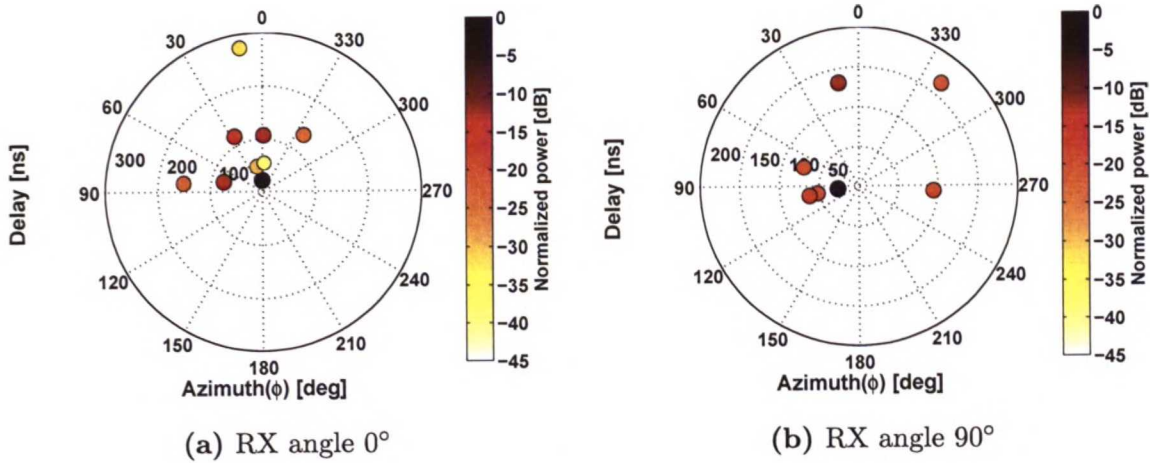


Figure 5.33 DPADPs at the lowest frequency sub-band for the reference case

Table 5.3 DPADPs parameters for the reference case

Frequency sub-band (0.6-1.5 GHz)					
RX angle 0°			RX angle 90°		
Delay [ns]	DOD [deg]	Power [dB]	Delay [ns]	DOD [deg]	Power [dB]
21.6	2	-54.31	26.5	92	-56.80
48.5	12	-84.20	52.6	100	-76.63
54.3	357	-93.78	63.3	101	-74.92
76.5	76	-69.10	73.1	71	-77.40
107.3	59	-69.24	94.2	266	-75.97
117.4	27	-71.90	132.7	11	-69.61
132.6	24	-77.30	165.6	321	-77.68
151.9	84	-77.14			
274.1	9	-87.12			

Figure 5.34 shows the DPADPs for the reference measurement case in the highest frequency sub-band. The specular paths arrive from almost all directions but compared to the low frequency DPADPs showed in Figure 5.33, the specular paths

are more attenuated and hence weak. The DPADPs parameters for the reference case in the highest frequency sub-band have been summarized in Table 5.4.

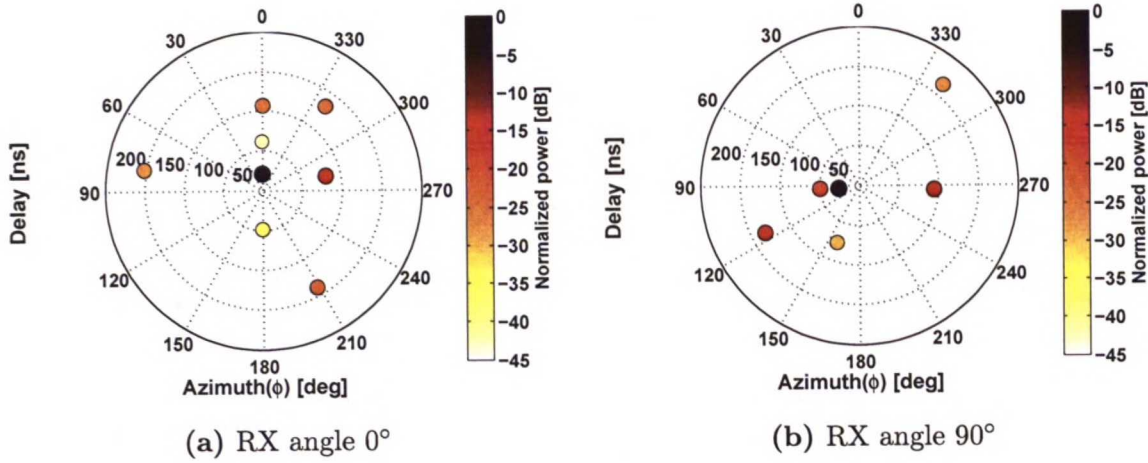


Figure 5.34 DPADPs at the highest frequency sub-band for the reference case

Table 5.4 DPADPs parameters for the reference case

Frequency sub-band (5.1-6.0 GHz)					
RX angle 0°			RX angle 90°		
Delay [ns]	DOD [deg]	Power [dB]	Delay [ns]	DOD [deg]	Power [dB]
21.3	2	-66.08	26.1	93	-67.51
48.1	179	-101.53	49.8	94	-86.15
61.4	1	-108.65	76.4	158	-96.91
81.2	283	-81.48	94.1	267	-82.10
106.9	0	-89.56	132.3	116	-82.83
131.8	323	-89.47	164.9	320	-94.83
139.7	209	-88.13			
153.2	80	-93.0			

No coating case: Figure 5.35 shows the DPADPs for the no coating measurement case with the car in the environment in the lowest frequency sub-band. If compared with the DPADPs of the reference case, it is evident that specular paths have been reduced after the introduction of the car in the environment and the car acts like a filter for these paths. Table 5.5 summarizes the DPADPs parameter for the no coating case.

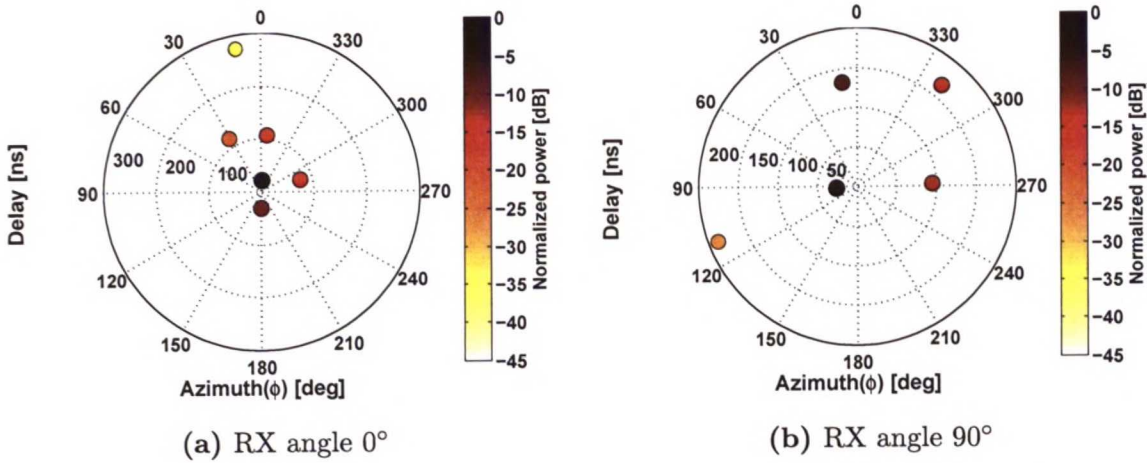


Figure 5.35 DPADPs at the lowest frequency sub-band for the no coating case

Table 5.5 DPADPs parameters for the no coating case

Frequency sub-band (0.6-1.5 GHz)					
RX angle 0°			RX angle 90°		
Delay [ns]	DOD [deg]	Power [dB]	Delay [ns]	DOD [deg]	Power [dB]
21.8	356	-56.43	26.2	94	-64.81
30.5	180	-66.84	94.8	272	-77.72
77.2	287	-72.60	132.9	8	-72.85
107.5	354	-73.83	166.4	320	-79.30
117.2	31	-77.20	188.0	111	-90.84
274	10	-89.81			

Figure 5.36 shows the DPADPs for the no coating measurement case in the highest frequency sub-band. The figure indicates the presence of even less number of specular paths as compared to the lowest frequency sub-band case. The DPADPs parameters at RX angles 0° and 90° for the no coating case have been summarized in Table 5.6.

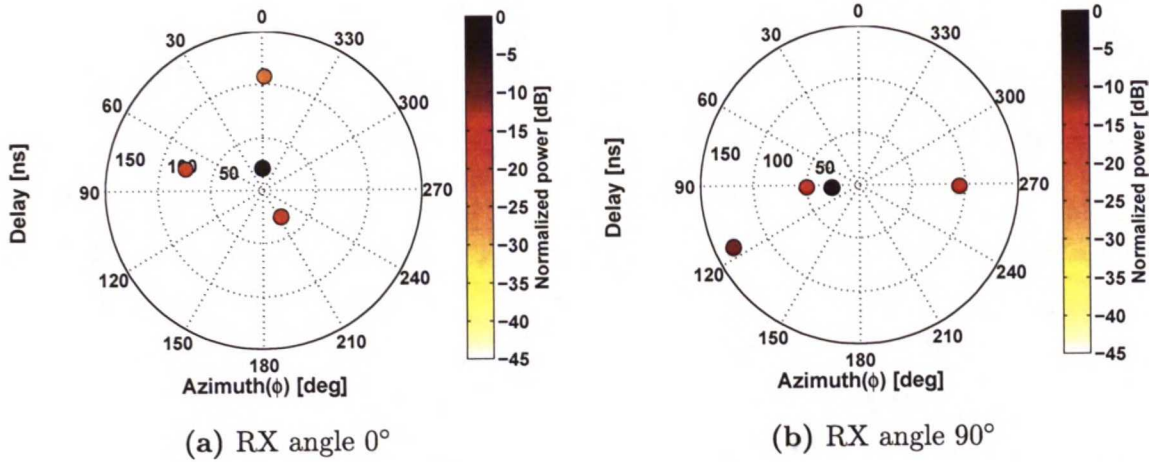


Figure 5.36 DPADPs at the highest frequency sub-band for the no coating case

Table 5.6 DPADPs parameters for the no coating case

Frequency sub-band (5.1-6.0 GHz)					
RX angle 0°			RX angle 90°		
Delay [ns]	DOD [deg]	Power [dB]	Delay [ns]	DOD [deg]	Power [dB]
21.6	1	-65.42	25.9	95	-74.09
30.3	214	-83.12	49.6	92	-90.46
76.5	74	-84.35	94.6	269	-89.08
107.5	359	-88.85	132.5	116	-84.90

Aluminium foil case: For the Aluminium foil case, the DPADPs are depicted in Figures 5.37a and 5.37b for the highest frequency sub-bands at RX angle 180°. The figures show that with the application of aluminium foil on the car windows, the specular components were blocked and only LOS component manages to reach the RX. The situation has already been discussed from the PDPs discussed in earlier sub-section 5.2.3.3. Table 5.7 summarizes the DPADPs parameters for the Aluminium foil case.

Table 5.7 DPADPs parameters for Aluminium foil case

Frequency sub-band (0.6-1.5 GHz)			Frequency sub-band (5.1-6.0 GHz)		
RX angle 180°			RX angle 180°		
Delay [ns]	DOA [deg]	Power [dB]	Delay [ns]	DOA [deg]	Power [dB]
28.6	185	-87.53	28.3	179	-94.77

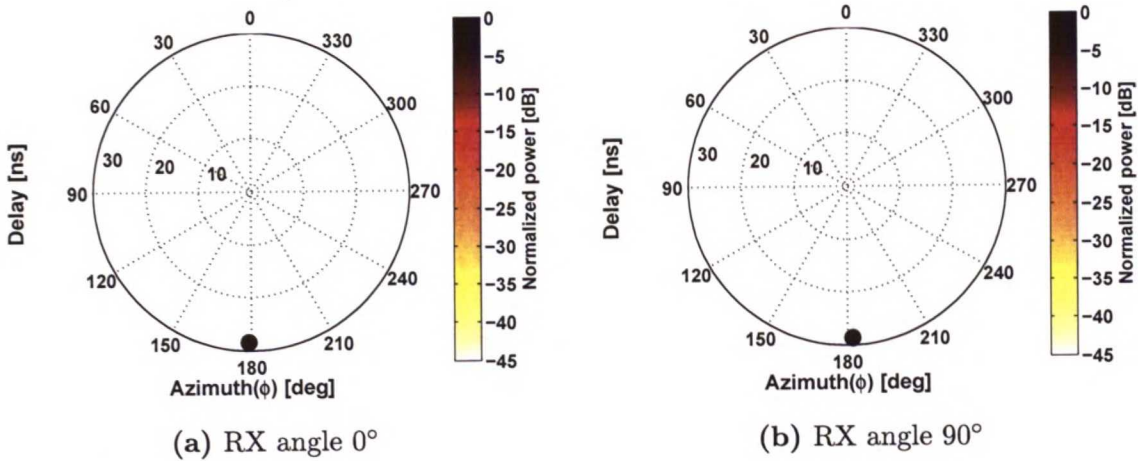


Figure 5.37 DPADPs at lowest frequency sub-band for Aluminium foil case

5.2.3.7 Geometry based path identification

In order to obtain clearer picture for detected MPCs with respect to the physical environment, a geometry based path identification analysis is presented for the reference and no coating case at RX angle 90° as illustrated in Figures 5.38 and 5.39. The path details are summarized in Table 5.8 and 5.9 respectively for the two cases under consideration. The specular paths have been drawn and scaled on the illustration according to the path length corresponding to its respective delay. In Figure 5.38 we see the direct path (LOS component) between TX and RX, two specular paths arriving after reflection from the lateral walls (wall#1 and wall#3) of the hall, a double bounced component arriving after getting reflected from the corner of wall#1 and wall#2 and the path arriving from the rear of the hall after reflection from the metal chassis of a parked vehicle around. However, another component with relatively high power is present and seems to arrive at 116° and delay of 132 ns but could not be identified and may be regarded as an artefact. In a similar fashion, the Figure 5.39 shows only the paths arriving after reflection from lateral walls where the artefact is still observable at 116°.

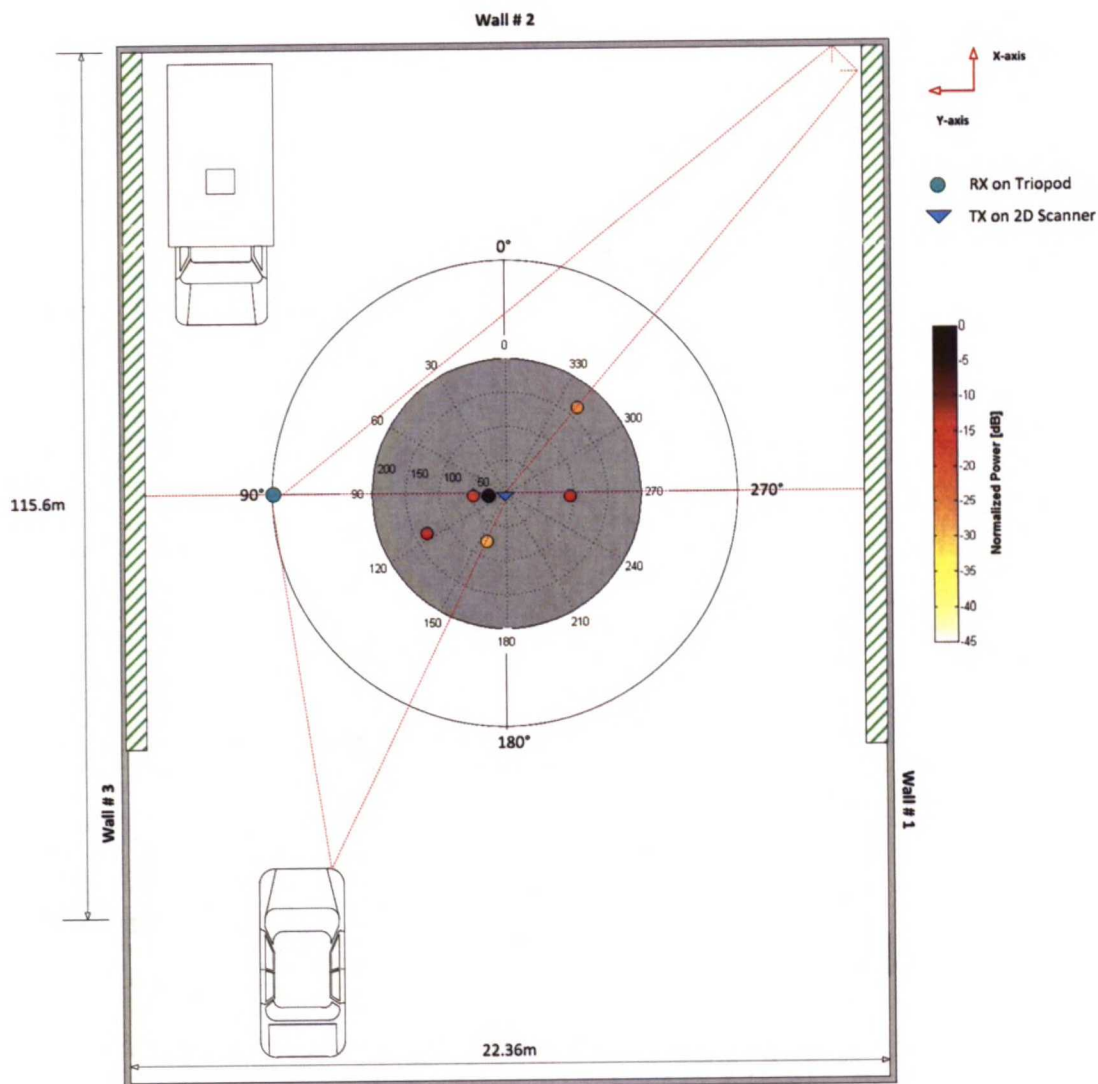


Figure 5.38 Path identification for the reference case at RX angle 90°

Table 5.8 Path identification for the reference case

MPC #	Identified path	Delay [ns]	DOD [deg]	Normalized power [dB]
1	LOS component	26.1	93	0
2	wall#3	49.8	94	-18.64
3	from vehicle at rear	76.4	158	-96.91
4	wall#3	94.1	267	-14.59
5	unresolvable	132.3	116	-15.32
6	double bounce (wall#2 and wall)#2	164.47	320	-94.83

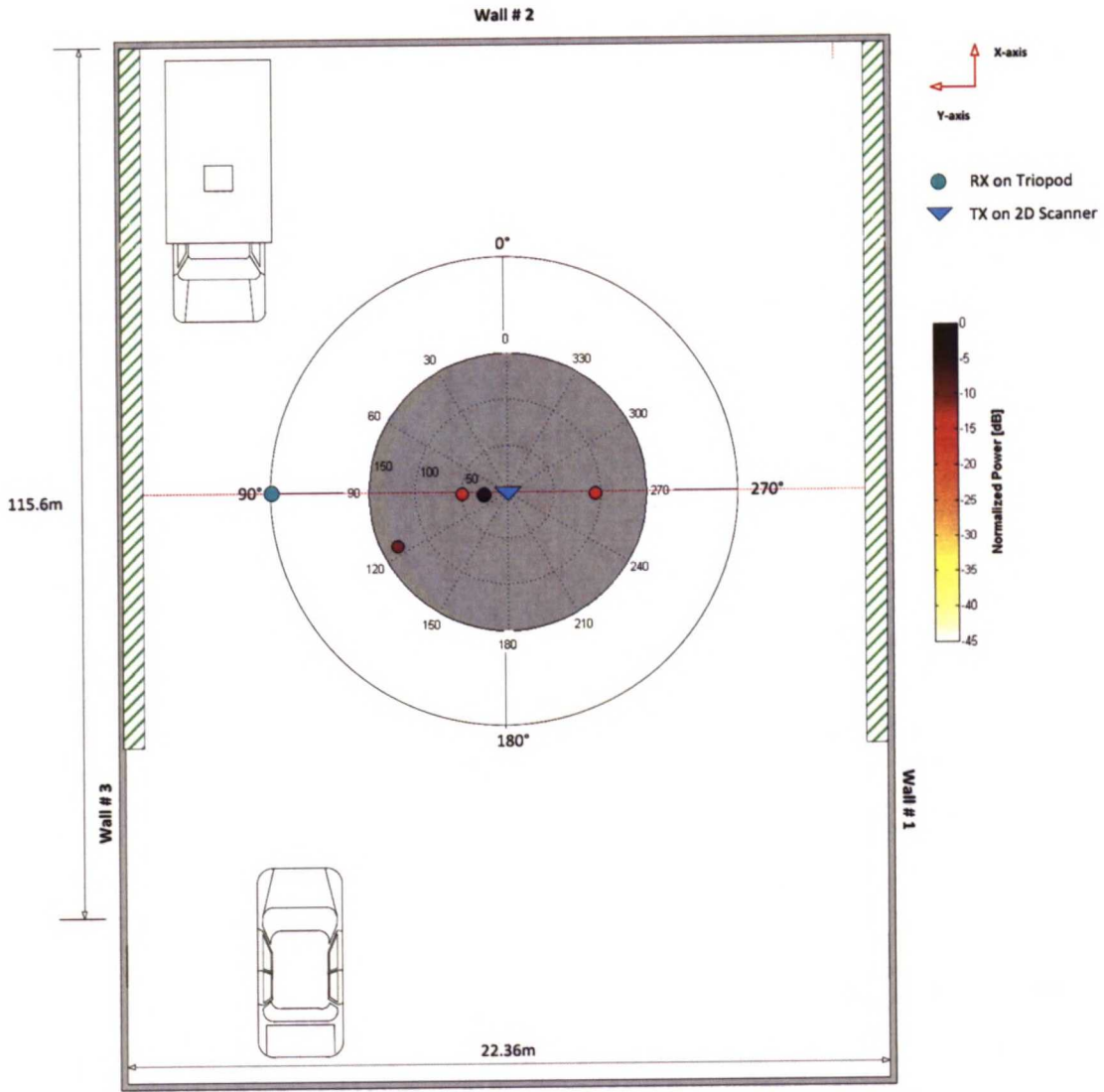


Figure 5.39 Path identification for the no coating case at RX angle 90°

Table 5.9 Path identification for the no coating case

MPC #	Identified path	Delay [ns]	DOD [deg]	Normalized power [dB]
1	LOS component	25.9	95	0
2	wall#3	49.6	92	-16.37
3	wall#1	94.6	269	-14.99
4	unresolvable	132.5	116	-10.80

5.3 UWB window film measurements

For the evaluation of window film penetration loss (WFPL), UWB measurements were performed for commercially available window films in both automotive and building series. The measurements have been described in detail in Chapter 4. The measurement data obtained corresponding to each film was post-processed using Matlab and the results are presented in this section.

5.3.1 Post-processing flow diagram

Figure 5.1 presents the post-processing flow diagram of UWB window film measurements. The measurement data retrieved from VNA in the form of forward scattering parameter $S_{21}(f)$ for individual measurements undergoes system calibration by applying corresponding calibration data which serves as a reference for the elimination of other effects than the radio channel. The second common post-processing step involved was the windowing of frequency domain data for reducing the sidelobe level and improving the dynamic range. After these two common post-processing steps, the radio channel path loss or in this case the WFPL and channel impulse response (CIR) were extracted and explained in the proceeding subsections. However, for deriving CIR, IFFT was used first for transforming frequency domain data into time domain. The three main post-processing steps including calibration, windowing, and Fourier transformation employed for these measurements are the same as that of the UWB car measurement.

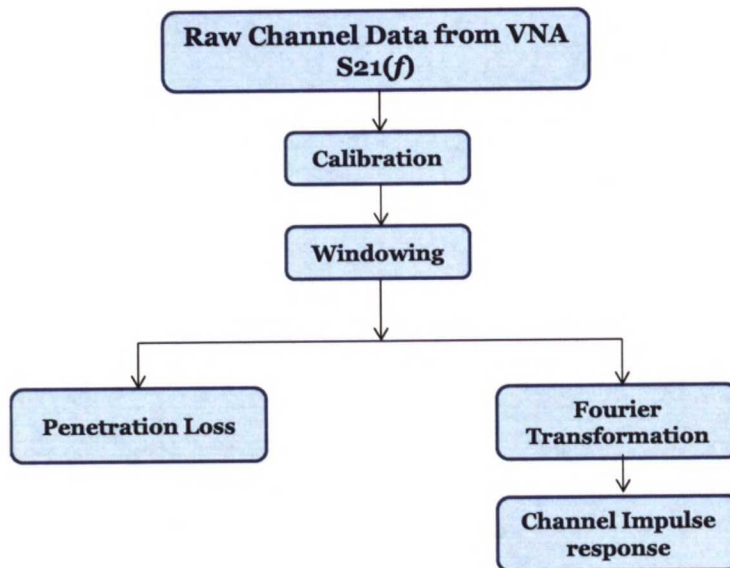


Figure 5.40 Post-processing flow diagram for UWB window film measurements

5.3.2 Channel characteristics

The main objective behind conducting window film measurement was to quantify WFPL. The measurements were performed for two different window films commercially available in the market. These include PerformX-Slate-50 that belongs to the automotive series and Century-Nova-50 which belongs to building series. The measurement scenario has been covered comprehensively in Chapter 4. The subsequent subsections present and discuss WFPL and CIR for both window films.

5.3.2.1 Window film penetration loss (WFPL)

The channel transfer function (CTF) for the individual measurements were processed with calibration and windowing as an initial step. Next, in order to mitigate the small-scale variations, frequency dependent window film penetration loss (WFPL) was extracted by first taking sliding mean over CTF using an appropriate sliding window. Then, the resultant smoothed CTF with the film was subtracted from similarly treated reference case without the film. The WFPL for the two window films are shown in Figure 5.41 and 5.42 respectively. The WFPL for PerformX-Slate-50 is on average 5 dB for the complete measurement frequency band whereas Century-Nova-50 shows on average 30 dB penetration loss.

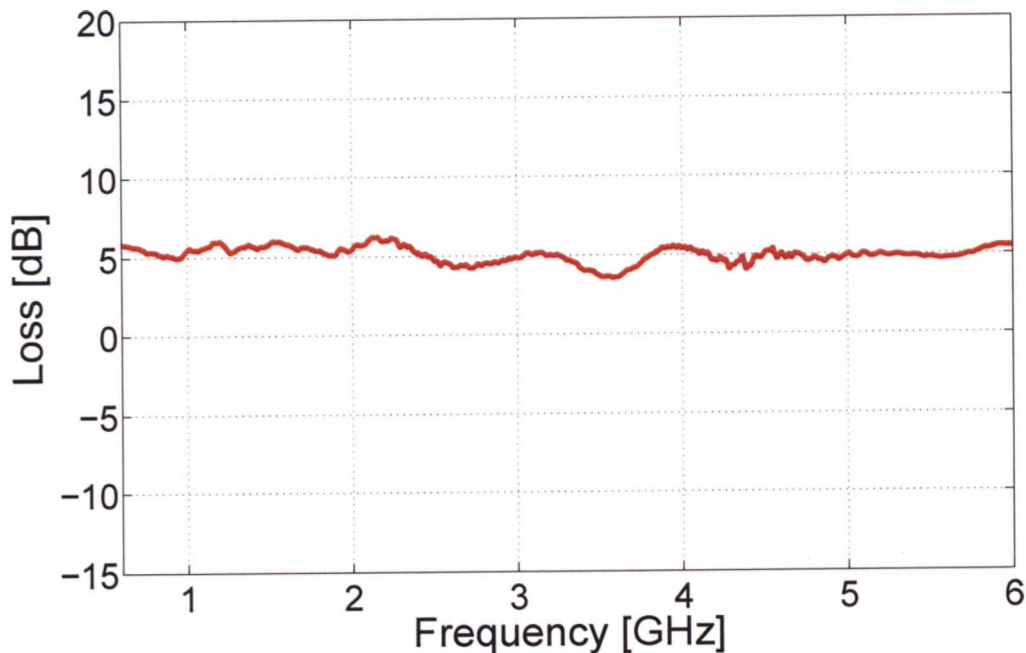


Figure 5.41 WFPL for PerformX-Slate-50

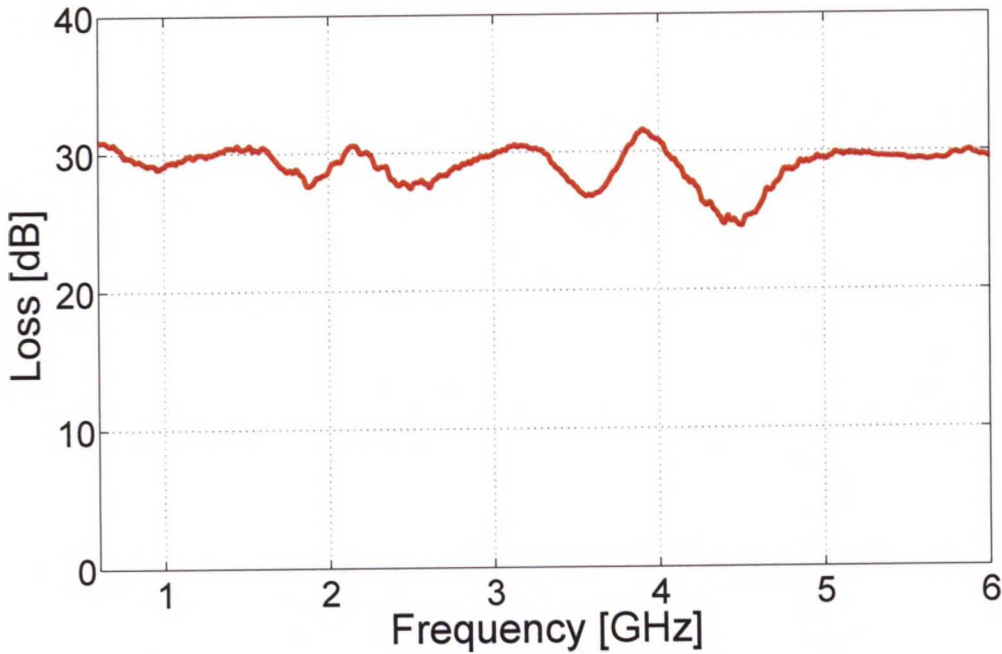


Figure 5.42 WFPL for Century-Nova-50

5.3.2.2 Channel impulse response (CIR)

The CIRs for both window films were evaluated by taking IFFT of the CTFs. The Figures 5.43 and 5.44 illustrate CIRs for PerformX-Slate-50 and Century-Nova-50 respectively plotted with respect to the reference measurement case without film between TX and RX. Figure 5.43 indicates that the CIR for both PXSlate and the reference case follow each other and almost all components in the CIR for PXSlate are attenuated on average by 5 dB with respect to the reference measurement by delay of 150 ns at which the CIR decays completely and reaches the noise floor at -125 dB. In Figure 5.44 the signal components in the CIR for Century-Nova are attenuated by 30 dB with respect to the reference. The CIR for Century-Nova decays completely and reaches the noise floor at -125 dB before the delay of 70 ns and within the delay range of 70-150 ns the MPCs completely disappears compared to the reference case and levels with the noise floor. The metallized effect of Century-Nova is clearly indicated and suggests that the use of such window films severely attenuate the signals resulting in poor coverage of radio signals in the interiors.

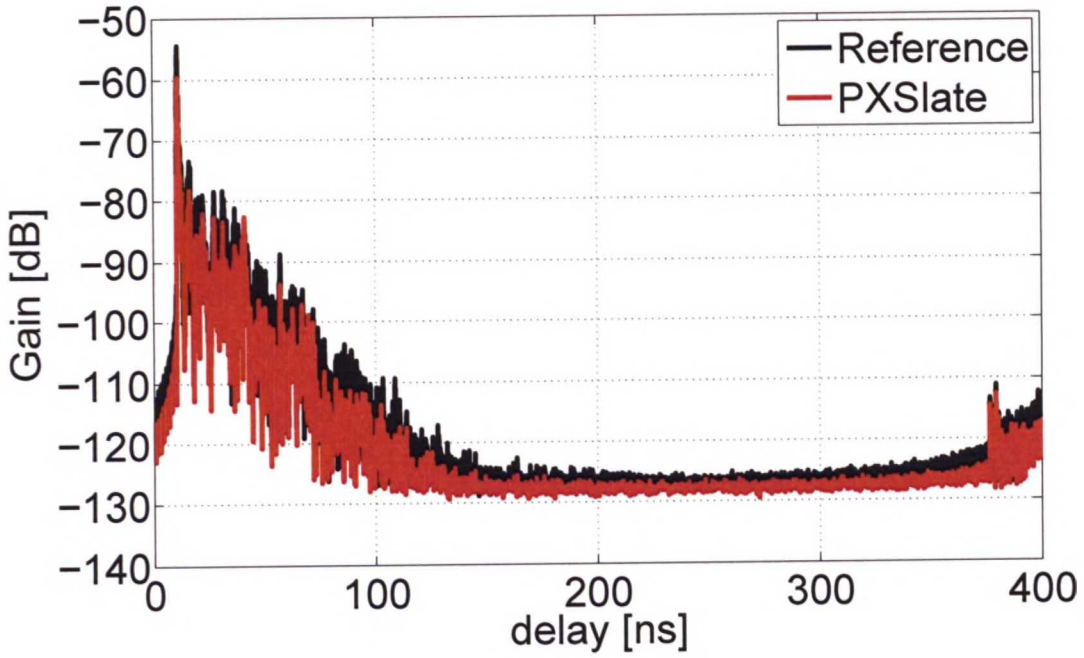


Figure 5.43 CIR for Perform-XSlate-50

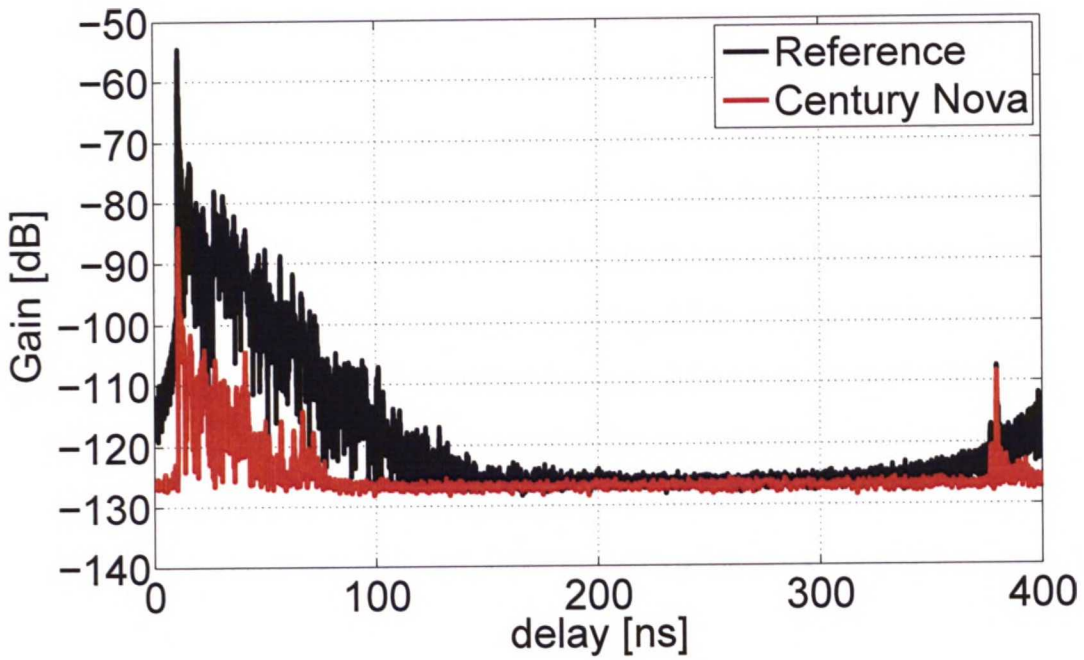


Figure 5.44 CIR for Century-Nova-50

5.4 Summary

In this chapter, data post-processing of the measurement data for UWB car measurements along with the analysis of VPL and other channel characteristics have been covered mainly. The analysis has been carried out maintaining the same sequence as that of measurements discussed in Chapter 4. The Chapter is broadly structured into two main section, (i) UWB car measurements analysis and (ii) UWB window film measurements analysis. For both of these categories, post-processing steps have been explained initially followed by a comprehensive discussion on channel characteristics including VPL, CIR, PDPs, DS and directional estimation.

Chapter 6

Numerical analysis

6.1 Introduction

The ability of predicting radio propagation channel behaviour for wireless communication systems is crucial and plays a vital role in wireless system design. Although measurements provide a considerably accurate estimate of propagation channel characteristics, they require sufficient financial resources, hardware implementation and man power. The numerical approach, however, appears to be a suitable, low cost and convenient alternative.

Nowadays, numerous design and optimization tools are being used in the wireless communication industry based on empirical and semi-empirical models for quick implementation requirements. These models do not sustain precision in complex environments such as indoor scenarios that are overwhelmed with objects demanding a contingent geometrical description. For handling such cases deterministic models tend to have a capacity to accommodate the geometry of the environment and the propagation phenomenon such as reflections, diffractions and scattering. Ray tracing is an example of deterministic approach based on Geometrical Optics (GO) and yield a good approximation of propagation phenomenon. On the other hand, numerical electromagnetics based on Maxwell's equations is the only known method that provides the most accurate description of electromagnetic wave propagation.

Various numerical techniques have been employed for last couple of decades in order to model the behaviour electromagnetic waves. With the advancement in high level programming languages and computing technologies, frequency domain solutions gained marked interest by research community. However, the frequency domain techniques suffer from several limitations and tradeoffs such as inability to deal with electrically large structures, complex shapes, and incorporation of non-linearities of materials in the design. Alternatively, Finite-difference time-domain (FDTD) techniques has been accredited as one of the most attractive methods for full wave electromagnetic analysis due to its simplicity with robust and accurate description of electromagnetic fields. For these qualities, FDTD based numerical analysis has been performed for investigating the VPL under the scope of this thesis. This chapter presents numerical characterization of VPL by first introducing the tools and methods utilized followed by numerical simulation details.

6.2 Finite-difference time-domain (FDTD) method

The Finite-difference time domain (FDTD) is essentially a grid based time domain numerical technique for computational electromagnetic modelling by solving Maxwell's curl equations directly in the time domain on a space grid. It was originally proposed by Kane Yee in the year 1966 but the formal acronym FDTD was coined by Allen Taflove in 1980 who first validated sinusoidal steady state FDTD model. Much more work have been emerged in this demesne in the succeeding years to benefit from the versatility of the FDTD method.

6.2.1 Formulation of FDTD algorithm

The electric and magnetic fields being vector quantities can be described through vectors, $\mathbf{E} = [E_x, E_y, E_z]$ and $\mathbf{H} = [H_x, H_y, H_z]$ respectively in a three dimensional Cartesian coordinate space. The use of both \mathbf{E} and \mathbf{H} information makes the solution more vigorous and hence the material properties can be modelled in rather a straightforward manner. The 3D Yee cell is illustrated in Figure 6.1 with \mathbf{E} and \mathbf{H} -field components distributed on the grid.

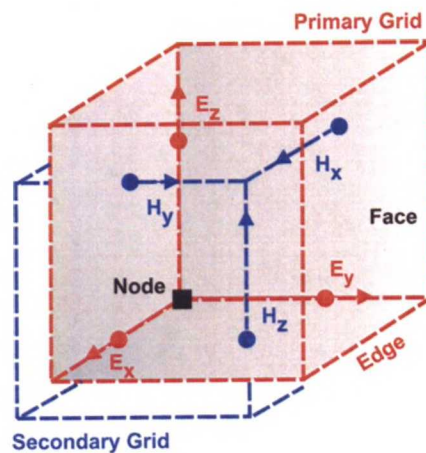


Figure 6.1 3D Yee grid with E and H-field components

The \mathbf{E} and \mathbf{H} fields are updated in a leap-frog manner using time dependent partial differential Maxwell's curl equations which are discretized using second order finite-difference approximation both in time and space in an equidistantly spaced mesh. The procedure is repeated all over again until a steady state electromagnetic behaviour is evolved. The leap-frog stepping is explicit and avoids the situations which usually faced in simultaneous equations and matrix inversions. With the prior knowledge of initial field, boundary and source conditions, the transient field can be evaluated. The well known Maxwell's curl equations are given as:

$$\nabla \times \mathbf{H} = \frac{\partial}{\partial t} \epsilon \mathbf{E} + \sigma \mathbf{E} \quad (6.1)$$

$$\nabla \times \mathbf{E} = \frac{\partial}{\partial t} \mu \mathbf{H} + \sigma_H \mathbf{H} \quad (6.2)$$

where σ and σ_H represents the electric and magnetic losses for the fields on the allocated space grid at certain instant of time. The first partial space and time derivative of an arbitrary function yields the following finite difference form :

$$\frac{\partial F(i, j, k, n)}{\partial x} = \frac{F^n(i + 1/2, j, k) - F^n(i - 1/2, j, k)}{\Delta x} + O[(\Delta x)^2] \quad (6.3)$$

$$\frac{\partial F(i, j, k, n)}{\partial t} = \frac{F^n(i + 1/2, j, k) - F^n(i + 1/2, j, k)}{\Delta t} + O[(\Delta t)^2] \quad (6.4)$$

where F^n can be either \mathbf{E} or \mathbf{H} -field at any time instant $n \cdot \Delta t$, the i, k, j being the indices of the spatial grid and $O[(\Delta x)^2]$ and $O[(\Delta t)^2]$ are the associated error quantities. By applying the central difference to the Maxwell's curl equations in (6.1) and (6.2), the x-component of, for instance \mathbf{E} -field, E_x is given as:

$$\begin{aligned} \frac{E_x|_{i,j,k}^{n+1} - E_x|_{i,j,k}^n}{\Delta t} &= \frac{1}{\epsilon_{i,j,k}} \left(\frac{H_z|_{i,j+1/2,k}^{n+1/2} - H_z|_{i,j-1/2,k}^{n+1/2}}{\Delta y} \right) \\ &- \frac{1}{\epsilon_{i,j,k}} \left(\frac{H_z|_{i,j+1/2,k}^{n+1/2} - H_z|_{i,j-1/2,k}^{n+1/2}}{\Delta z} \right) \\ &- \frac{1}{\epsilon_{i,j,k}} \left(\sigma_{i,j,k} E_x|_{i,j,k}^{n+1/2} \right) \end{aligned} \quad (6.5)$$

In the above expression (6.5), all the field quantities are solved at the time step n including the electric field E_x with the material conductivity σ . The electric field E_x values at the time step $n - 1/2$ are only stored in the computer's memory, whereas the E_x values at the time step n are not stored and must be approximated. For this purpose, a semi-implicit approximation, given by (6.6), properly estimates the terms which are not stored in the memory.

$$E_x|_{i,j,k}^{n+1/2} = \frac{E_x|_{i,j,k}^{n+1} - E_x|_{i,j,k}^n}{2}, \quad (6.6)$$

The E_x values in (6.6) at the time step n are simply assumed to be the arithmetic mean of the stored values at the time step $n - 1/2$ and the E_x values to be computed at the time step $n + 1/2$. By substituting (6.6) into (6.5), the expression is solved to the component E_x^{n+1} as:

$$\begin{aligned}
E_x|_{i,j,k}^{n+1} = & E_x|_{i,j,k}^n \left(\frac{1 - \frac{\Delta t \sigma_{i,j,k}}{2\epsilon_{i,j,k}}}{1 + \frac{\Delta t \sigma_{i,j,k}}{2\epsilon_{i,j,k}}} \right) \\
& + \left(\frac{1 - \frac{\Delta t}{\epsilon_{i,j,k}}}{1 + \frac{\Delta t \sigma_{i,j,k}}{\epsilon_{i,j,k}}} \right) \left(\frac{H_z|_{i,j+1/2,k}^{n+1/2} - H_z|_{i,j-1/2,k}^{n+1/2}}{\Delta y} \right) \\
& - \left(\frac{1 - \frac{\Delta t}{\epsilon_{i,j,k}}}{1 + \frac{\Delta t \sigma_{i,j,k}}{\epsilon_{i,j,k}}} \right) \left(\frac{H_z|_{i,j+1/2,k}^{n+1/2} - H_z|_{i,j-1/2,k}^{n+1/2}}{\Delta z} \right)
\end{aligned} \tag{6.7}$$

In a similar fashion, the other six field components can be evaluated by discretizing Maxwell's equations in respective directions. For the complete derivation of all field components, [36] is suggested.

6.2.2 Computational load

The explicit nature of the FDTD algorithm indicates its computational efficiency. For an orthogonal grid of dimensions $N_x \times N_y \times N_z$ necessitates $N = 6(N_x \cdot N_y \cdot N_z)$ degree of freedom to represent the field vectors in a three dimensional space. The total memory required to store the field and perform coefficient update increases as $O(N)$. The number of floating point iterations also increase as $O(N)$ whereas the total number of time iterations approximately increases as $O(N^{1/3})$. Hence, the number of floating point iterations of FDTD algorithm increases as $O(N^{4/3})$. In a nutshell, the factors that influence the computational load are given as:

- **Number of volumetric grid cells, N :** The six electromagnetic field components at each grid cell must be updated with every time step yielding a total scaling of $O(N)$.
- **Number of time steps, n_{\max} :** For a consistent solution in time domain, the numerical wave must propagate over time scales that adequately links each part of the structure. Therefore, n_{\max} must increase with the electrical size of the structure.
- **Accumulative errors:** The computational burden may increase due to progressive mesh refinement where phase errors can occur during the propagation of numerical modes.

6.2.3 Numerical dispersion

Normally dispersion is a word used in the meaning of widening or spreading, however, here it has a more qualified definition. In computation electromagnetics, the dispersion is referred as the variation of wavelength λ with respect to frequency f of the propagating wave or alternatively can be considered as the variation of wavenumber $k = 2\pi/\lambda$ with angular frequency $\omega = 2\pi f$. The analytical expression of the dispersion relation results from the simple scalar wave equation. A plane wave propagating in a homogeneous lossless medium along x -axis is given by following phasor form:

$$s(x, t) = e^{j(\omega t - kx)} \quad (6.8)$$

The scalar wave equation in one dimension is given as:

$$\frac{\partial^2 s}{\partial t^2} = c^2 \frac{\partial^2 s}{\partial x^2} \quad (6.9)$$

Substituting (6.8) in (6.9) yields the analytical dispersion relation as:

$$(k_x)^2 + (k_y)^2 + (k_z)^2 = \left(\frac{\omega}{c}\right)^2 \quad (6.10)$$

where ω is the angular frequency, c is the speed of light in the medium and $\mathbf{k} = [k_x, k_y, k_z]$ is the wave vector in Cartesian coordinates.

For the discrete approximation of 3D Maxwell's curl equations, the propagating wave suffers from a numerical dispersion. This implies that the numerical phase velocity of the wave propagating through the mesh may not correspond to the analytical form and rather depends on the frequency and direction of propagation. In FDTD algorithm, the numerical phase velocity generally differs from the analytical one and is usually less [36]. If the frequency is low the probability that numerical phase velocity matching the analytical one is higher. Furthermore, the phase velocity does not exhibit isotropic property and waves whose wave vector is directed along the primary axis of the grid tend to propagate faster and the lowest phase velocity is observed for the waves propagating parallel to the grid axes. The numerical dispersion relation evaluated by [36] is given as:

$$\frac{1}{(c\Delta t)^2} \sin^2\left(\frac{\omega\Delta t}{2}\right) = \frac{1}{\Delta x^2} \left(\sin^2\frac{k_x\Delta x}{2}\right) + \frac{1}{\Delta y^2} \left(\sin^2\frac{k_y\Delta y}{2}\right) + \frac{1}{\Delta z^2} \left(\sin^2\frac{k_z\Delta z}{2}\right) \quad (6.11)$$

The relation in (6.11) clearly indicates the difference with respect to the analytical form in (6.10). FDTD algorithm inherits the numerical dispersion errors which must be kept as small as possible to maintain accuracy. This can be achieved by decreasing the grid step size in (6.11).

6.2.4 Numerical stability criteria

For a stable solution of the explicit finite difference scheme, the time step for updating **E** and **H**-field components must be restricted according to the Courant-Friedrich-Levy (CFL) criteria. The CFL stability criteria for FDTD algorithm limiting the discrete time step Δt is given as:

$$\Delta t \leq \frac{1}{c \sqrt{\frac{1}{(\Delta x)^2} + \frac{1}{(\Delta y)^2} + \frac{1}{(\Delta z)^2}}} \quad (6.12)$$

where Δx , Δy and Δz are the grid space steps in a Cartesian coordinate system and c is the speed of light in the material grid cell.

The condition in (6.12) clearly indicates that the time step Δt is directly related to the grid size. The grid size has, therefore, a significant impact on the stability of a numerical simulation. By decreasing the grid size to half, the storage space requirement increases by eight times and the computational time by a factor of sixteen.

6.2.5 Strengths and weaknesses

There are several advantages that raises the interests in implementing FDTD based computational solutions. Some of these are highlighted in this subsection.

- FDTD being a time domain method, handle the impulsive behaviour in a more natural way by directly evaluating the impulse response of a system. Therefore, a single FDTD simulation can cover a wide range of frequencies when a broadband temporal waveforms, such as Gaussian pulse, are used as an excitation source.
- Since FDTD does not use linear algebra, the explicit nature of FDTD computations avoid the problems that are typically associated with the linear algebraic calculations restricting the size of frequency domain computational solutions. FDTD does not set any upper bound on the number of unknown fields to be modelled.
- FDTD is a simple method that utilizes Maxwell's equations and provides an easy and intuitive understanding of its implementation and possible outcomes of the model under study.
- FDTD being a time domain technique, evaluates the non-linear response of the system directly. The material properties can be specified at all points in the computational domain and hence the non-linear properties of the materials are treated and modelled in a straightforward manner.
- FDTD is a scheme in which **E** and **H**-field components are evolved with time, therefore, the field animation display in the model is possible which is a useful feature in understanding the behaviour of electromagnetic waves.

In reality, every modelling technique also carries some limitations. Some of these are briefly described as follows.

- FDTD is a grid based method and in order to account the complex geometrical features of the model and resolve the shortest wavelength, the grid must be discretized with sufficiently fine resolution but in doing so the computational load or burden also increases which ultimately defines a limit to the simulation of electrically large structures.
- The stability criteria, CFL, must be satisfied for realistic results while maintaining accuracy.
- Since only limited memory is available in reality, the computational domain is limited in FDTD by means of an artificial boundary which introduce errors.

6.2.6 Challenges for radio channel modelling

Although a simple technique, FDTD is subject to limitations in terms of implementation which is the major obstacle in using this powerful technique for commercial radio coverage predictions in a wideband setting. The three main challenges that are faced by FDTD applications in the field of radio propagation are described below:

- **Sufficient computational resources:** FDTD is a demanding algorithm which require high memory and intense computational requirements since the structure under observation is modelled and discretized in a grid where the vector field components are computed in a three dimensional space.
- **Validity of numerical model:** Even though FDTD provides an efficient approximation of the Maxwell's equations, the results still depend on how well a model is described. In addition, it is not always possible to take into account the exact detail of the true propagation scenario which is generally subjected to random effects such as movement of objects etc. In this view, the random effects must be removed by a useful calibration of the numerical model.
- **Numerical dispersion:** A spatially dense FDTD grid is obtained at the cost of numerical dispersion which is the variation of numerical wave vector \mathbf{k} with angular frequency ω . This relationship is different from the real world physical dispersion phenomenon which ultimately limits the accuracy of wideband simulations. For remedying this, spatially dense grids can be used which in turn increases the computational load.

6.3 Boundary conditions

Numerical representation in the computation domain is limited and inherently have a border. This border in space acts as a reflector for the propagating simulation waves which is not always desirable especially for the case of free space scenarios and becomes a source of artificial reflections in the simulation. Different types of boundary conditions are implemented based on the application under question. Some of the popular boundary conditions utilized by FDTD tools are described in this section.

6.3.1 Absorbing boundary conditions (ABC)

In a computational domain, the waves impinged on the outer boundary of the grid are reflected back unless some absorbing boundary conditions (ABC) are used. For the purpose of absorbing waves arriving at the outer boundary, the mesh must be truncated with absorbing boundary conditions (ABC) which either absorb the incoming waves without any reflection or simulate a possible analytical transparent boundary condition. The two commonly employed boundary conditions are described below.

6.3.1.1 Perfectly matched layers (PML):

PML extends the computational domain with layers of efficient numerical absorbing material which is perfectly matched to the incoming waves regardless of their polarization, frequency and angle of incidence. The waves upon encroaching PML are attenuated by its successive lossy layers. The waves reaching the last layer are reduced in amplitude by order of their magnitude and reflect backwards.

The efficiency of PML greatly depends upon its thickness, conductivity and absorbing profile. It provides absorption at all angle of incidences and its position can be controlled with respect to the structure. The parameters of the PML, such as power loss profile, conductivity and number of layers, implemented in a commercially available FDTD tools are usually user-defined and can be manipulated with a geometrical progression which has proven to be more preferable over polynomial profile.

6.3.1.2 Analytical absorbing boundary conditions (A-ABC)

In a theoretical sense, the analytical boundary condition is a non-local operator because the solution value at each point on the boundary relate to the values at all points on the boundary. Therefore, replacing a local boundary condition with analytical boundary condition is analogous to high frequency approximation. The extension of the boundary must be large as compared to the wavelength, and boundary must be set at far distance from the large objects. The efficiency of analytical boundary is quite sensitive to the angle of incidence of the incoming wave. As compared to PML, analytical boundary condition is fast and does not require the

extension of the grid. The efficiency of analytical boundary condition is approximately equal to the second order Mur/Higdon approximations [36].

6.3.2 Perfectly conductive boundary conditions

This is a natural boundary condition with a physical concept for electromagnetic waves as it completely reflects the impinging wave. In perfect conducting boundary conditions, the computational domain is terminated with a perfectly conducting planes (PEC). The tangential components of E-fields on the outer boundaries are set to zero. PEC boundary condition is often used to take the advantage of the symmetry of the object geometry for reducing the size of the computational domain.

6.3.3 Perfectly magnetic boundary conditions

This is also a natural boundary condition for electromagnetic waves but does not exist physically and is merely an artifice. In perfect magnetic boundary conditions, the computational domain is terminated with perfectly magnetic planes (PMC). The tangential component of H-field at the boundary are set to zero. Symmetry of the object geometry is also exploited by using PMC boundary conditions to reduce the size of computational domain.

6.3.4 Periodic boundary conditions

Periodic boundary conditions are utilized for the structures whose geometry shows periodic patterns. Using this boundary condition, it is necessary to simulate only a single period of the geometry in the computational domain. The geometry is subsequently mirrored at the boundary to represent infinite periodic structure.

6.4 Simulations

For the numerical investigation of VPL, simulations based on the FDTD method were performed. It has been learned from the preceding sections that presently wideband simulation for radio channel modelling is a challenge due to the requirement of intensive computational resources. For the very same reason and with the available computational hardware, harmonic simulations were carried out at some discrete frequencies. Although harmonic simulations were considered, frequencies in the complete frequency band under the scope of this thesis could not be exploited. This section comprehensively covers the FDTD simulations including the tool utilized, the model description, simulation setup and finally the simulation results.

6.4.1 Simulation tools

6.4.1.1 FDTD electromagnetic solver

SEMCAD-X v(14.6) designed by Schmid & Partner Engineering AG (SPEAG), was used as a full wave electromagnetic simulation platform for obtaining VPL at various frequencies. It is a high end, graphical user interfaced (GUI) and fully featured FDTD tool which enables the modelling of complex structures with reasonable accuracy.

6.4.1.2 Computing hardware

The computing hardware used for SEMCAD-X is briefly listed below.

- Intel Xeon R CPU 64 bit with 2.13 GHz processor and 64 GB RAM.
- NVIDIA GPU Tesla C1060 with 148 GBytes/s memory bandwidth, 6 GB dedicated memory and supporting 150 Mcells problems.

The FDTD algorithm update the information within each grid cell at every time step and does not require any additional computational flow for field updates at various locations. In this view, a parallel thread can support the calculations of the field in a single cell and all the threads follow the same flow which can be used for different cells in the computational domain. This feature allows the FDTD algorithm to be implemented with parallel computing architectures. In this perspective, the parallel hardware acceleration techniques have recently attained a great interest by FDTD research and development community. The two famous parallel hardware acceleration techniques are field-programmable gate-array (FPGA) and graphic processing units (GPUs). In comparison to FPGAs, GPUs are more affordable, accessible and can be easily integrated with personal computers. Due to these reasons, they are commonly employed nowadays for accelerating electromagnetic computations consequently decreasing the simulation times to a great extent.

6.4.2 Simulation model

The simulation model in SEMCAD-X for the evaluation of VPL constituted TX-RX antennas and Toyota Prius car. Since the accurate description of a structural model for the environment of interest is necessary to ensure sufficient accuracy in the results, therefore in order to account this, a high resolution AutoCad model of Toyota Prius 2008 model car was purchased from an online web source [3Dcadbrowser.com] with the given details. The AutoCad model of the car is depicted in Figure 6.2.

- Total number of polygons: 249352
- Total number of vertices: 131075
- Sub-objects: 42
- Materials: 20

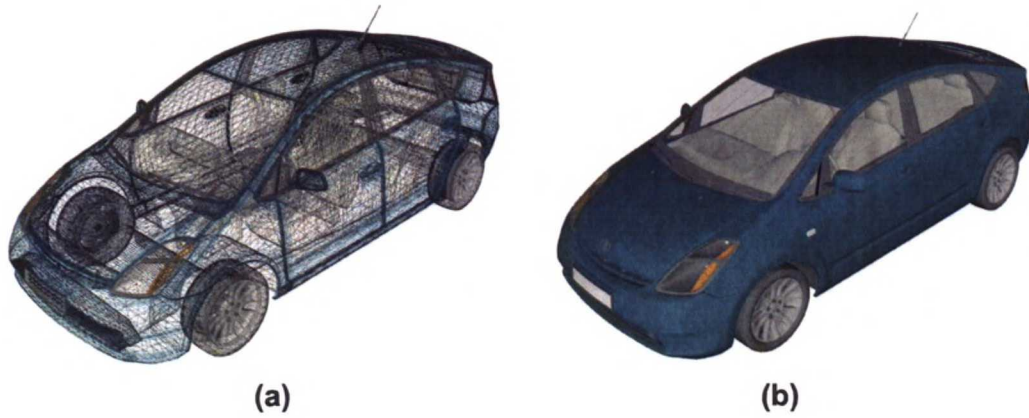


Figure 6.2 Auto-cad Toyota Prius car model (a) polygon representation (b) full model

The AutoCad model was imported in SEMCAD-X for obtaining the simulation model. The imported model merged various parts of the AutoCad model and produced overall four distinguishable parts. These individual car parts include (i) chassis (ii) interior (iii) windows and (iv) tyres. The resulted simulation model is illustrated in Figure 6.3.

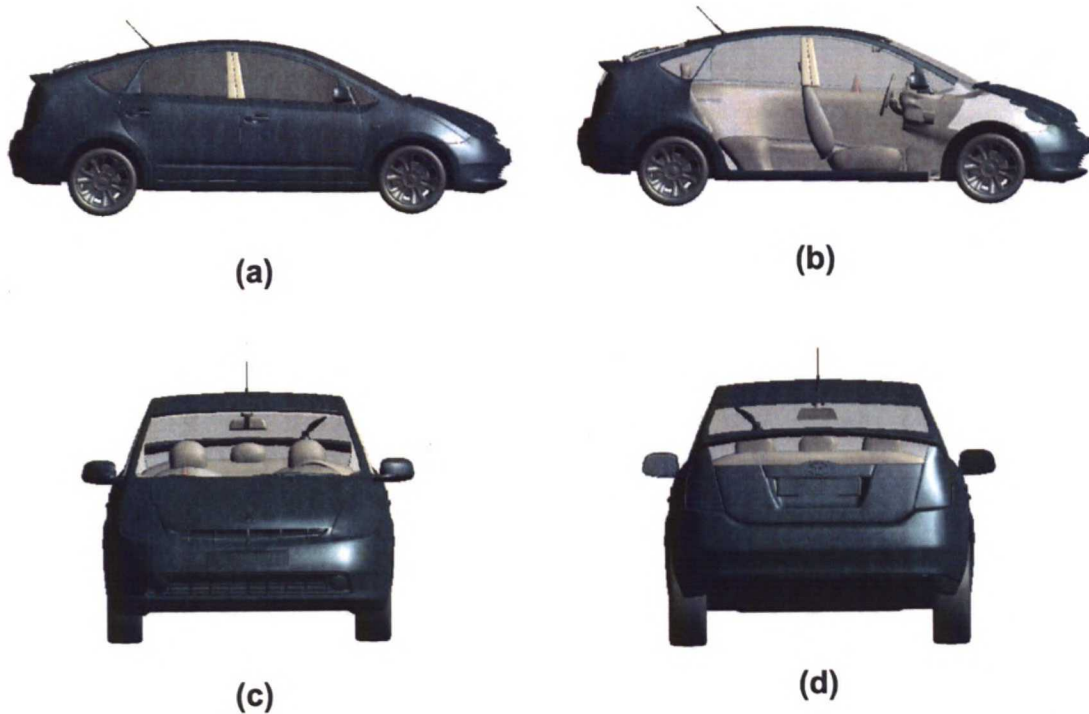


Figure 6.3 SEMCAD-X Toyota Prius car model (a) side view (b) side view with interior illustrated (c) front view (d) rear view

The TX and RX antennas were modelled as planar dipoles at respective frequency with edge excitation source which are described in the next subsection. The TX-RX antennas are illustrated in Figure 6.4.

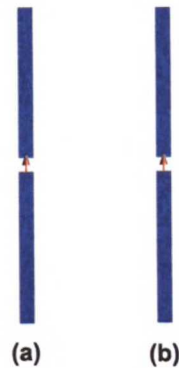


Figure 6.4 Antenna simulation model (a) TX antenna (b) RX antenna

To mimic the measurement scenario, the same settings were considered in the simulation model as that of measurements. However, it is not possible to accommodate the measurement hall with very large dimensions into the model which, if considered, could lead to a computational domain extremely large requiring super computing resources. In order to limit the computational domain, it was truncated with absorbing boundary conditions (ABC) with strict calculation mode.

The car model was centered at the zero reference in the Cartesian coordinates of the simulation model and all other positions were considered relative to it. The RX antenna outside the car was modelled at height of 2 m from reference x - y plane and at a distance of 7 m from the car FM antenna position in the same way as that of the measurements. In measurements, a galvanic connector was installed in place of car FM antenna serving the outlet for RF cable and reference for RX angular locations. For simulations only one RX position i.e. car front was considered. The simulation scenario is depicted in the Figure 6.5. The reference case which does not include the car model in the simulation is illustrated in Figure 6.6 where both TX and RX are have the same reference positions as that of the car simulation. The boundary around the models in Figures 6.5 and 6.6 is drawn to indicate the relevant dimensions and is not the actual part of simulation model.

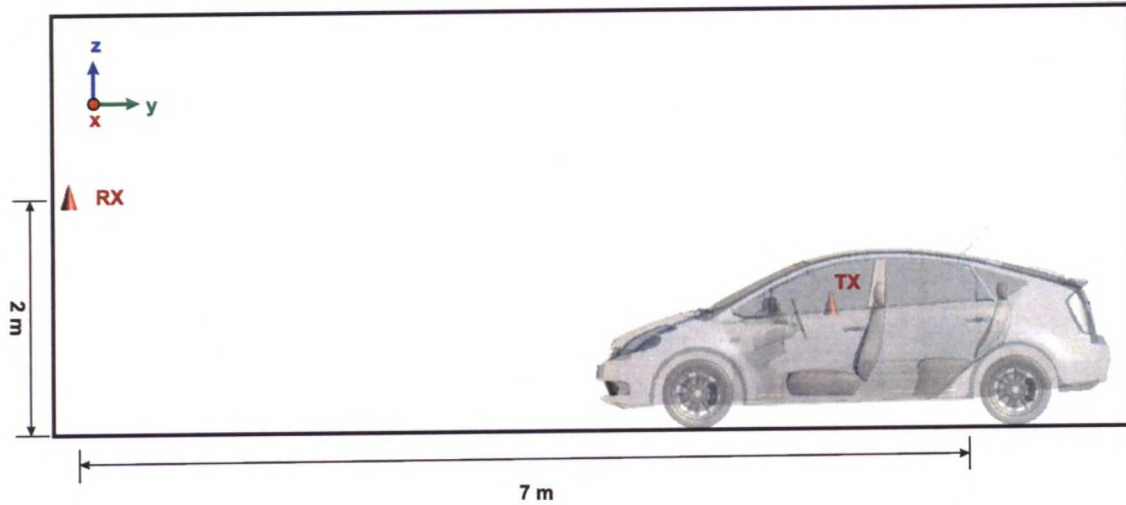


Figure 6.5 Simulation scenario with Rx outside and TX inside the car

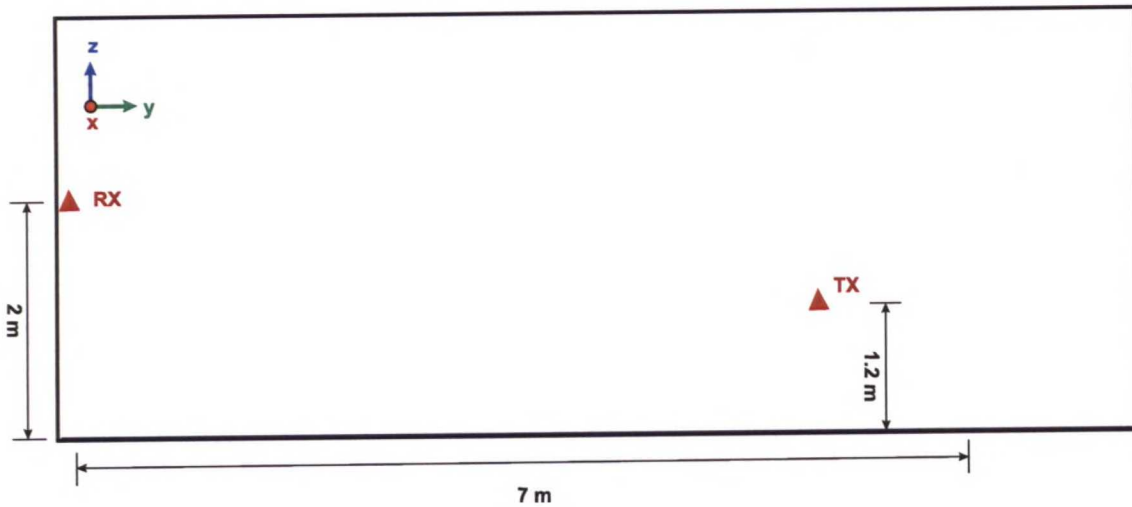


Figure 6.6 Reference simulation scenario

The TX antenna was modelled inside the car on the front passenger seat at a height of 1.2 m from the reference x - y plane defined at the bottom of the car. To eliminate the small scale effects from simulated VPL, a two dimensional TX position grid of size (5×5) with an inter element spacing of 75 mm yielding twenty-five (25) TX positions was considered similar to the measurements scenario. In the corresponding measurement, a synthetic array was achieved through the 2D electromechanical scanner installed in place of front passenger seat. The positioning of TX antenna inside the car simulation model on the front passenger seat is illustrated in Figure 6.7.

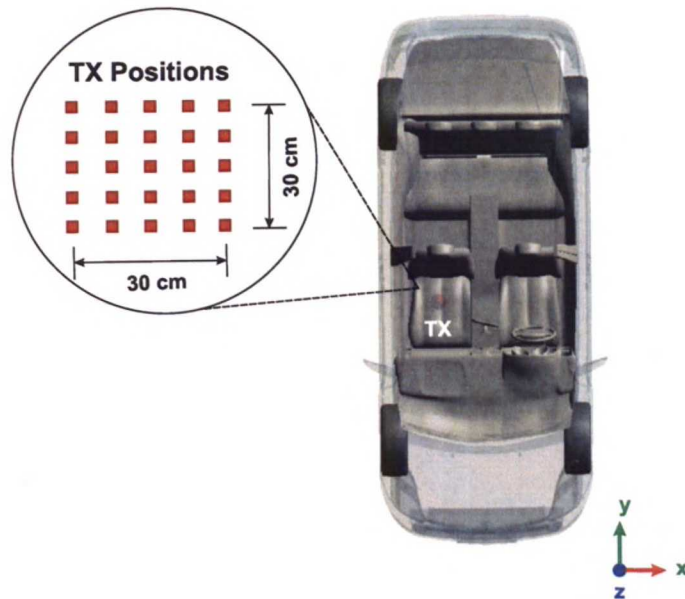


Figure 6.7 TX antenna modelling inside car

6.4.3 Simulation setup

The simulation setup for VPL simulations with different parameter settings is described in this subsection.

6.4.3.1 Material properties

In simulation model description presented in the preceding subsection, it has been mentioned that the simulation model consisted of four distinct parts which include car chassis, car interior, tyres and glass windows. For these parts material properties have been defined which are summarized in Table 6.1. For convenience, the material for the whole car interior was considered as a commercial plastic (Polypropylene) and is typically used for car dashboards and inner door coverings etc. Since tyres do not affect the inside-to-outside propagation which occurs mainly through the windows and other openings in the car chassis, they have been considered as air. For the effect of window metallization, Aluminium coating material was considered in the simulation for car windows.

Table 6.1 Material properties

S.No	Part Description	Material selection	Relative permittivity ϵ_r	Conductivity σ (S/m)
1	Car chassis	PEC	-	-
2	Car interior	Plastic (Polypropylene)	2.38	6.8×10^{-16}
3	Tyres	Dielectric	1	0
4	Windows	Glass	3.8	2.513×10^{-10}
5	Window coating	Aluminium (metal)	-	3.55×10^7
5	TX-RX antenna elements	PEC	-	-

6.4.3.2 Primary simulation settings

The main simulation parameters were setup in the primary simulation settings in SEMCAD-X. These parameters are briefly discussed below.

- **Excitation:** The type of excitation used was harmonic which utilizes a sinusoidal waveform for the excitation of the simulation at the source. The source used for exciting the TX and RX antenna was an edge source readily available in SEMCAD-X tool box. The edge source applies an electric field strength on a single edge of the primary Yee grid. It is a common choice for exciting antennas in SEMCAD-X.
- **Frequency:** The two frequencies of the source excitation sinusoidal waveform were 900 MHz and 1.2 GHz.
- **Simulation time:** It specifies the duration of the excitation waveform and was taken as 400 periods in order to account for waves propagating in the simulated computational domain.
- **Boundary conditions:** Absorbing boundary conditions were employed which maps the FDTD computational domain to infinity. The PML mode was selected for the absorbing boundary condition.
- **Grid settings and generation:** For an easy and customized generation of a FDTD grid in SEMCAD-X, an Interactive Grid Generator tool is available. Using this grid generation tool, the maximum grid step size was adjusted for a high resolution grid. To maintain numerical stability and avoid dispersion, maximum grid step size was chosen as $\lambda/14$ for discretizing background space within outer boundary of the computational domain. However, in order to obtain a more refined mesh for antenna, the step size for antenna elements

and excitation source in main grid were scaled by a factor of 0.2 with respect to the background step size. The resultant un-equidistant grids for the two simulations are given in the Table 6.2.

Table 6.2 Grid size for simulations

S.No	Simulation	Grid size (M-cells)
1	VPL simulation at 900 MHz	62.90
2	VPL simulation at 1.2 GHz	99.06

6.4.3.3 Multi-simulation setup

For the evaluation of VPL the quantity of interest is the transfer function or forward S-parameter S_{21} . For this purpose, Multi-simulation Setup tool was used which allow user to easily extract S-, Z- or Y-parameters through the Network Analysis post-processing tool. The Multi-simulation setup tool generates two child simulation setups for the main parent simulation. The ports in the parent simulation must be selected before generating child simulations. In practice, the two child simulations setups are simulated for the extraction of S-parameters. This clearly means that in order to produce S-parameter for the case under observation, two simulations are evaluated instead of a single simulation. The Network Analysis post-processing tool extracts and plots the parameters of interest.

6.4.3.4 Convergence criteria

The convergence of FDTD simulation must be taken into account to obtain correct and accurate results before the conversion of time domain data into frequency domain using Fourier transformation. The convergence requirement for a harmonic simulation is that all transients must decay and the received signal exhibit sinusoidal behaviour for steady state. If this criteria is not met, the results will be subjected to errors. For all VPL simulations, the *Monitor Signal* was observed after each simulation ended to ensure simulation convergence. The *Monitor Signal* observes the signal recorded at the sensor location to visually determine the convergence of the simulation.

6.4.4 Simulation results

6.4.4.1 Plane wave illumination

In order to analyse the behaviour of fields penetrating and propagating through the car, the car was illuminated with a plane wave excitation as depicted in Figure 6.8. In the SEMCAD-X, the method used for plane wave excitation is Total-Field

Scattered-Field (TFSF). In this method, the plane wave is propagated only in a certain bounded region in the computation domain. This bounded region, also known as total field region, encloses all scatterers in the mesh and the analytical solution of the incident plane wave is subtracted at the boundaries of total field region. The scattered field inside the total field region crosses its boundary and can propagate to the mesh truncation of the simulation model. Figure 6.8b shows the car enclosed in the total field region where the arrows indicate orthogonal vectors including magnitude of E-field, H-field and propagation vector \mathbf{k} . The car is illuminated from the front as indicated by the propagation vector \mathbf{k} . The Figure 6.8a illustrates the E-field in the x - y plane for the scattered field inside the total field region. Figure 6.9 shows the field cartography obtained from x - y plane cut at the car mid height. The field is scaled with respect to the strongest field value and is shown in the colour bar. The field scattered from the car chassis is clearly indicated whereas the intensity of the field is 5-10 dB higher inside the car. The results show that the car acts like a shielding enclosure trapping the propagating waves where they undergoes multiple bounces inside the car compartment.

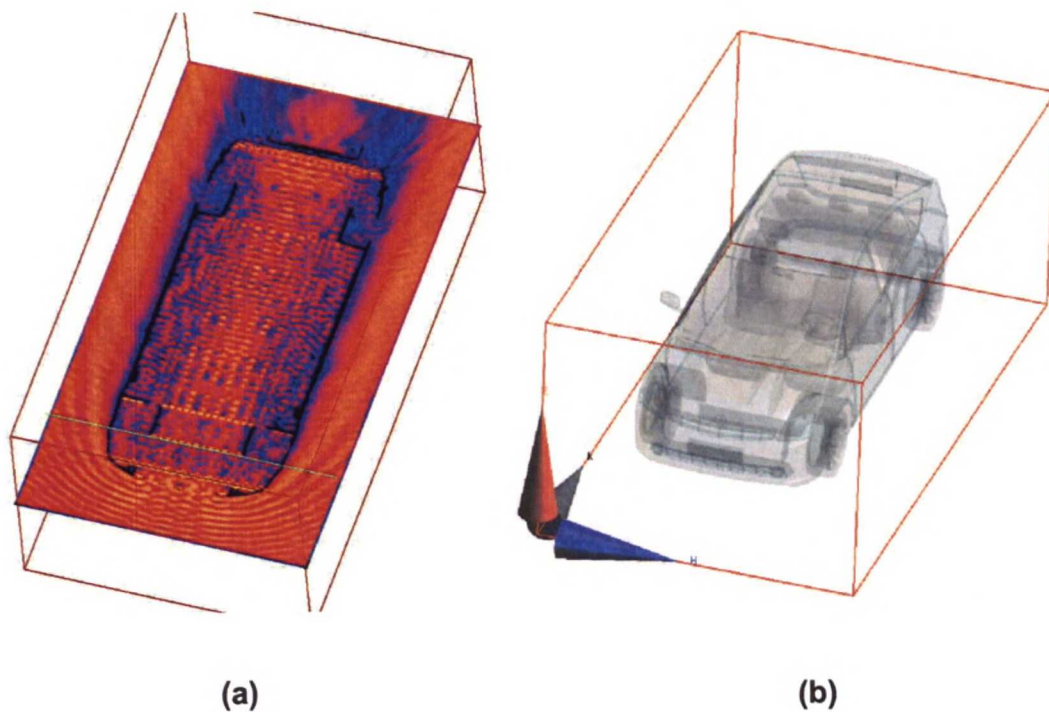


Figure 6.8 Plane wave excitation of car (a) E-field slice in x - y plane (b) total field region encapsulating car

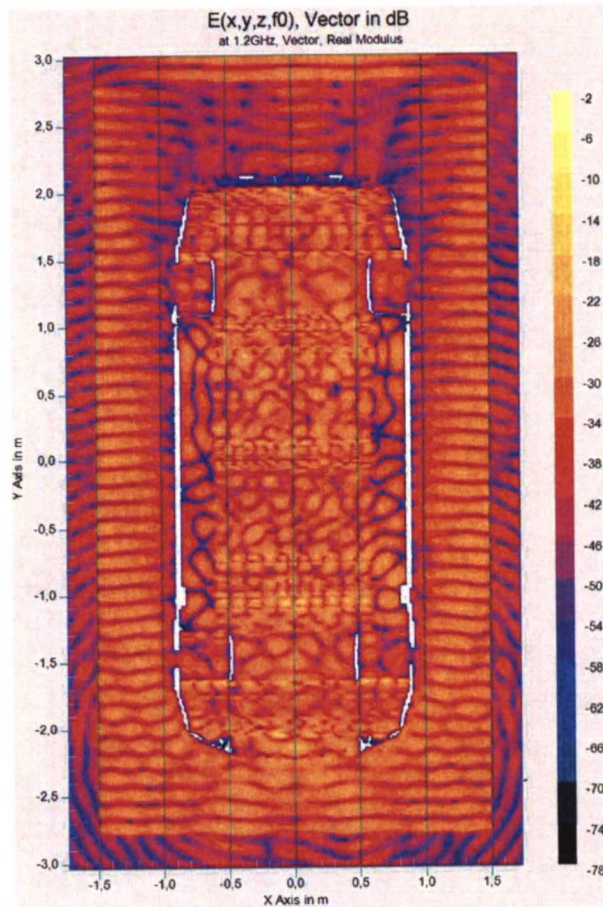


Figure 6.9 E-Field cartography for Total-Field Scattered Field simulation

6.4.4.2 VPL

The return loss of TX-RX dipole antennas modelled for VPL simulations at 900 MHz and 1.2 GHz is illustrated in Figures 6.10 and 6.11 respectively. The antennas at both frequencies have a return loss of 15 dB. For antennas at 900 MHz frequency show 6 dB bandwidth 140 MHz of whereas the antennas at 1.2 GHz frequency exhibits 6 dB bandwidth of 180 MHz.

The model scenario considered for VPL simulations has been described in the earlier section which take into account aluminium foil coating on the car windows. The forward S-parameter S_{21} or alternatively the transfer function extracted through Network Analysis tool at each frequency was linearly averaged over the spatial TX positions inside the car. This linear spatial averaging was intended to remove small scale effects from the results. The VPL values were derived by taking the difference of power magnitudes for the VPL simulation and the reference simulation at a given frequency. The reference simulation, as explained earlier, did not include the car while TX and RX positions were the same as that of the VPL simulation.

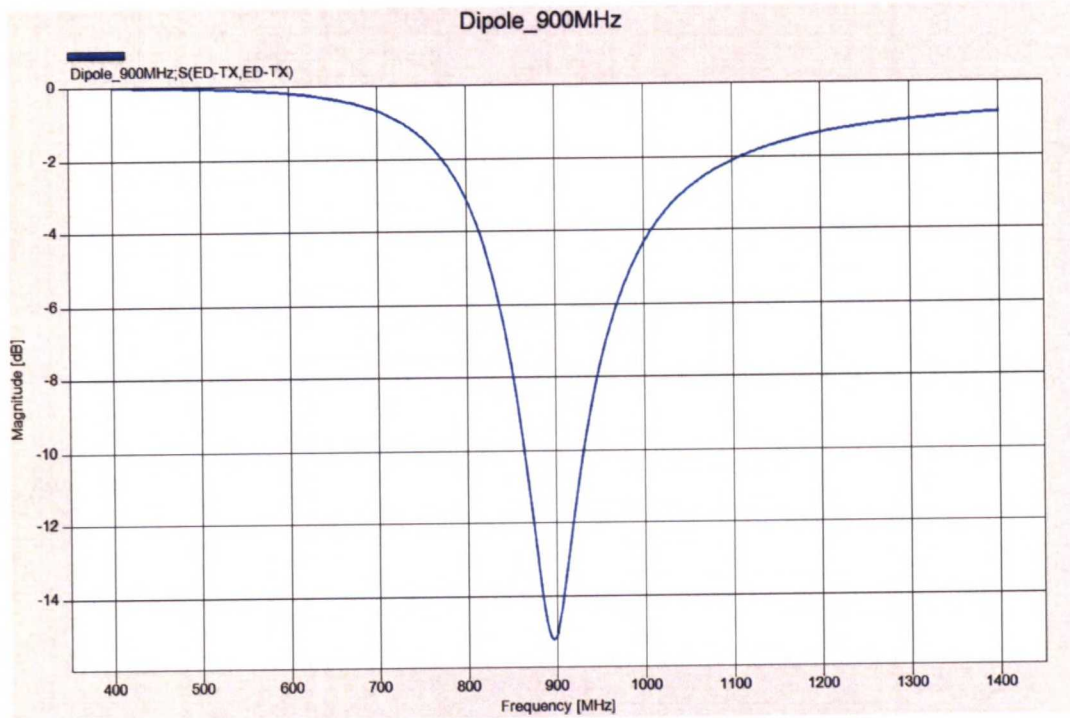


Figure 6.10 Return loss for TX-RX antennas at 900 MHz

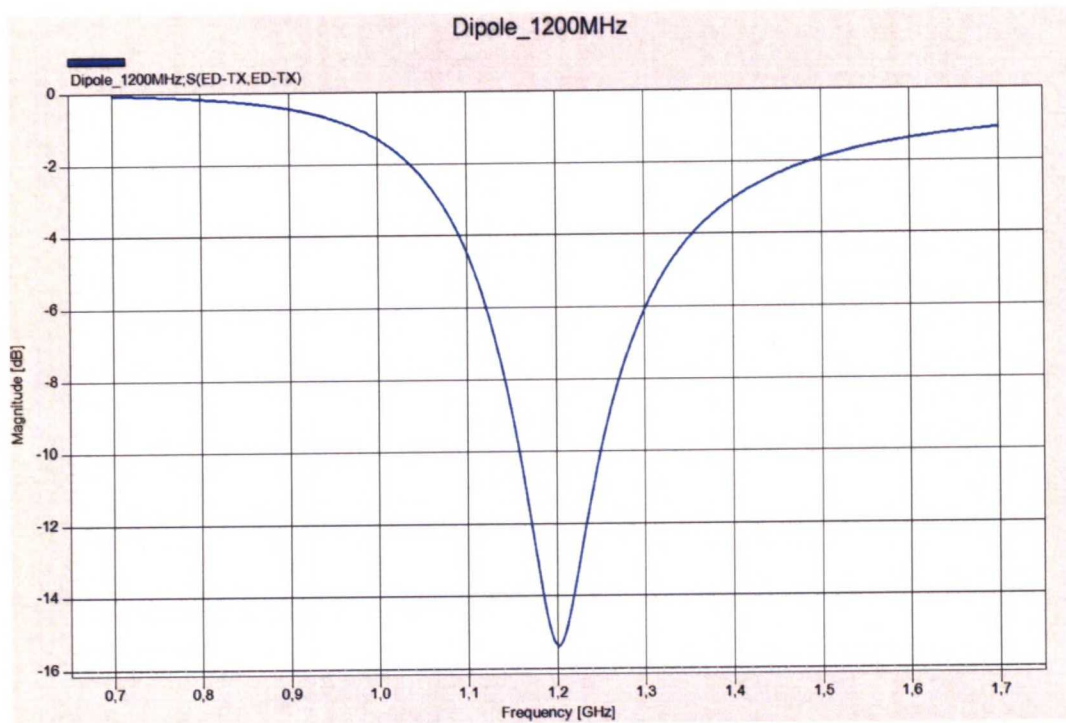


Figure 6.11 Return loss for TX-RX antennas at 1.2 GHz

The VPL values obtained at 900 MHz and 1.2 GHz are summarized in the Table 6.3 along with the total time of a simulation for single TX position inside the car.

Table 6.3 Mean simulated VPL

S.No	Frequency	Mean VPL [dB]	Single simulation time (hrs)	Total time for VPL estimate (hrs)
1	900 MHz	14	5.62	140.5
2	1.2 GHz	16.5	9.53	232.5

6.4.4.3 Simulations versus measurements

Table 6.4 presents simulated and measured mean VPL at 900 MHz and 1.2 GHz. The difference between simulated and measured mean VPL at 900 MHz frequency is 4 dB whereas at 1.2 GHz frequency the difference is 2.5 dB. The reason of this difference is two-fold: (i) it is intractable to incorporate the true material properties of all the objects in the simulation model and (ii) the accuracy of the results depends upon the description of simulation model.

Table 6.4 VPL comparison between simulations and measurements

S.No	Frequency	Mean simulated VPL [dB]	Mean measured VPL [dB]
1	900 MHz	14	18
2	1.2 GHz	16.5	18

6.5 Summary

This chapter has covered the numerical analysis of VPL. Initially the mathematical formulation of the numerical technique considered for the subject analysis is presented along with its limitations, advantages and disadvantages, and present challenges faced by the research community to employ numerical techniques for radio channel modelling. Next, the electromagnetic boundary conditions have been discussed providing a background for their implementation in simulation tools. Finally, the simulations performed for the evaluation of VPL have been described in detail by first introducing the simulation tool utilized followed by simulation model, setup and scenarios. At the end, a brief comparison between measured and simulated VPL has been drawn.

Chapter 7

Conclusions and future thoughts

This thesis work has primarily addressed the characterization of Vehicle Penetration Loss (VPL) at major wireless communication frequencies in the presence and absence of automotive window coating and based on both empirical and numerical evaluation. It has also comprehensively covered the contingent analysis of radio wave propagation into a typical car signifying the associated propagation phenomenon and influence of car structure on directional VPL. The exceptional proliferation of wireless communication and broadcast networks over recent years necessitates a reliable in-vehicle coverage from quality of service (QoS) standpoint and has been a main focus of both wireless network operators and automotive industry. In general, the automobiles are manufactured into a metallic chassis with relatively small window apertures compared to its size. Moreover, vehicle chassis appears to be a complete metallic enclosure when windows are covered with a metallized coating which affects the communication through vehicle interior. In effect, VPL is substantial and carries a superlative standing for mean received signal level inside a vehicle and fade margin calculations in wireless system design. Despite their importance in coverage predictions, VPL investigations are scarce in literature. These very facts ultimately stimulated the research study under the scope of this thesis. Therefore, this meticulous characterization of VPL will not only serve a vital role in the optimization of existing incumbent wireless services for high data rate applications but also pave a way for the deployment of in-vehicle ultra-wideband (UWB) wireless technologies with future applications such as vehicle peripheral monitoring, vehicle radar and wireless multimedia distribution inside a vehicle.

With the goal of characterizing VPL on empirical groundwork, extensive UWB car measurements were performed in an indoor environment with a wide variety of scenarios in the first step. In Chapter 4, measurement methodology and scenarios have been covered in detail for better understanding before commencing an in-depth analysis. Frequency domain measurement technique was employed for conducting all measurements since it provides high dynamic range and involves simple implementation requirements wherein the quality of the equipment was ensured to maintain accuracy in the results. In order to effectively exploit the directional behaviour of VPL, different sets of measurement scenarios were considered utilizing different window coating which include commercial automotive window film and Aluminium

metal foil. In addition to this, UWB window film measurements were also carried out in a specialized environment for the assessment of penetration loss through different commercially available and widely used window films. The compendium of these measurements enabled the analysis to single out the precise effect of window films by determining their penetration loss. One meaningful and major contribution of this research work is that it utilized commercially available window films for the first time in order to characterisation of VPL and analysed their overall effect on propagation of radio waves into a vehicle.

In Chapter 5, the statistical quantification of measurement data has been explained by first presenting the post-processing steps and methods. The post-processing methods cause a significant impact on the accuracy of results and if not considered appropriately, thereby inducing errors in the results which subsequently affects the analysis. Hence, standard and efficient data post-processing methods were employed and data was processed by segregating the complete frequency band into frequency sub-bands so that the behaviour of different channel characteristics can be analysed for various frequencies. The discussion then immersed into a comprehensive analysis of the obtained results. The directional VPL characteristics were examined in a comparative manner with and without the inclusion of window coatings. The mean VPL evaluated for no coating, window film and Aluminium metal foil case was 3 dB, 6.6 dB and 20.7 dB respectively for the complete observed frequency range. The VPL values for the no coating case in the lowest frequency sub-band are closely related to those reported in the literature which qualify the measurement results of this research work. The delay domain parameter, RMS delay spread, exhibited highest values close to 100 ns for the Aluminium metal foil and rear of the car structure manifesting the influence of car structure and metallization of car windows. Finally, the directional estimation was performed revealing the multipath propagation effects in the environment with different window coating configuration. It allowed the identification of specular paths from the environment into the car. On the basis of VPL results, it is inferred that the use of metallized window films offers adverse effects on the communication of radio signal into vehicles which subsequently impacts the overall throughput. A possible solution to avoid such situation is to workout advance methods and techniques that improve the signal quality inside vehicle in the presence of a metallized window film. Also, future research in the field of automotive window films may enable effective communication into vehicle without compromising on the heat rejection performance.

In Chapter 6, numerical analysis of VPL through FDTD simulations has been presented as alternative approach to measurements. It has been always a great attraction in the research community to utilize a numerical techniques for the solution of a scientific problem therewith reducing the experimental efforts. The numerical characterisation of VPL was achieved by using FDTD based commercially available full wave electromagnetic solver, SEMCAD-x. The choice of FDTD numerical method was made on the basis of its procreative features for electrically large problems. For enhancing accuracy in the results, a high resolution AutoCad model was used in the numerical solver. The fact that the use of numerical evaluation is limited due to computational resource requirements was established on theoretical ground

in beginning of the Chapter 6. In this perspective, the possibility of wideband simulations was fallible and therefore single frequency simulations were performed. The simulated mean VPL values at 900 MHz and 1.2 GHz were 14 dB and 16.5 dB by considering the Aluminium metal foil coating on the car windows. These values deviate from measurements in the order of 2-4 dB. A possible reason for deviation in the simulated results is because of the inaccurate description of the material properties used in car simulation model. Nevertheless, the numerical evaluation of VPL using an electromagnetic full wave solver is the very first attempt for this kind of research investigation and also a main contribution of this thesis. It has established a new starting point for research in this regard.

In general, the results of the empirical evaluation of VPL from this thesis can be used in developing guidelines and a standard framework for wireless system design and optimization. The results will also enable automobile manufacturers for deciding the most suitable antenna position inside and on vehicle chassis for various applications. The future work may evolve into the evaluation of VPL with varying degrees of detail such as different vehicle types and window coatings in different measurement environments can essentially provide a large set of results for establishing an international standard. The extension of numerical evaluation, using super computing resources, is one of the most appealing future task and can possibly eliminate the requirement of measurement approach at some point in future. The predictions are always hard but can be realizable with a systematic scientific approach and constant travail. As it has been said by the famous physicist and Nobel laureate, Neils Bohr:

Prediction is very difficult, especially about the future.
Neils Bohr (1885-1962)

References

- [1] C. Hill and T. Kneisel, "Portable radio antenna performance in the 150, 450, 800, and 900 mhz bands 'outside' and in-vehicle," *IEEE Transactions on Vehicular Technology*, vol. 40, no. 4, pp. 750–756, Nov 1991.
- [2] W. Vogel, G. Torrence, and N. Kleiner, "Measurement of propagation loss into cars on satellite paths at l-band," in *Proceedings of the Second European Workshop on Mobile/Personal Satcoms (EMPS '96)*, 1996, pp. 129–138.
- [3] I. Kostanic, C. Hall, and J. McCarthy, "Measurements of the vehicle penetration loss characteristics at 800 mhz," in *Vehicular Technology Conference*, vol. 1, May 1998, pp. 1–4.
- [4] F. Harrysson, "A simple directional path loss model for a terminal inside a car," in *Vehicular Technology Conference*, vol. 1, Oct. 2003, pp. 119–122.
- [5] F. Berens, H. Dunger, S. Czarnecki, T. Bock, R. Reuter, S. Zeisberg, J. Weber, and J. Guasch, "Uwb car attenuation measurements," in *Mobile and Wireless Communications Summit*, July 2007, pp. 1–5.
- [6] E. Tanghe, W. Joseph, L. Verloock, and L. Martens, "Evaluation of vehicle penetration loss at wireless communication frequencies," *IEEE Transactions on Vehicular Technology*, vol. 57, no. 4, pp. 2036–2041, July 2008.
- [7] F. Harrysson, T. Hult, and F. Tufvesson, "Evaluation of an outdoor-to-in-car radio channel with a four-antenna handset and a user phantom," in *Vehicular Technology Conference*, Sept. 2011, pp. 1–5.
- [8] M. Malmirchegini and Y. Mostofi, "An integrated sparsity and model-based probabilistic framework for estimating the spatial variations of communication channels," *Physical Communication*.
- [9] D. J. Vild, "Ashae research and principles of solar heat transfer through glass fenestrations," in *Windows and Glas: In the Exterior of Buildings*. Washington DC, USA: Building Research Institute, March 1957, pp. 19–28.
- [10] L. I. Gibbs, D. W. Lawrence, and M. A. Kohn, "Heat exposure in an enclosed automobile," *J La State Med Soc*, vol. 147, no. 12, pp. 545–546, Dec 1995.

- [11] A. Grundstein, V. Meentemeyer, and J. Dowd, "Maximum vehicle cabin temperatures under different meteorological conditions," *Int J Biometeorol*, vol. 53, no. 3, pp. 255–261, May 2009.
- [12] C. McLaren, J. Null, and J. Quinn, "Heat stress from enclosed vehicles: moderate ambient temperatures cause significant temperature rise in enclosed vehicles," *Pediatrics*, vol. 116, no. 1, pp. e109–112, Jul 2005.
- [13] A. Molisch, D. Cassioli, C.-C. Chong, S. Emami, A. Fort, B. Kannan, J. Karedal, J. Kunisch, H. Schantz, K. Siwiak, and M. Win, "A comprehensive standardized model for ultrawideband propagation channels," *IEEE Transactions on Antennas and Propagation*, vol. 54, no. 11, pp. 3151–3166, Nov. 2006.
- [14] H. Hashemi, "The indoor radio propagation channel," *Proceedings of the IEEE*, vol. 81, no. 7, pp. 943–968, Jul 1993.
- [15] V. Degli-Esposti, D. Guiducci, A. de'Marsi, P. Azzi, and F. Fuschini, "An advanced field prediction model including diffuse scattering," *IEEE Transactions on Antennas and Propagation*, vol. 52, no. 7, pp. 1717–1728, 2004.
- [16] A. Richter and R. S. Thoma, "Joint maximum likelihood estimation of specular paths and distributed diffuse scattering," in *Vehicular Technology Conference*, vol. 1, 2005, pp. 11–15.
- [17] T. Fugen, J. Maurer, T. Kayser, and W. Wiesbeck, "Verification of 3d ray-tracing with non-directional and directional measurements in urban macrocellular environments," in *Proc. Vehicular Technology Conference*, vol. 6, 2006, pp. 2661–2665.
- [18] A. Molisch, *Wireless Communications*. Wiley, 2005.
- [19] B. M. Donlan, D. R. McKinstry, and R. M. Buehrer, "The uwb indoor channel: large and small scale modeling," *IEEE Journal of Wireless Communications*, vol. 5, no. 10, pp. 2863–2873, 2006.
- [20] A. Alvarez, G. Valera, M. Lobeira, R. Torres, and J. Garcia, "New channel impulse response model for uwb indoor system simulations," in *Vehicular Technology Conference*, vol. 1, april 2003, pp. 1 – 5.
- [21] R. C. Qiu and I.-T. Lu, "Wideband wireless multipath channel modeling with path frequency dependence," in *Proc. Conf. on Converging Technologies for Tomorrow's Applications Communications ICC 96*, vol. 1, 1996, pp. 277–281.
- [22] R. Qiu and I.-T. Lu, "Multipath resolving with frequency dependence for wide-band wireless channel modeling," *IEEE Transactions on Vehicular Technology*, vol. 48, no. 1, pp. 273–285, Jan 1999.
- [23] S. S. Ghassemzadeh, R. Jana, C. W. Rice, W. Turin, and V. Tarokh, "Measurement and modeling of an ultra-wide bandwidth indoor channel," *IEEE Transactions on Communications*, vol. 52, no. 10, pp. 1786–1796, 2004.

- [24] D. Cassioli, M. Z. Win, and A. F. Molisch, "The ultra-wide bandwidth indoor channel: from statistical model to simulations," *IEEE Journal on Selected Areas in Communications*, vol. 20, no. 6, pp. 1247–1257, 2002.
- [25] J. Kunisch and J. Pamp, "Measurement results and modeling aspects for the uwb radio channel," in *Proc. Digest of Papers Ultra Wideband Systems and Technologies*, 2002, pp. 19–23.
- [26] D. Cassioli and A. Durantini, "A time-domain propagation model of the uwb indoor channel in the fcc-compliant band 3.6 - 6 ghz based on pn-sequence channel measurements," in *Proc. VTC 2004-Spring Vehicular Technology Conf. 2004 IEEE 59th*, vol. 1, 2004, pp. 213–217.
- [27] J. R. Foerster and Q. Li, "Uwb channel modeling contribution from intel," Intel, Tech. Rep. P802.15 02/279SG3a IEEE P802.15 SG3a contribution, 2002.
- [28] G. Stüber, *Principles of Mobile Communication*. Kluwer Academic, 2001.
- [29] A. A. M. Saleh and R. Valenzuela, "A statistical model for indoor multipath propagation," *IEEE Journal on Selected Areas in Communications*, vol. 5, no. 2, pp. 128–137, 1987.
- [30] G. Turin, F. Clapp, T. Johnston, S. Fine, and D. Lavry, "A statistical model of urban multipath propagation," *IEEE Transactions on Vehicular Technology*, vol. 21, no. 1, pp. 1 – 9, Feb 1972.
- [31] A. S.-J. R.M. Buehrer, W.A. Davis and D. Sweeney, "Ultra-wideband propagation measurements and modeling," Virginia Tech, DARPA NETEX Program, January 2004.
- [32] S. Venkatesh, J. Ibrahim, and R. M. Buehrer, "A new 2-cluster model for indoor uwb channel measurements," in *Proc. IEEE Antennas and Propagation Society Int. Symp*, vol. 1, 2004, pp. 946–949.
- [33] A. Papoulis, *Probability, Random Variables and Stochastic Processes*, 3rd ed. McGraw-Hill Companies, Feb. 1991.
- [34] S.-H. Sun and F.-C. Zheng, "Deconvolution method for removing the distortion from time jitter in equivalent-time waveform samplers," *Acta Metrologica Sinica*, vol. 10, no. 2, pp. 91–96, April 1989.
- [35] H. Ott, *Electromagnetic Compatibility Engineering*. John Wiley & Sons, 2009.
- [36] A. Taflove and S. Hagness, *Computational Electrodynamics: The Finite-Difference Time-Domain Method*, 2000.
- [37] B. Allen, M. Dohler, E. Okon, W. Malik, A. Brown, and D. Edwards, *Ultra-wideband antennas and propagation for communications, radar and imaging*. John Wiley & Sons, 2007.

- [38] H. L. Bertoni, *Radio Propagation for Modern Wireless Systems*. Prentice Hall, December 1999.
- [39] D. Cheng, *Field and wave electromagnetics*, ser. Addison-Wesley series in electrical engineering. Addison-Wesley, 1989.
- [40] J. Kraus and R. Marhefka, *Antennas for All Applications*. McGraw-Hill, 2003.
- [41] A. Molisch, "Ultra-wide-band propagation channels," *Proceedings of the IEEE*, vol. 97, no. 2, pp. 353–371, Feb. 2009.
- [42] H. Nikookar and R. Prasad, "Ultra wide band wireless channels," in *Introduction to Ultra Wideband for Wireless Communications*, ser. Signals and Communication Technology. Springer Netherlands, 2009, pp. 43–65.
- [43] C. Paul, *Introduction to Electromagnetic Compatibility*, ser. Wiley Series in Microwave And Optical Engineering. Wiley, 2006.
- [44] A. Raisanen and A. Lehto, *Radio Engineering for Wireless Communication and Sensor Applications*, ser. Artech House Mobile Communications Series. Artech House, 2003.
- [45] T. Rappaport, *Wireless Communications: Principles and Practice*, ser. Prentice Hall communications engineering and emerging technologies series. Prentice Hall PTR, 2002.
- [46] S. Saunders and A. Aragón-Zavala, *Antennas and Propagation for Wireless Communication Systems: 2nd Edition*. John Wiley & Sons, 2007.
- [47] Online materials information resource. MatWeb LLC, 2020 Kraft Drive, Suite 3005, Blacksburg, VA 24060 USA. [Online]. Available: <http://www.matweb.com/>
- [48] 3d cad browser. Shelley Walk 38, Hampshire, GU466YG United Kingdom. [Online]. Available: <http://www.3dcadbrowser.com/>